ORDERED POROUS CARBON AND NITROGEN-CONTAINING CARBON SUPPORTED NANO-PLATINUM ELECTRO-CATALYST FOR DIRECT METHANOL FUEL CELL APPLICATIONS

A project report
submitted in partial fulfilment of the requirements
for the award of the degree of

MASTER OF TECHNOLOGY
in
CHEMICAL ENGINEERING
SPECIALISATION : CATALYSIS TECHNOLOGY

by

K. DEVAKI
(CH09M001)

Under the guidance of
PROFESSOR P. SELVAM

DEPARTMENT OF CHEMICAL ENGINEERING
INDIAN INSTITUTE OF TECHNOLOGY- MADRAS
CHENNAI 600 036

MAY 2011

CERTIFICATE

This is to certify that the thesis entitled "**Ordered Porous Carbon and Nitrogen-containing Carbon Supported Nano-Platinum Electro-catalyst for Direct Methanol Fuel Cell Applications"**, submitted by **Ms. K. DEVAKI (CH09M001)** to the Indian Institute of Technology-Madras, Chennai for the award of the degree of **Master of Technology in Catalysis Technology (Chemical Engineering)**, is a *bona-fide* record of the work carried out by her under our supervision. The contents of this thesis, in full or in parts, have not been submitted to any other Institute or University for the award of any degree.

Guide	**Co-Guide**
PROF. P. SELVAM	Dr. PREETI AGHALAYAM
National Centre for Catalysis Research	Department of Chemical Engineering
IIT-Madras, Chennai 600 036	IIT-Madras, Chennai 600 036

Place: CHENNAI

Date : May 11, 2011

ACKNOWLEDGEMENTS

I am very much grateful to my research guide **Prof. P. Selvam** for his constant encouragement, thought provoking discussions, critical ideas, support, invaluable suggestions and unfailing guidance at every stage of the research programme. It gives me immense pleasure to have been associated with him. I thank him for his patient guidance, open discussions, constant encouragement, unbounded enthusiasm and interest.

I express my sincere gratitude to **Prof. B. Viswanathan** for his inspiring, invaluable guidance, constant encouragement and thought provoking discussions through out the research work. I am really grateful to him for providing opportunities to learn various aspects in catalysis and fuel cells. I feel privileged to have been associated with him. It is my privilege to express my gratitude to him for introducing me to the field of catalysis.

I am very much grateful to **Dr. Preeti Aghalayam,** my research co-guide, for her constant encouragement, support and invaluable suggestions.

I express my deep gratitude to **Prof. S. Pushpavanam**, Head, Department of Chemical Engineering and other faculty members of our department for the support and facilities provided in carrying out this project work.

I sincerely thank all my PG committee members, **Dr. S. Sivasanker**, **Dr. K. R. Krishna Murthy** and **Prof. R. Ramnarayanan**, for their constant encouragement and suggestions.

I wish to thank **NCCR** and **IIT Madras** for providing opportunity and all facilities to carry out my project.

I am thankful to **Mr. Narayanan** for surface area analysis, **Mrs. Kanchanamala** for TEM, **Mr. Omprakash** for SEM and **Dr. Thirunavukarasu** for XPS analysis. I would like to extend my thanks to Head and all the staff members of SAIF and Department of Metallurgy, IIT Madras for providing various facilities.

I wish to thank my class mates **Ms. Rajalakshmi, Mr. Chaitanya Dhoke, Mr. Sourav Khan** and **Mr. Sanjay Soni** for their motivation, encouragement and support through out my project period.

I express my sincere thanks to my seniors and colleagues, **Dr. Indraneel, Mr. Kuppan, Mr. Vamsi Krishna, Mr. Ramana Murthy, Mr. Mahendran, Mr. Anil Kumar, Mr. Sudhakar, Mr. Sankaranarayanan, Mr. Muthu Krishnan, Mr. Ramamohan, Mr. Pachamuthu, Mr. Prakash, Mr. Shanmugam, Mr. Ariharan, Mrs. Premlatha, Dr. Anuradha, Ms. Jeyalakshmi, Ms. Keerthiga, Ms. Alagarasi, Ms. Banu, Ms. Kaviya, Ms. Deepa** and **Ms. Vijayashanthi,** for their kindly help, suggestions and support.

I am deeply indebted to my father, **Sri. C. Krishnan** and mother, **Smt. K. Lakshmi** for their constant support and encouragement whenever needed, without them it would have been impossible for me to complete this work.

K. Devaki

ABSTRACT

Fuel cells are considered as the future energy conversion devices for wide variety of applications. Fuel cells can power almost any portable device or machine that uses batteries. Unlike a typical battery, which eventually goes dead, a fuel cell continues to produce energy as long as fuel and oxidant are supplied. Laptop, computers, cellular phones, video recorders, and hearing aids could be powered by portable fuel cells. Fuel cells have strong benefits over conventional combustion-based technologies currently used in many power plants and cars. They produce much smaller quantities of greenhouse gases and none of the air pollutants that create smog and cause health problems. If pure hydrogen is used as a fuel, fuel cells emit only heat and water as a byproduct. Hydrogen-powered fuel cells are also far more energy efficient than traditional combustion technologies.

Among the different types of fuel cells, the PEM (Polymer electrolyte membrane) fuel cells employing hydrogen as the fuel and the DMFC (Direct methanol fuel cell) employing methanol as the fuel are under development for successful commercialization. The commercialization of fuel cells is delayed mainly because of the high cost of the catalyst layer which needs expensive noble metals such as platinum and its alloys. The sluggish kinetics of oxygen reduction reaction in H_2 based PEMFC and both oxygen reduction and methanol oxidation reactions in DMFC, have caused concern. Even a slight enhancement in the activity and durability of these catalysts can bring down the cost significantly. The typical catalyst mostly used in fuel cell electrodes is Pt dispersed on carbon black support, for both anode and cathode electrodes.

Hydrogen is the most potential and promising fuel due to its high energy density and the maximum attainable voltage (E°_{max} =1.15 V), which is closer to the theoretical value (E°_{theor} = 1.23 V). But hydrogen fuel cell encounters challenges of hydrogen production, storage and transportation, whereas DMFC uses a liquid methanol as a fuel, which can be easily stored, handled and transported.

Carbon materials are the most widely used support for fuel cell electro-catalyst due to its various properties. These properties include corrosion resistance, anisotropic electronic property, formation of intercalation compounds, strong covalent bond formation with variety of surface modifiers and adsorbing capacity of wide variety of materials. The nature of the carbon determines the electrochemical performance of electrode catalysts. Interactions between the noble metal and the support may increase the catalyst performance. Carbon black, Vulcan XC-72 is the most common support material for fuel cell electro-catalyst. But nowadays various carbon materials have been investigated as electro-catalyst support like carbon nanofibers, carbon nanotubes, carbon aerogels and ordered nanoporous carbon (micro and mesoporous carbon).

Micro porous carbons, having very high surface area are of great technological interest for the development of catalytic, electro-catalytic and hydrogen storage systems. Ordered microporous carbons have been prepared by nanocasting method. i.e., CNPI-1 and NCNPI-1 have been synthesized by pyrolysis of furfuryl alcohol and pyrrole respectively within the pores of H-Mordenite. The inorganic templates were then removed by HF treatment, followed by filtration, washing and drying to obtain the microporous carbons. All the carbon samples were systematically characterized by various analytical and spectroscopic techniques including, XRD, XPS, SEM and N_2 sorption measurements. Subsequently, 10 and 20 wt % Pt were loaded on the microporous carbons using $H_2PtCl_6.6H_2O$ acid. The prepared platinum catalysts were systematically characterized by XRD, XPS and TEM.

The prepared catalysts were evaluated for their catalytic activity for methanol electro oxidation reaction. Electrochemical oxidation of methanol over the microporous carbon supported platinum catalysts was studied by cyclic voltammetry at room temperature. The electrochemical measurements performed using 1 M H_2SO_4 + 1 M CH_3OH indicate that the prepared catalysts exhibit excellent electrochemical activity as well as better CO tolerance compared to commercial Pt catalyst. The activity loss of the catalysts was studied by chronoamperometry (CA) measurement. Prepared microporous carbon supported Pt catalysts showed lesser activity loss compared to commercial Pt catalyst. It is therefore, concluded that platinum supported on ordered microporous carbon catalysts are promising electrode materials for methanol fuel cell applications.

KEYWORDS: Carbon materials, Microporous carbons, Nanocasting, Electro-catalysts, Methanol oxidation, Fuel cell, DMFC

TABLE OF CONTENTS

Title	**Page No.**
ACKNOWLEDGEMENTS	**i**
ABSTRACT	**iii**
LIST OF FIGURES	**viii**
LIST OF TABLES	**xiv**
ABBREVIATIONS	**xv**
NOTATIONS	**xvi**

CHAPTER 1 INTRODUCTION

1.1 Fuel Cells 1

1.2 Direct Methanol Fuel Cell (DMFC) 3

CHAPTER 2 LITERATURE SURVEY

2.1 Electro-catalysts for Methanol Oxidation 6

2.2 Support materials for Electro-catalysts 10

2.2.1 Carbon Nanotubes (CNTs) 10

2.2.2 Ordered Porous Carbons 11

2.2.3 Graphenes 16

2.2.4 Onion –like Fullerenes (OLFs) 17

2.3 Other Applications of Porous Carbons 17

2.3.1 Hydrogen Storage 17

2.3.2 Capacitor 18

CHAPTER 3 EXPERIMENTAL METHODS

3.1 Starting Materials 20

3.2 Characterization Techniques 20

3.2.1 X-ray diffraction (XRD) 20

3.2.2 BET surface area measurements 20

3.2.3 Scanning electron microscopy (SEM) 21

3.2.4 Transmission electron microscopy (TEM) 21

3.2.5 X-ray photoelectron spectroscopy (XPS) 21

3.2.6 Electrochemical measurements 21

CHAPTER 4 ORDERED MICROPOROUS CARBON (CNP-1) AND NITROGEN-CONTAINING CARBON (NCNP-1)

4.1 Introduction 25
4.2 Preparation Methods 26
4.3 Nanocasting 27
4.3.1 Zeolites as Hard Template 27
4.3.2 Use of furfural alcohol as carbon precursor 28
4.3.3 Use of pyrrole as carbon/nitrogen precursor 28
4.4 Characterization 29
4.4.1 XRD 29
4.4.2 Textural properties 32
4.4.3 SEM 33
4.4.4 XPS 36

CHAPTER 5 Pt/CNPI-1 AND Pt/NCNPI-1 ELECTRODES FOR DMFC APPLICATIONS

5.1 Electrode Materials for Methanol Oxidation 41
5.2 Preparation methods of Pt/ONCs 43
5.2.1 Colloidal deposition method 43
5.2.2 Wet impregnation method 44
5.2.3 Incipient-wetness impregnation method 44
5.3 Characterization 45
5.3.1 XRD 45
5.3.2 TEM 49
5.3.3 XPS 51
5.3.4 Electro oxidation of methanol - Cyclic Voltammetry 55
5.3.5 Evaluation of Mass Specific Activity (MSA) of the prepared catalysts 58
5.3.6 Methanol electro oxidation-Effect of scan rate 63
5.3.7 Evaluation of activity loss of the electrodes for methanol electro oxidation by Chronoamperometry 65

CHAPTER 6 SUMMARY AND CONCLUSIONS 68

APPENDIX A

A.1 EDX Spectras of ONCs 70
A.1.1 EDX Spectras of CNPI-1 70
A.1.2 EDX Spectras of NCNPI-1 71

APPENDIX B

B.1 Preparation of ONC from H-Mordenite and sucrose 74
B.2 Characterization 74
B.2.1 XRD 74
B.2.2 Textural properties 75
B.2.3 SEM 76
B.2.4 EDX 76

APPENDIX C

C.1 Preparation of ONCs using zeolite Y (Na-Y) 77
C.1.1 Furfural alcohol as a precursor 77
C.1.2 Sucrose as a precursor 77
C.2 Characterization 78
C.2.1 XRD 78
C.2.2 SEM 79
C.2.3 EDX 80

APPENDIX D

D.1 Area used for ESA calculations 82

APPENDIX E

E.1 Methanol electro oxidation – Effect of scan rate 85
E.2 Dependence of the peak currents on the square root of scan rates 88

APPENDIX F

CNPI-1 SUPPORTED Pt, Pd and Pd_3Pt ELECTRO-CATALYSTS FOR ORR

F.1 Introduction 90
F.2 Electro-catalysts for oxygen reduction reaction 90
F.2.1 Pt Metal Electro-catalysts 91
F.2.2 Pd Electro-catalysts 92
F.3 Characterization 93
F.3.1 XRD 93
F.3.2 Electrochemical reduction of oxygen 97
REFERENCES 99

LIST OF FIGURES

Title		Page No.
Figure 1.1	Schematic representation of a Fuel Cell	2
Figure 1.2	Schematic representation of a Direct Methanol Fuel Cell	4
Figure 2.1	Schematic representation of MeOH oxidation by Au-Pt/C	9
Figure 2.2	Preparation of CNT by a template carbonization technique	10
Figure 2.3	Schematic representation of synthesis of carbon from zeolite	11
Figure 2.4	Schematic representation of nanoporous carbon from MOF-5	13
Figure 2.5	Schematic representation of synthesis of OMC from silica	13
Figure 2.6	Schematic representation of the preparation of ordered mesoporous polymer resins and carbon frameworks	15
Figure 2.7	Schematic representation of synthesis of graphene nanosheet supported catalyst. (1) Oxidation of graphite to graphite oxide with larger inter layer distance; (2) Exfoliation of graphite oxide by ultrasonication and (3) Preparation of GNS based catalyst by colloidal method	16
Figure 3.1	A model Cyclic Voltammogram of Pt/C catalyst in 1M H_2SO_4 at room temperature (scan rate: 50 mV/s)	22
Figure 4.1	Schematic representation of nanocasting pathway, showing the change of the mesostructure during the process. The process mainly includes three steps: (1) Precursor infiltration inside mesochannels of the silica template; (2) Conversion of the precursor in the nanochannels; (3) Removal of mesoporous silica template	27
Figure 4.2	XRD pattern of CNPI-1	30
Figure 4.3	XRD pattern of NCNPI-1	31
Figure 4.4	N_2 sorption isotherm of CNPI-1. Inset: Pore size distribution of CNPI-1	32
Figure 4.5	N_2 sorption isotherm of NCNPI-1. Inset: Pore size distribution of NCNPI-1	32
Figure 4.6	SEM images of: (a) H-Mordenite; (b) FA / H-MOR composite; (c) Heat treated sample; (d) CNPI-1(2 % HF; 9 h); (e) CNPI-1 (5 % HF; 3 h); (f) CNPI-1 (5 % HF; 6 h)	35

Figure 4.7 SEM images of (a) H-Mordenite; (b) Pyrrole / H-MOR composite; (c) Heat treated sample; (d) NCNPI-1 (5 % HF; 1 h); (e) NCNPI-1 (5 % HF; 2 h); (f) NCNPI-1 (5 % HF; 3 h); (g) NCNPI-1 (5 % HF; 6 h); (h) NCNPI-1 (5 % HF; 9 h) 35

Figure 4.8 Survey XPS spectra of (a) NCNPI-1; (b) CNPI-1 36

Figure 4.9 XPS spectra of CNPI-1 and NCNPI-1(a) C (1s); (b) O (1s); 37

Figure 4.10 Deconvoluted XPS spectra of C 1s of (a) CNPI-1; (b) NCNPI-1 38

Figure 4.11 Deconvoluted XPS spectra of O 1s of (a) CNPI-1; (b) NCNPI-1 39

Figure 4.12 Deconvoluted XPS spectra of N 1s of NCNPI-1 39

Figure 4.13 Model of a carbon layer with nitrogen atoms bonded differently 40

Figure 5.1 XRD patterns of 10 wt.% Pt/AC prepared by different methods 46

Figure 5.2 XRD patterns of 10 wt.%Pt/ ONCs prepared by colloidal deposition method using SBH as a reducing agent 47

Figure 5.3 XRD patterns of 20 wt.% Pt supported on ONCs and AC prepared by colloidal deposition method using SBH as a reducing agent 47

Figure 5.4 XRD patterns of 20 wt.% Pt supported on ONCs and AC prepared by colloidal deposition method using EG as a reducing agent 48

Figure 5.5 TEM and ED of: (a) 20 wt.% Pt/CNPI-1 (SBH); (b) 10 wt.% Pt/NCNPI-1 (SBH); (c) 20 wt.% Pt/CNPI-1 (EG) 50

Figure 5.6 Histogram of the ONCs supported Pt catalysts (a) 20 wt.% Pt/CNPI-1 (SBH); (b) 10 wt.% Pt/NCNPI-1 (SBH); (c) 20 wt.% Pt/CNPI-1 (EG) 51

Figure 5.7 Survey XPS spectra of (a) 20 wt.% Pt/AC (EG); (b) 20 wt.% Pt/CNPI-1 (SBH) 52

Figure 5.8 Survey XPS spectra of (a) 10 wt.% Pt/NCNPI-1 (SBH); (b) 10 wt.% Pt/CNPI-1 (SBH) 52

Figure 5.9 XPS spectra of Pt 4f of (a) 20 wt.% Pt/C; (b) 10 wt.% Pt/ONCs 53

Figure 5.10 XPS spectra of CNPI-1 and 10 wt.% Pt/CNPI-1 (SBH) (a) C (1s); (b) O (1s) 53

Figure 5.11 XPS spectra of NCNPI-1 and 10 wt.% Pt/NCNPI-1 (SBH) (a) C (1s); (b) O (1s); (c) N (1s) 55

Figure 5.12 Cyclic voltammograms of (a) 20 wt.% Pt/NCNPI-1 (SBH); (b) 20 wt.% Pt/CNPI-1 (SBH); (c) 20 wt.% Pt/AC (SBH); (d) 40 wt.% Pt/E-TEK measured in 1 M H_2SO_4 electrolyte at room temperature (scan rate: 50 mV/s) 56

Figure 5.13 Cyclic voltammograms of (a) 20 wt.% Pt/E-TEK; (b) 20 wt.% Pt/ CNPI-1 (EG); (c) 20 wt.% Pt/AC (EG); (d) 20 wt.% Pt/NCNPI-1 (EG) measured in 1 M H_2SO_4 electrolyte at room temperature (scan rate: 50 mV/s) 57

Figure 5.14 Cyclic voltammograms of (a) 10 wt.% Pt/CNPI-1 (SBH); (b) 10 wt.% Pt/NCNPI-1 (SBH) measured in 1 M H_2SO_4 electrolyte at room temperature (scan rate: 50 mV/s) 58

Figure 5.15 MSA of (a) 40 wt.% Pt/E-TEK; (b) 20 wt.% Pt/AC (SBH); (c) 20 wt.% Pt/CNPI-1(SBH); (d) 20 wt.% Pt/NCNPI-1 (SBH) for methanol electro oxidation reaction in 1 M CH_3OH + 1 M H_2SO_4 at room temperature (scan rate: 50 mV/s) 59

Figure 5.16 MSA of (a) 20 wt.% Pt/CNPI-1 (EG); (b) 20 wt.% Pt/NCNPI-1 (EG); (c) 20 wt.% Pt/E-TEK; (d) 20 wt.% Pt/AC (EG) for methanol electro oxidation reaction in 1 M CH_3OH + 1 M H_2SO_4 at room temperature (scan rate: 50 mV/s) 60

Figure 5.17 MSA of (a) 10 wt.% Pt/CNPI-1 (SBH); (b) 10 wt.% Pt/NCNPI-1 (SBH) for methanol electro oxidation reaction in 1 M CH_3OH + 1 M H_2SO_4 at room temperature (scan rate: 50 mV/s) 61

Figure 5.18 Cyclic voltammograms of 20 wt.% Pt/CNPI-1 (SBH) at different scan rates ((a) 25 mV/s; (b)50 mV/s; (c) 75 mV/s; (d) 100 mV/s) in 1 M CH_3OH and 1 M H_2SO_4 at room temperature 64

Figure 5.19 Dependence of the peak currents on the square root of scan rates for 20 wt.% Pt/CNPI-1 (SBH) in 1 M CH_3OH and 1 M H_2SO_4 at room temperature 64

Figure 5.20 Chronoamperometry of (a) 40 wt.% Pt/E-TEK; (b) 20 wt.% Pt/CNPI-1 (SBH); (c) 20 wt.% Pt/AC (SBH); (d) 20 wt.% Pt/E-TEK; (e) 20 wt.% Pt/NCNPI-1 (SBH) for methanol electro oxidation reaction in 1 M CH_3OH + 1 M H_2SO_4 at room temperature 65

Figure 5.21 Chronoamperometry of (a) 20 wt.% Pt/E-TEK; (b) 20 wt.% Pt/CNPI-1 (EG); (c) 20 wt.% Pt/AC (EG); (d) 20 wt.% Pt/NCNPI-1 (EG) for methanol electro oxidation reaction in 1 M CH_3OH + 1 M H_2SO_4 at room temperature 66

Figure 5.22 Chronoamperometry of (a) 10 wt.% Pt/CNPI-1 (SBH); (b) 10 wt.% Pt/NCNPI-1 (SBH) for methanol electro oxidation reaction in 1 M CH_3OH + 1 M H_2SO_4 at room temperature 66

Figure A.1 EDX spectras of (a) H-Mordenite; (b) FA / H-MOR composite; (c) Heat treated sample; (d) CNPI-1 (2 % HF; 9 h); (e) CNPI-1 (5 % HF; 3 h); (f) CNPI-1 (5 % HF; 6 h) 71

Figure A.2 EDX spectras of (a) H-Mordenite; (b) Pyrrole / H-MOR composite; (c) Heat treated sample; (d) NCNPI-1 (5 % HF; 1 h); (e) NCNPI-1 (5 % HF; 2 h); (f) NCNPI-1 (5 % HF; 3 h); (g) NCNPI-1 (5 % HF; 6 h); (h) NCNPI-1 (5 % HF; 9 h) 73

Figure B.1 XRD pattern of CNPI-9 74

Figure B.2 N_2 sorption isotherm of CNPI-9. Inset: Pore size distribution of CNPI-9 75

Figure B.3 SEM images of (a) H-Mordenite; (b) CNPI-9 76

Figure B.4 EDX spectra of (a) H-Mordenite; (b) CNPI-9 76

Figure C.1 XRD pattern of CNPI-2 78

Figure C.2 XRD pattern of CNPI-8 78

Figure C.3 SEM images of (a) Na-Y; (b) CNPI-2 79

Figure C.4 SEM images of (a) Na-Y; (b) CNPI-8 79

Figure C.5 EDX Spectra of (a) Na-Y; (b) CNPI-2 80

Figure C.6 EDX Spectra of (a) Na-Y; (b) CNPI-8 80

Figure D.1 Cyclic Voltammogram of 40 wt.% Pt/E-TEK catalyst in 1 M H_2SO_4 at room temperature (scan rate: 50 mV/s) 82

Figure D.2 Cyclic Voltammogram of 20 wt.% Pt/CNPI-1 (SBH) catalyst in 1 M H_2SO_4 at room temperature (scan rate: 50 mV/s) 82

Figure D.3 Cyclic Voltammogram of 20 wt.% Pt/AC (SBH) catalyst in 1 M H_2SO_4 at room temperature (scan rate: 50 mV/s) 83

Figure D.4 Cyclic Voltammogram of 20 wt.% Pt/CNPI-1 (EG) catalyst in 1 M H_2SO_4 at room temperature (scan rate: 50 mV/s) 83

Figure D.5 Cyclic Voltammogram of 10 wt.% Pt/CNPI-1 (SBH) catalyst in 1 M H_2SO_4 at room temperature (scan rate: 50 mV/s) 84

Figure E.1 Cyclic voltammograms of 20 wt.% Pt/NCNPI-1 (SBH) at Different scan rates ((a) 25 mV/s; (b) 50 mV/s; (c) 75 mV/s; (d) 100 mV/s) in 1 M H_2SO_4 and 1 M CH_3OH at room temperature 85

Figure E.2 Cyclic voltammograms of 20 wt.% Pt/AC (SBH) at different scan rates ((a) 25 mV/s; (b) 50 mV/s; (c) 75 mV/s; (d) 100 mV/s) in 1 M H_2SO_4 and 1 M CH_3OH at room temperature 85

Figure E.3 Cyclic voltammograms of 20 wt.% Pt/CNPI-1 (EG) at different scan rates ((a) 25 mV/s; (b) 50 mV/s; (c) 75 mV/s; (d) 100 mV/s) in 1 M H_2SO_4 and 1 M CH_3OH at room temperature 86

Figure E.4 Cyclic voltammograms of 20 wt.% Pt/NCNPI-1 (EG) at different scan rates ((a) 25 mV/s; (b) 50 mV/s; (c) 75 mV/s; (d) 100 mV/s) in 1 M H_2SO_4 and 1 M CH_3OH at room temperature 86

Figure E.5 Cyclic voltammograms of 20 wt.% Pt/AC (EG) at different scan rates ((a) 25 mV/s; (b) 50 mV/s; (c) 75 mV/s; (d) 100 mV/s) in 1 M H_2SO_4 and 1 M CH_3OH at room temperature 87

Figure E.6 Cyclic voltammograms of 10 wt.% Pt/CNPI-1(SBH) at different scan rates ((a) 25 mV/s; (b) 50 mV/s; (c) 75 mV/s; (d) 100 mV/s) in 1 M H_2SO_4 and 1 M CH_3OH at room temperature 87

Figure E.7 Cyclic voltammograms of 10 wt.% Pt/NCNPI-1(SBH) at different scan rates ((a) 25 mV/s; (b) 50 mV/s; (c) 75 mV/s; (d) 100 mV/s) in 1 M H_2SO_4 and 1 M CH_3OH at room temperature 88

Figure E.8 Dependence of the peak currents on the square root of scan rates of (a) 20 wt.% Pt/AC (SBH); (b) 20 wt.% Pt/CNPI-1 (SBH); (c) 20 wt.% Pt/NCNPI-1 (SBH) in1 M H_2SO_4 and 1 M CH_3OH at room temperature 88

Figure E.9 Dependence of the peak currents on the square root of scan rates of (a) 20 wt.% Pt/CNPI-1 (EG); (b) 20 wt.% Pt/AC (EG); (c) 20 wt.% Pt/NCNPI-1 (EG) in1 M H_2SO_4 and 1 M CH_3OH at room temperature 89

Figure E.10 Dependence of the peak currents on the square root of scan rates of (a) 10 wt.% Pt/CNPI-1 (SBH); (b) 10 wt.% Pt/NCNPI-1 (SBH) in 1 M H_2SO_4 and 1 M CH_3OH at room temperature 89

Figure F.1 XRD patterns of 10 wt.% Pd/AC prepared by colloidal deposition and WI method using SBH as a reducing agent 93

Figure F.2 XRD patterns of 20 wt.% Pd/ C (C: CNPI-1/AC) prepared by colloidal deposition method using different reducing agents (SBH and EG) 94

Figure F.3 XRD patterns of Pd_3Pt/C (C: CNPI-1/AC) prepared by colloidal deposition method using SBH as a reducing agent 95

Figure F.4 XRD patterns of Pd_3Pt/C (C: CNPI-1/AC) prepared by colloidal deposition method using EG as a reducing agent 95

Figure F.5 Cyclic voltammograms of (a) 20 wt.% Pt/ CNPI-1 (SBH); (b) 20 wt.% Pd/ CNPI-1 (SBH);(c) Pd_3Pt/ CNPI-1 (SBH) in N_2 and O_2 saturated 1 M H_2SO_4 solution at room temperature (scan rate: 50 mV/s) 98

LIST OF TABLES

Title **Page No.**

Table 1.1 Classification of Fuel Cell 2

Table 1.2 Chemical and electrochemical data of various fuels 3

Table 2.1 List of the reported ordered mesoporous carbons 14

Table 4.1 Textural properties of CNPI-1 and NCNPI-1 33

Table 4.2 Elemental analysis results of CNPI-1 34

Table 4.3 Elemental analysis results of NCNPI-1 36

Table 5.1 Effect of preparation methods on the crystallite size of the AC supported Pt catalysts 48

Table 5.2 Effect of reducing agents and platinum loading on the crystallite size of the carbon (ONCs and AC) supported Pt catalysts 49

Table 5.3 Effect of Pt loading and the nature of the carbon support on the electro-catalytic activity of methanol oxidation of Pt/ONCs and Pt/AC 62

Table 5.4 Effect of Pt loading and the nature of the carbon support on the EAS, MSA and SA of methanol electro oxidation of Pt/ONCs and Pt/AC at + 0.7 V 63

Table 5.5 Effect of Pt loading and the nature of the carbon support on the stable activity for methanol electro oxidation of Pt/ONCs and Pt/AC by chronoamperometry 67

Table B.1 Textural properties of CNPI-9 75

Table B.2 Elemental analysis results of CNPI-9 76

Table C.1 Elemental analysis results of CNPI-2 81

Table C.2 Elemental analysis results of CNPI-8 81

Table F.1 Effect of preparation methods on the crystallite size of the AC supported Pd catalysts 96

Table F.2 Effect of reducing agents and palladium loading on the crystallite size of the carbon supported Pd catalysts 96

Table F.3 Effect of reducing agents and active metal loading on the crystallite size of the carbon supported Pd_3Pt catalysts 97

Table F.4 ORR activity of the prepared monometallic and bimetallic catalysts 98

ABBREVIATIONS

AC	Activated Carbon
CNT	Carbon Nanotube
ONC	Ordered Microporous Carbon
OMC	Ordered Mesoporous Carbon
CNPI-1	ONC from H-Mordenite (template) and furfural alcohol (carbon precursor)
NCNPI-1	ONC from H-Mordenite (template) and pyrrole (carbon/nitrogen precursor)
CNPI-9	ONC from H-Mordenite (template) and sucrose (carbon precursor)
CNPI-2	ONC from Na-Y (template) and furfural alcohol (carbon precursor)
CNPI-8	ONC from Na-Y (template) and sucrose (carbon precursor)
CV	Cyclic Voltammetry
CA	Chronoamperometry
DMFC	Direct Methanol Fuel Cell
XRD	X-ray Diffraction
EDX	Energy Dispersive X-ray Analysis
SCE	Standard Calomel Electrode
ORR	Oxygen Reduction Reaction
SEM	Scanning Electron Microscopy
TEM	Transmission Electron Microscopy
XPS	X-ray Photoelectron Spectroscopy
EAS	Electrochemical active surface area
MSA	Mass Specific Activity
SA	Specific Activity
EG	Ethylene Glycol
SBH	Sodium Borohydride
WI	Wet Impregnation
FA	Furfural Alcohol
ED	Electron Diffraction

NOTATIONS

Å	Angstrom
θ	Angle
Λ	Wavelength
h	hour
°C	Degree Celsius
T	Temperature
cm	centimeter
eV	Electron volt
mV	milli volt
mA	milli amphere
E	Potential (V)
I	Current
t	Time
β	Full width at half maximum

CHAPTER 1

INTRODUCTION

1.1 FUEL CELLS

Fuel cells (Fig. 1.1.) are electrochemical devices that directly convert chemical energy of fuel and oxidant to electrical energy by the redox process with high efficiencies and zero emission. They consist of an anode, cathode, electrolyte, gas-diffusion layer and bipolar plates. An anode facilitates the oxidation of the fuel, while a cathode promotes the reduction of oxidant. The electrodes should be both catalytically active and conductive in nature. The electrodes are used to provide the necessary active sites, physical barrier which separates the bulk gas phase and the electrolyte and also to facilitate the ion transport away from or into the three-phase interface. The electrolyte also acts as a physical barrier between the fuel and oxidant.

Fuel cells are mainly classified based on electrolyte. The choice of the electrolyte medium decides the operating temperature of the fuel cell (Viswanathan and Scibioh, 2006; Ramani, 2006). The porous gas diffusion layers (GDLs) provide structural support for the electrodes and diffusion path through which the oxidant or fuel gases can reach the catalyst. GDLs are made of carbon paper or woven carbon cloth. Bipolar plates can be coated with dispersed carbon to provide corrosion resistance and good electrical conductivity. The bipolar plates used for the distribution of fuel and oxidant; heat and water management; separate the individual cells in the stack and to humidify the gases and also as a current collector (Dicks, 2006).

Fuel cells can be classified based on fuel (direct or indirect fuel), oxidant, electrolyte and temperature. The details are given in Table 1.1.

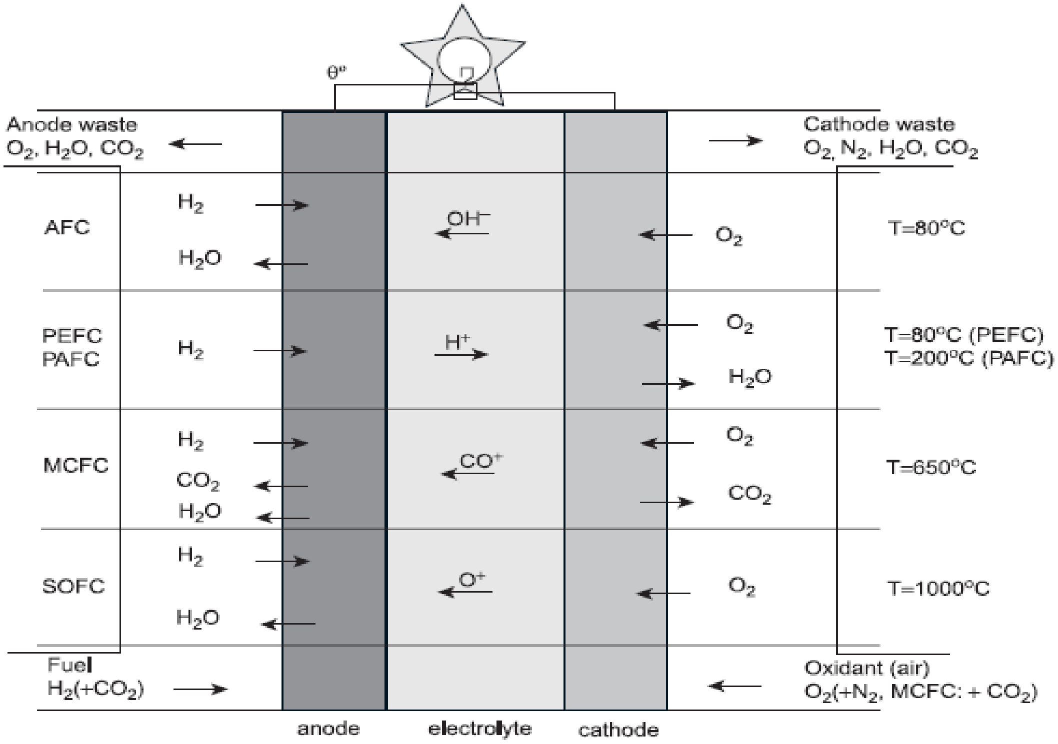

Figure 1.1: Schematic representation of a Fuel Cell (Viswanathan and Scibioh, 2006).

Table 1.1: Classification of Fuel cell.

Fuel		**Oxidant**	**Electrolyte**	**Temperature**
Direct	**Indirect**			
Hydrogen	Methanol	Oxygen (pure)	Solid polymer electrolyte	Low (RT - 120 °C)
Methanol	Ethanol	Air (oxygen)	Aq. sulfuric acid	Intermediate (120 - 250 °C)
Ammonia	Hydrocarbon	H_2O_2	Aq. phosphoric acid	High (250 - 750 °C)
Hydrazine	Ammonia		Aq. KOH	Very high (> 750°C)
Formic acid	Hydride		Aq. K_2CO_3	
Ethanol	Coal		Molten carbonate (Li_2CO_3-Na_2CO_3)	
Coal gas			Solid oxide (Yttrium-stabilized Zirconia)	
Coal				

The choice of the fuel depends on their chemical and catalytic activity. Table 1.2 shows the list of fuels that can be used in fuel cells.

Table 1.2: Chemical and electrochemical data of various fuels (Viswanathan and Scibioh, 2006).

Fuel	**$-\Delta G^{\circ}$ (kcal/mol)**	**E°_{theor} (V)**	**E°_{max} (V)**	**Energy density (kWh/kg)**
Hydrogen	56.69	1.23	1.15	32.67
Methanol	166.8	1.21	0.98	6.13
Ammonia	80.8	1.17	0.62	5.52
Hydrazine	143.9	1.56	1.28	5.22
Formaldehyde	124.7	1.35	1.15	4.82
Carbon monoxide	61.6	1.33	1.22	2.04
Formic acid	68.2	1.48	1.14	1.72
Methane	195.5	1.06	0.58	-
Propane	503.2	1.08	0.65	-

From the above table one can conclude that, hydrogen is the most potential and promising fuel due to its high energy density and the maximum attainable voltage which is closer to the theoretical value. But hydrogen fuel cell encounters challenges of hydrogen production, storage and transportation, whereas DMFC uses a liquid methanol as a fuel, which can be easily stored, handled and transported.

1.2 DIRECT METHANOL FUEL CELL (DMFC)

DMFC (Fig. 1.2) is considered as a promising candidate for clean and portable power sources, transportation applications and electric vehicles. Methanol is a liquid fuel, so it can be easily handled and stored. And also, it is having high heating value and solubility in aqueous electrolytes. However, various limitations such as sluggish anode kinetics (six electron transfer process), methanol crossover (causing mixed potential at the cathode), high loading of noble metals, carbon monoxide poisoning and carbon dioxide removal at an anode remain as major problems for commercialization of DMFC.

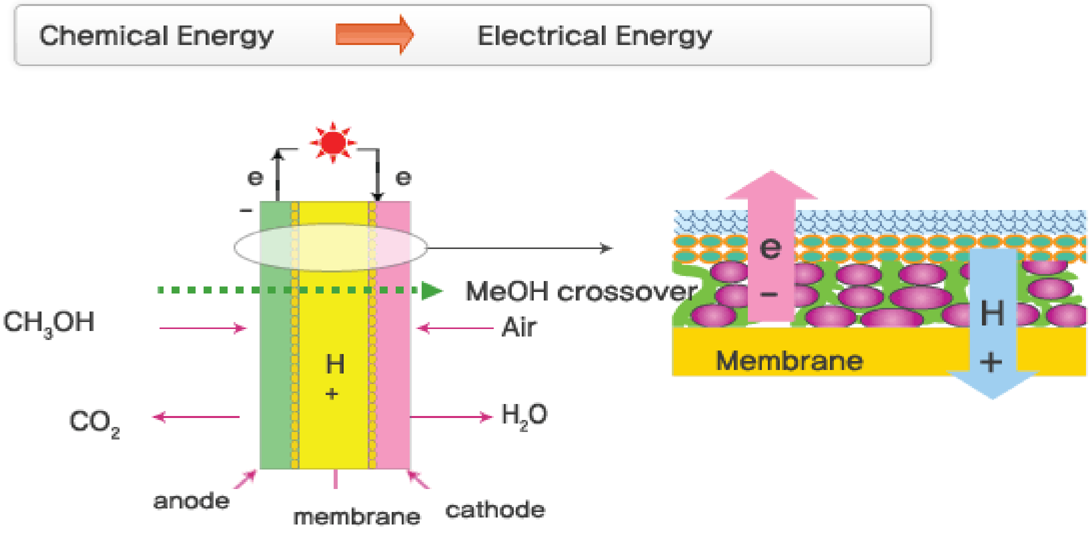

Figure 1.2: Schematic representation of a Direct Methanol Fuel Cell.

In the case of conventional platinum (Pt) catalyst, the adsorption of CO, one of the intermediates in methanol oxidation, block the active sites, resulting in prevention of further methanol adsorption. To reduce CO poisoning effect, CO tolerant electro-catalysts have been examined. In nano scale, gold (Au) is the active catalyst for CO oxidation at lower temperature. Au facilitates the removal of CO, thus poisoned sites can be regenerated by the presence of Au. On the other hand, various Pt-based alloys (bimetallics) such as Pt-Ru, Pt-Os, Pt-Sn, Pt-W, Pt-Mo have been examined. Since methanol oxidation is a demanding reaction, the atomic radii between two metals should be in a proper ranges, so that it will facilitate the CO oxidation reaction. And also second metal should be oxophilic in nature, so that it can provide active form of oxygen in order to oxidize the poisonous CO.

Ruthenium (Ru) has been the best metal to validate the above points. And also Ru will form an oxygenated species at lower potential compared to Pt. Therefore PtRu is the state-of-the-art anode catalyst. The increased activity of PtRu for methanol oxidation can be due to bi-functional mechanism (Pt promotes the dissociative chemisorption of methanol whereas Ru forms a surface oxy-hydroxide which is used to oxidizes the CO to CO_2) or by a ligand effect, the second metal modifies the electronic properties of the Pt in a such way, so that weakening the chemical bond between platinum and the surface intermediates is facile, (Hamnett, 1997). The catalytic activity of the PtRu electro-catalyst depends on the composition, structure, morphology, particle size, particle size distribution, oxidation state of Pt and Ru and alloyed degree (Liu *et al.*, 2006).

The maximum utilization, dispersion of electro-catalyst can be obtained by choosing the proper supporting material. The role of supporting material includes achieving high surface area, high dispersion, improved activity and stability. It also prevents the agglomeration of metal nanoparticles and decreases the mass transfer limitations. The ideal support material should have some specific characteristic like wide electrochemical potential window (Electrochemical properties), good corrosion resistance (Chemical properties), and high electrical conductivity (Electrical properties) and mechanical stability (Salgado *et al.*, 2010).

Pt and Au are in cubic lattice, whereas Ru has hexagonal lattice. Platinum is most widely used as an anode because of its ability to remove the CO poisonous species at + 0.7 V, whereas Ru is able to remove CO poisonous species at a lower potential (less than + 0.7 V) by ligand effect. Therefore Pt-Ru bimetallic is the best electro-catalyst for the oxidation of methanol.

CHAPTER 2

LITERATURE SURVEY

2.1 ELECTRO-CATALYSTS FOR METHANOL OXIDATION

The common criteria for a high performance electro-catalysts are:

(i) narrow nanoscale size distribution

(ii) uniform composition throughout the nanoparticles

(iii) full degree of alloying

(iv) high dispersion on the carbon support.

Salgado *et al.* (2010) reported the synthesis of Pt-Ru electro-catalysts supported on ordered mesoporous carbon (CMK-3) for DMFC by formic acid method. Methanol and carbon monoxide oxidation were studied by cyclic voltammetry, and current-time curves were reordered in a methanol solution to establish the activity under potentiostatic conditions. At 0.6 V, Pt-Ru/CMK-3 showed highest current density in both CV (223 $\mu A/cm^2$) and chronoamperometric (102 $\mu A/cm^2$) tests compared to Pt-Ru/ Vulcan (CV: 134 $\mu A/cm^2$ and CR: 91 $\mu A/cm^2$) and Pt-Ru/ C (E) (CV: 48 $\mu A/cm^2$ and CR: 74 $\mu A/cm^2$). These results show the effect of mesoporous carbon support. From these results, they have concluded that bimetallic Pt-Ru supported on ordered mesoporous carbon is the most suitable electro-catalyst for methanol oxidation.

Guo *et al.* (2006) reported the synthesis of ceria (CeO_2) modified PtRu supported on carbon (Vulcan XC72) catalysts with different compositions of Ru and CeO_2 {$PtRu_{0.9}(CeO_2)_{0.1}/C$, $PtRu_{0.7}(CeO_2)_{0.3}/C$, $PtRu_{0.5}(CeO_2)_{0.5}/C$ and unmodified PtRu/C}by the sodium borohydride reduction method. They employed CeO_2 as a co-catalytic material along with Pt-Ru catalyst since CeO_2 has the higher oxygen storage capacity. So the oxygen atoms present in the CeO_2 lattice can be used for promoting bi-functional mechanism of methanol oxidation. They have found that $PtRu_{0.7}(CeO_2)_{0.3}/C$ exhibited higher activity for methanol oxidation than the conventional Pt-Ru/C catalyst.

Liu *et al.* (2003) have reported the synthesis of nanosized Pt and Pt-Ru colloids by a microwave-assisted polyol process. This method involves a rapid microwave synthesis of Pt and Pt-Ru colloids in ethylene glycol followed by the transfer of the colloidal metal particles to toluene using decanethiol as the phase transfer catalyst. The thiol-encapsulated Pt and Pt-Ru colloids are then deposited on carbon and heat treated to produce carbon supported Pt and Pt-Ru catalysts. Due to bi-functional mechanism, binary catalyst was more active than the monometallic Pt and less receptive to methanolic residue deactivation.

Bensebaa *et al.* (2004) have reported the optimum thermal conditions necessary to prepare the monometallic and alloyed bimetallic nanocatalysts using microwave heating. Alloyed Pt-Ru nanocatalysts have been prepared using microwave heating at a maximum heating temperature of 173 °C in less than 5 minutes. Also they have investigated the effects of preparation parameters to optimize the particles' composition and structure characteristics in the presence of ploy (N-vinyl-2-pyrrolidone) (PVP) and ethylene glycol (EG). In this method, EG was used both as a solvent and reducing agent whereas PVP was used as a protective layer against agglomeration. The resulting catalyst had uniform diameters of 2-3 nm for the PVP-coated samples. In the absence of PVP, agglomerated, inhomogeneous, larger nanocrystals were obtained with a Pt-rich core and a Ru-rich Shell.

Solla-Gullón *et al.* (2004) have reported electrochemical characterization of Pt-Ru nanoparticles which was prepared by water-in-oil microemulsion method. They have studied electro-catalytic properties of Pt-Ru nanoparticles through Co_{ads} oxidation and methanol oxidation reactions. The highest molar oxidation currents were obtained for $Pt_{80}Ru_{20}$. Pt-Ru nanoparticles with Pt ranging between 40 and 80 % show higher oxidation currents than pure Pt.

Xiong and Manthiram (2005) have synthesized the nanostructured Pt-Ru/C catalysts with different particle sizes by microemulsion method and reported that the samples prepared with water to surfactant molar ratio (W) of 10 attains the maximum mass activity with the least charge transfer resistance and particle size of around 5.3 nm. The better performance of the Pt-Ru/C prepared by microemulsion method can be attributed to a better control of particle size, crystallinity and microstructure. By optimizing the synthesis and processing conditions, the further improvement in the performance of the catalyst can be achieved.

Xue *et al.* (2005) have reported the synthesis of highly dispersed Pt-Ru/C catalysts by a two-step spray pyrolysis (SP) method. This method is used for the synthesis of particles with controllable size since the properties of final product can be controlled through the precursor choice, solution concentration and operating conditions. In an SP process, the reaction temperature, composition of the carrier gas and the solution properties are the important variables. The catalyst prepared by SP process required 0.39 V to achieve 300 mA/cm^2, whereas commercial catalyst Pt-Ru/C (E-TEK) required 0.34 V to achieve the same. This result indicates that the electro-catalytic activity of the Pt-Ru/C (SP) catalyst for methanol oxidation is better than that of the Pt-Ru/C (E) catalyst. The high electro-catalytic activity of Pt-Ru/C (SP) can be attributed to the uniform distribution, small average particle size and high alloying degree of the Pt-Ru crystal particles.

Wu and Xu (2007) have synthesized and compared the electrochemical performance of the Pt electro-catalyst supported on multi-walled (MWNT) and single-walled carbon nanotubes (SWNTs). They reported that Pt/SWNT exhibits high CO tolerance due to better supply of OH groups form the SWNT surface and a preferential exposure of Pt (111) plane in the crystal structure. And also for methanol oxidation reaction, it showed higher current density, lower onset potential and lower charge transfer potentials. Li and Xing (2007) have reported the electrochemical properties of PtRu nanoparticles supported on functionalized carbon nanotubes. Three different catalysts, namely $Pt_{53}Ru_{47}$, $Pt_{69}Ru_{31}$ and $Pt_{77}Ru_{23}$ were prepared for the evaluation of compositional effects. Sonochemically functionalized CNTs used for the preparation of highly dispersed PtRu with the size of less than 3.0 nm. From the electrochemical test, they have obtained highest current density and stability for $Pt_{53}Ru_{47}$. Li *et al.* (2010) have synthesized PtBi/XC-72 with Pt solid-solution structure using sodium hypophosphite as a reducing agent. In the presence of phosphorus, the Pt-Bi formed an alloy with a Pt FCC solid-solution phase structure, and it showed a better electro-catalytic activity for methanol oxidation. The better electro-catalytic activity can be attributed to the combined effect of bi-functional mechanism and ligand effect.

One of the major challenges in DMFC is the fuel crossover from anode to cathode, causing the depletion of oxygen surface concentration, poisoning of the cathode catalyst and a reduction in fuel efficiency. Therefore, it is necessary to use a methanol tolerant cathode catalyst instead of conventional Pt catalyst. Xia *et al.* (2006) have synthesized ordered intermetallic $PtBi_2$ nanoparticles for methanol-tolerant catalyst for oxygen reduction reaction by co-reducing H_2PtCl_6 and $Bi(NO_3)_3$ with $NaBH_4$ in the presence of polyvinylpyrrolidone (PVP) as a capping agent. The methanol-tolerant property of $PtBi_2$ nanoparticles can be explained in two ways:

(i) The formation of the $PtBi_2$ phase results in a charge redistribution, which may affect the formation of oxygen-containing species from water dissociation

(ii) Pt-Pt distance in $PtBi_2$ is larger and may not be suitable for the formation of oxygen-containing species.

Luo *et al.* (2006) have explored the characterization of carbon-supported Au-Pt nanoparticles for electro-catalytic methanol oxidation reaction (Fig. 2.1). The characterization results showed the dependence of the morphology and the surface binding properties of the bimetallic nanoparticles on the temperature. The carbon supported Au-Pt nanoparticles catalysts with 65 % to 85 % Au and treated at 500 °C are shown to exhibit higher electro-catalytic activity in alkaline medium. The bi-functional properties could involve a combination of the following reactions,

$$\mathrm{MeOH} + \mathrm{Pt} \rightarrow \mathrm{Pt{-}CO_{ad}} + \mathrm{CO_3^-} \tag{1}$$

$$\mathrm{Pt{-}CO_{ad}} + \mathrm{Au} \rightarrow \mathrm{Au{-}CO_{ad}} + \mathrm{Pt} \tag{2}$$

$$\mathrm{Au} + \mathrm{OH^-} \rightarrow \mathrm{Au{-}OH_{ad}} + e^- \tag{3}$$

$$\mathrm{Pt{-}CO_{ad}} + \mathrm{Au{-}OH_{ad}} \rightarrow \mathrm{CO_3^-} + \mathrm{Pt} + \mathrm{Au} + e^- \tag{4}$$

$$\mathrm{Au{-}CO_{ad}} + \mathrm{Au{-}OH_{ad}} \rightarrow \mathrm{CO_3^-} + \mathrm{Au} + e^- \tag{5}$$

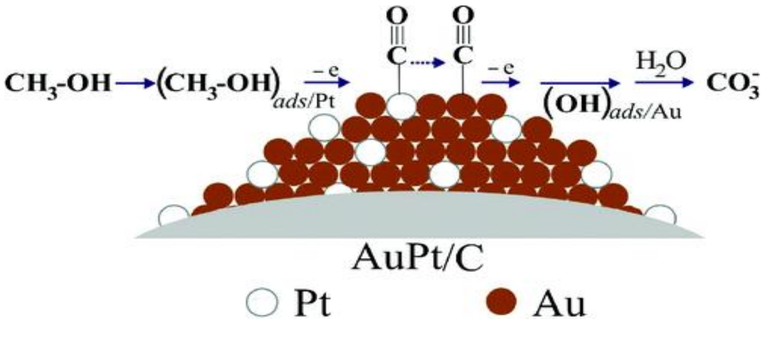

Figure 2.1: Schematic representation of MeOH oxidation by Au-Pt/C (Luo *et al.*, 2006).

2.2 SUPPORT MATERIALS FOR ELECTRO-CATALYSTS

Carbon materials are the most widely used support for fuel cell electro-catalysts due to its various properties. These properties include corrosion resistance, anisotropic electronic property, formation of intercalation compounds, strong covalent bond formation with variety of surface modifiers and adsorbing capacity of wide variety of materials. The nature of the carbon determines the electrochemical performance of electrode catalysts. Interactions between the noble metal and the support may increase the catalyst performance. Carbon black, Vulcan XC-72 is the most common support material for fuel cell electro-catalysts. But nowadays various carbon materials have been investigated as electro-catalyst's support like carbon nanofibers, carbon nanotubes, carbon aerogels and ordered nanoporous carbon (micro and mesoporous carbon).

2.2.1 Carbon Nanotubes (CNTs)

CNTs are generally synthesized by template method (Fig. 2.2), carbon- arc discharge, laser ablation of carbon or chemical vapor deposition. Kyotani *et al.* (1995) successfully prepared carbon nanotubes by template method involving carbon deposition from propylene gas at 800 °C on the inner walls of the nano-sized channels of an anodic aluminum oxide film. Carbon deposition followed by dissociation of the aluminum oxide either by HF at room temperature or by NaOH aqueous solution at 150 °C. The surface functionalization of CNTs before metal deposition was important for achieving optimal interaction between the support and the catalyst precursor. Widely, nitric acid is used to modify the CNTs surface in order to create acid sites on the surface, which can act as a nucleation center for metal ions.

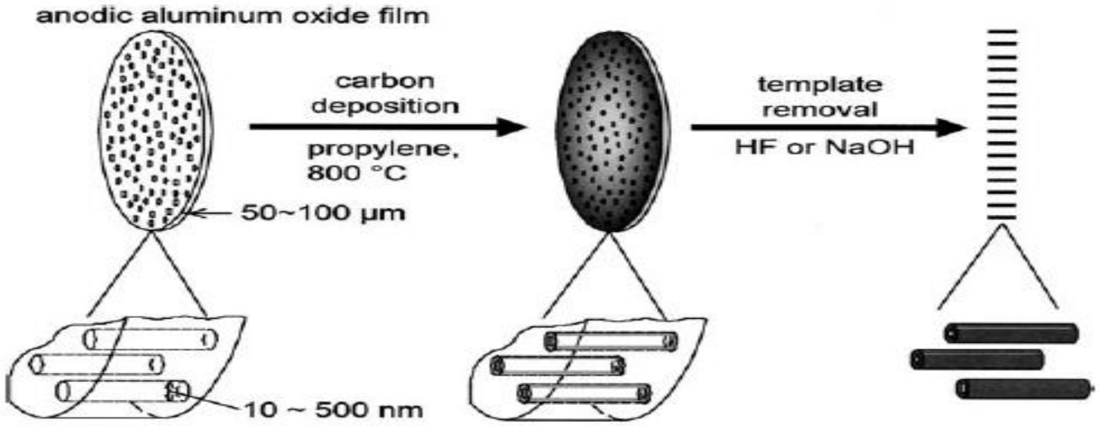

Figure 2.2: Preparation of CNT by a template carbonization technique (Kyotani *et al.*, 1996).

2.2.2 Ordered Porous Carbons

International Union of Pure and Applied Chemistry (IUPAC) classified porous carbon materials based on their pore sizes: microporous < 2 nm, mesoporous 2-50 nm and macroporous > 50 nm. Ordered nanoporous carbons have been synthesized using various templates, including silica nanoparticles, zeolites, and anodic alumina membranes and mesoporous silica materials. The porous carbons are generally synthesized by nanocasting method. The synthesis procedure includes incorporation of the pores of the template with the appropriate carbon precursor, its carbonization and subsequent removal of the template (Lee *et al.*, 2006).

Ordered Nanoporous Carbons (ONC): For the synthesis of microporous carbon materials with ordered pore structure, rigid inorganic templates are required (Fig. 2.3). Zeolites are highly crystalline aluminosilicate materials which possess uniform and ordered pore structure.

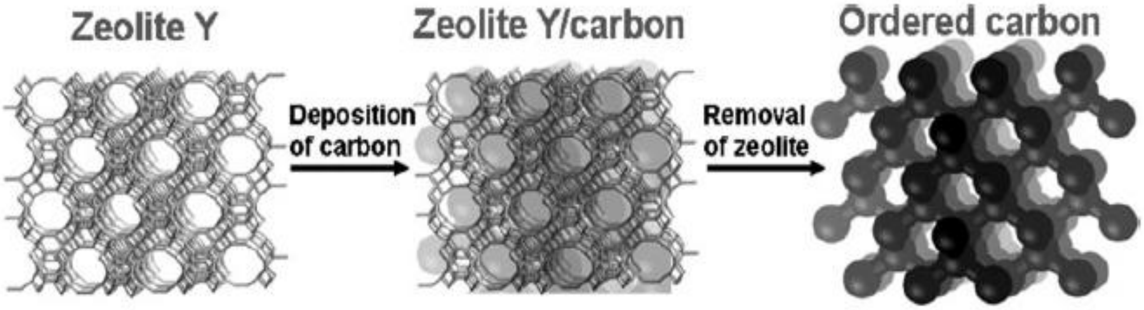

Figure 2.3: Schematic representation of synthesis of carbon from zeolite. (Lee *et al.*, 2006).

Kyotani *et al.* (1988) have first synthesized highly ordered graphite from ployacrylonitrile (PAN) by a using 2D-space between montmorillonite lamellae. A MONT-PAN intercalation compound was prepared and heat treated at 700 °C to produce carbon from PAN between MONT lamellae. The carbon was then removed by acid treatment and heat treated at different temperature up to 2800 °C. Kyotani *et al.* (1997) reported the preparation of microporous carbons using zeolite Y as a template and acrylonitrile/ furfural alcohol/propylene as a carbon precursor. The resulting microporous carbons are having BET surface area of over 2000 m^2/g. But they have failed to produce an ordered microporous carbon because while removing the template (by HF washing), carbon framework had been collapsed. The resulting carbon structure contained considerable amount of mesopores. In order to avoid the structural collapse of carbon framework, Ma *et al.* (2000) have employed two- step carbonization method. In this method, ordered microporous carbon was prepared by filling as much as carbon precursors into the zeolite pores. Additional incorporation of carbon precursor was achieved by chemical vapour deposition of propylene gas. In the first step, carbon precursor (Furfural alcohol) was incorporated into zeolite Y.

The mixture was stirred for more than 5 days, filtered and followed by washing with mesitylene to remove the carbon precursor from the external surface of the zeolite. The FA/zeolite was polymerized by heating at 150 °C under N_2 flow. The resultant composite was heat treated at 700 °C for 4 h to carbonize the polymer in the zeolite pores. After this temperature had been increased to 800 °C and propylene gas was passed for 4 h. In the second step, pyrolytic carbon was deposited into the remaining pores of the zeolite. After this, carbon/zeolite composite was washed with HF and HCl solution to remove the template framework. The carbon, so produced had almost no mesoporosity. This is confirmed by N_2-adsorption isotherm. XRD result showed some amorphous peak of carbon at 23°. This peak can be due to partial collapse of the carbon framework and/or due to the presence of graphitic domains deposited outside the zeolite pore system (Xia *et al.,* 2010). Ma *et al.* (2001) improved the synthesis of ordered microporous carbon by additional heat treatment after the propylene gas CVD. The ordered microporous carbon prepared by this method exhibits BET surface area of 3600 m^2/g.

Apart from zeolite, metal organic framework (MOF) can also be used as a template for microporous carbon. Liu *et al.* (2008) have synthesized microporous carbon by heating the carbon precursor within the pores of MOF-5 followed by carbonization and removal of template (Fig. 2.4). The MOF-5 templated carbon exhibits high BET surface area (2872 m^2/g) and pore volume (2.06 cm^3/g), but contained both micropores and mesopores. The presence of mesopores may be due to the void formation or partial filling of carbon precursor into the MOF-5. The MOF-5 templated carbon exhibits hydrogen uptake as well as excellent electrochemical properties as an electrode material.

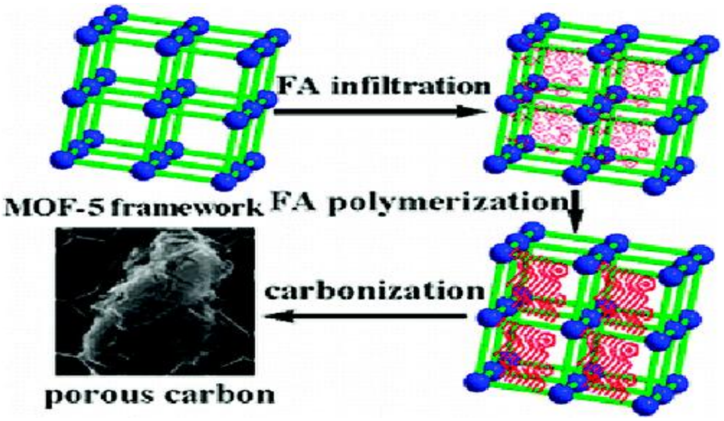

Figure 2.4: Schematic representation of nanoporous carbon from MOF-5 (Liu *et al.,* 2008).

Ordered Mesoporous Carbons (OMC): Ryoo *et al.* (1999) have first reported the synthesis of mesoporous carbon. The schematic representation of synthesis of OMC from silica is shown in Fig. 2.5. The synthesis was performed using sucrose as the carbon precursor and mesoporous silica molecular sieve (MCM-48) as a template with sucrose and sulfuric acid followed by polymerization, carbonization and the removal of the silica template. The resultant mesoporous carbon was named as CMK-1, which had different structural symmetry from that of the silica template. On the other hand, Hyeon's group (1999) used aluminium implanted MCM-48 as a template and phenol as the carbon precursor. The generated carbon was designated as SNU-1, which exhibited excellent performance as an electrochemical double layer capacitor (Lee *et al.*, 1999).

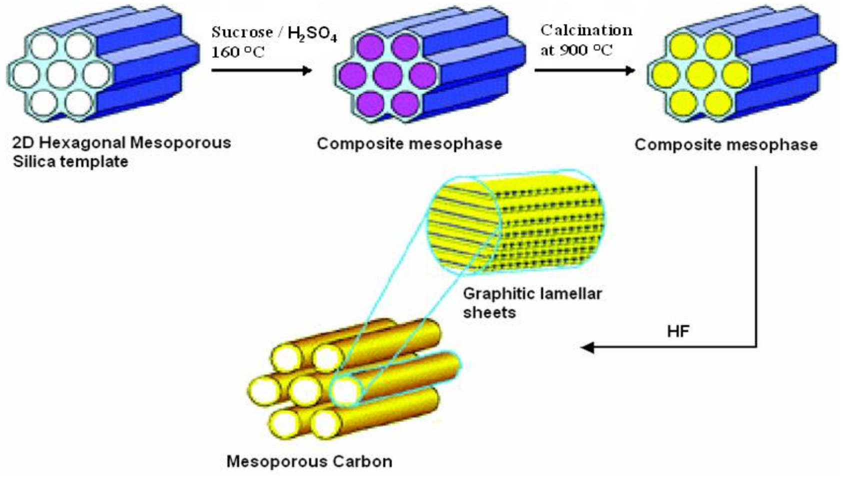

Figure 2.5: Schematic representation of synthesis of OMC from silica.

Ryoo *et al.* (2000) have synthesized hexagonally ordered mesoporous carbon (CMK-3) by using ordered mesoporous silica molecular sieve SBA-15 as a template, sucrose as the carbon precursor and sulfuric acid as the carbonization catalyst. The structure of CMK-3 carbon is an inverse replica of silica template. Depending on the degree of pore filling of the carbon precursor into the hexagonal pores of SBA-15, different carbon structure can be obtained. If the pores of SBA-15 are completely filled, CMK-3 is generated, in which carbon nanorods are interconnected by spacers. On the other hand, if the pore system of SBA-15 is partially filled with carbon precursor, CMK-5 is obtained with an array of hollow carbon tubes (Lei *et al.*, 2008). Table 2.1 summarizes the mesoporous carbons generated using nanocasing method.

Table 2.1: List of the reported ordered mesoporous carbons (Lu and Schüth, 2006).

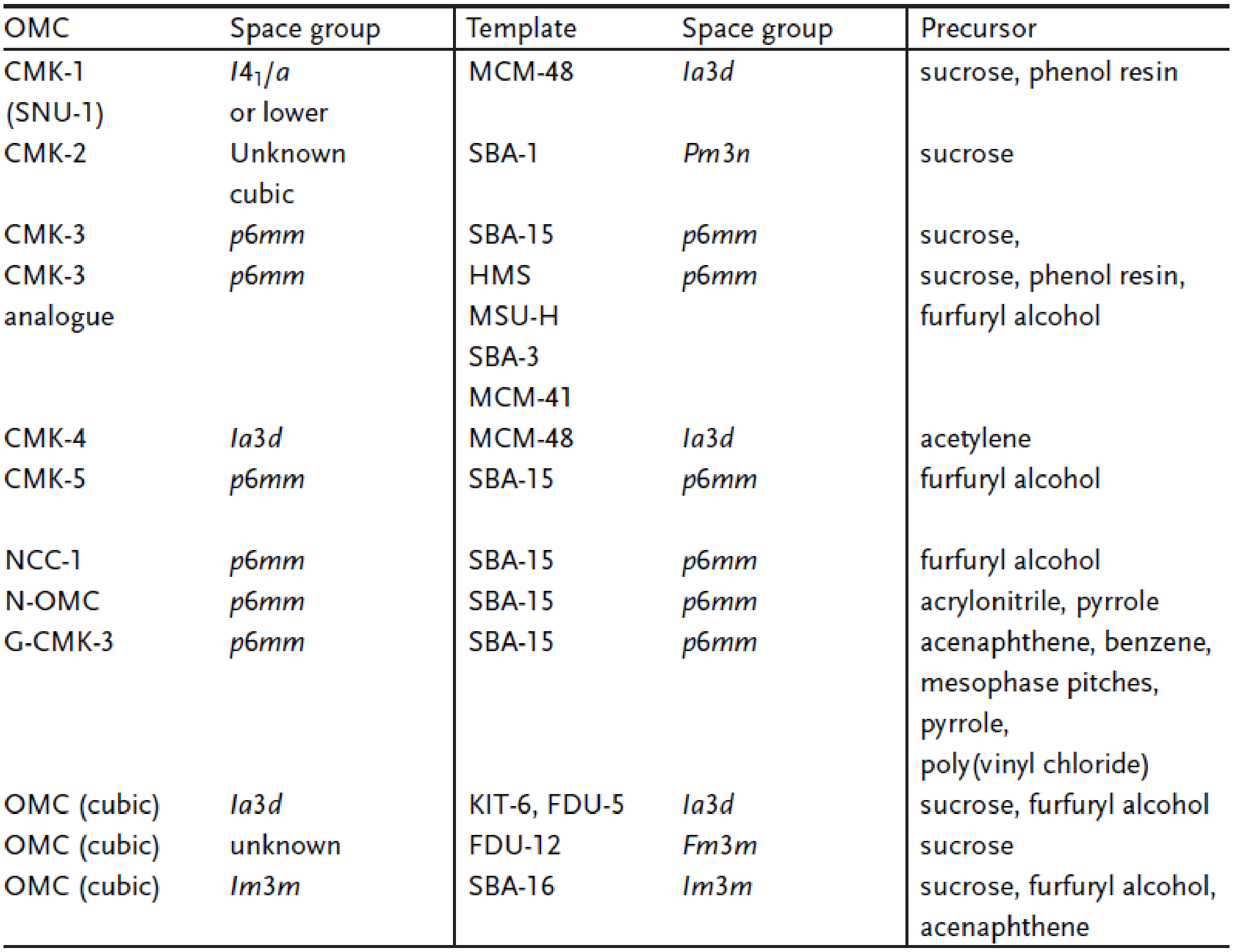

OMC	Space group	Template	Space group	Precursor
CMK-1 (SNU-1)	$I4_1/a$ or lower	MCM-48	*Ia3d*	sucrose, phenol resin
CMK-2	Unknown cubic	SBA-1	*Pm3n*	sucrose
CMK-3	*p6mm*	SBA-15	*p6mm*	sucrose,
CMK-3 analogue	*p6mm*	HMS MSU-H SBA-3 MCM-41	*p6mm*	sucrose, phenol resin, furfuryl alcohol
CMK-4	*Ia3d*	MCM-48	*Ia3d*	acetylene
CMK-5	*p6mm*	SBA-15	*p6mm*	furfuryl alcohol
NCC-1	*p6mm*	SBA-15	*p6mm*	furfuryl alcohol
N-OMC	*p6mm*	SBA-15	*p6mm*	acrylonitrile, pyrrole
G-CMK-3	*p6mm*	SBA-15	*p6mm*	acenaphthene, benzene, mesophase pitches, pyrrole, poly(vinyl chloride)
OMC (cubic)	*Ia3d*	KIT-6, FDU-5	*Ia3d*	sucrose, furfuryl alcohol
OMC (cubic)	unknown	FDU-12	*Fm3m*	sucrose
OMC (cubic)	*Im3m*	SBA-16	*Im3m*	sucrose, furfuryl alcohol, acenaphthene

Lee *et al.* (2000) have reported the synthesis of new type of high surface area mesoporous carbon using hexagonal mesoporous silica (HMS) aluminosilicate as a template. The pores of HMS are 3D interconnected. HMS templated carbon was named as SNU-2. HMS template uses cheap primary alkyl amines as a structure directing agent. The advantages of using HMS as a template includes, a shorter synthesis time, no hydrothermal reaction and high silica recovery. Ryoo and co-workers (2005) synthesized ordered mesoporous carbons with cubic Im3m structure using sucrose, furfural alcohol and acenaphthene as the carbon precursor and mesoporous silica SBA-16 as a template. This study showed that, sucrose is not suitable for the formation of rigidly interconnected pores through cage-like silica SBA-16. When furfural alcohol was used as a carbon source, cubic Im3m structure can be retained in the resulting carbon (Kim *et al.,* 2005). On the other hand, liquid crystalline mesophases can also be prepared in non-aqueous solution. This appears to be one of the most promising routes to the formation of non-silica mesoporous solids. Such soft-templating is defined as a process in which organic molecules serve as a 'mold' and around which a framework is built up (Fig. 2.6).

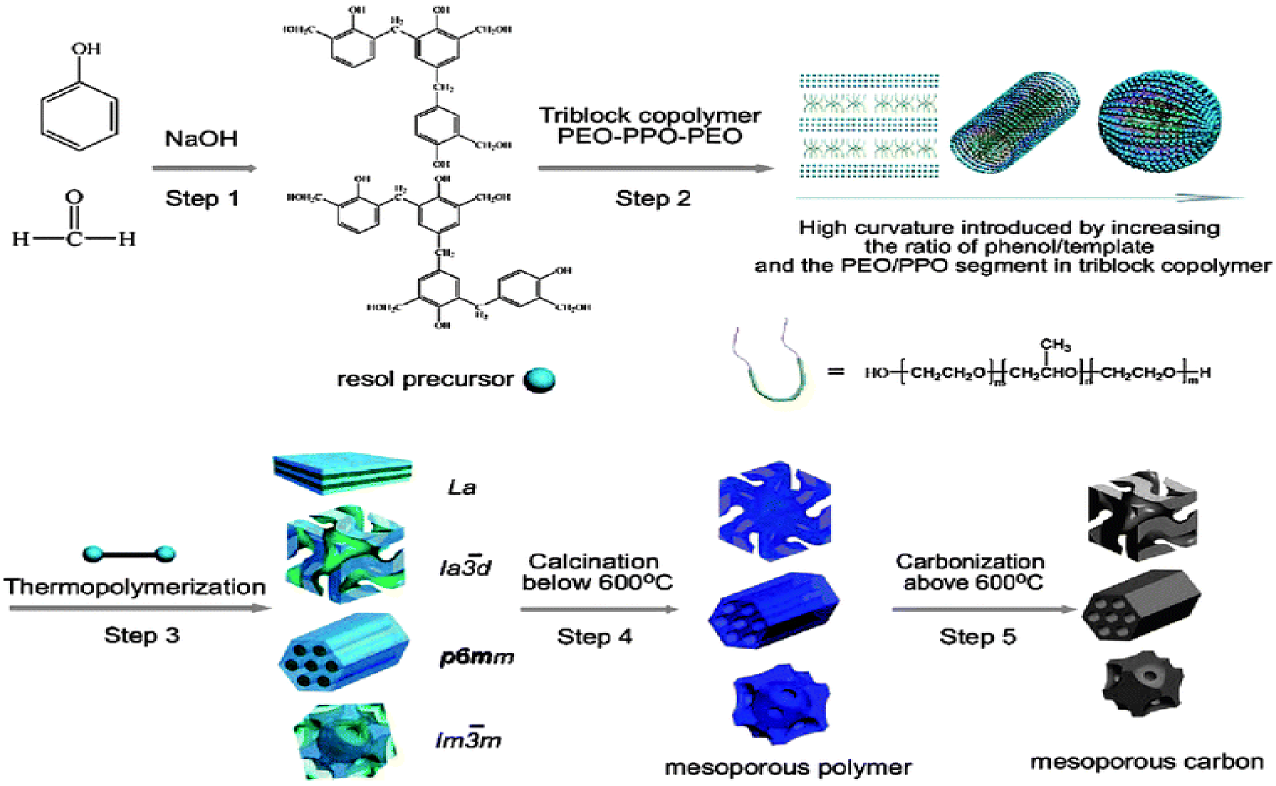

Figure 2.6: Schematic representation of the preparation of ordered mesoporous polymer resins and carbon frameworks (Meng *et al.,* 2006).

2.2.3 Graphenes

In comparison with CNTs, graphene nanosheet (GNS) has not only contains similar stable physical properties, but also contains large surface area (2620 m^2/g). It can be considered as a plat CNTs. GNS has been reported to have good dispersion stability and large surface area. GNS supported catalyst possesses larger electrochemical surface area (47.9 m^2/g) than the Vulcan supported catalyst (28.3 m^2/g) and it can be attributed to the size of PtRu particles well loaded on GNS. Preparation of GNS based catalyst is shown in Fig. 2.7. Normalized current density (considering electrochemical surface area at 700 mV) of PtRu/GNS and PtRu/VC are 0.113 and 0.0812 mA g/m^2 respectively. The increase in electrochemical activity of PtRu/GNS can be attributed to dispersed particle size effect and large electrochemical surface area (Bong *et al.,* 2010).

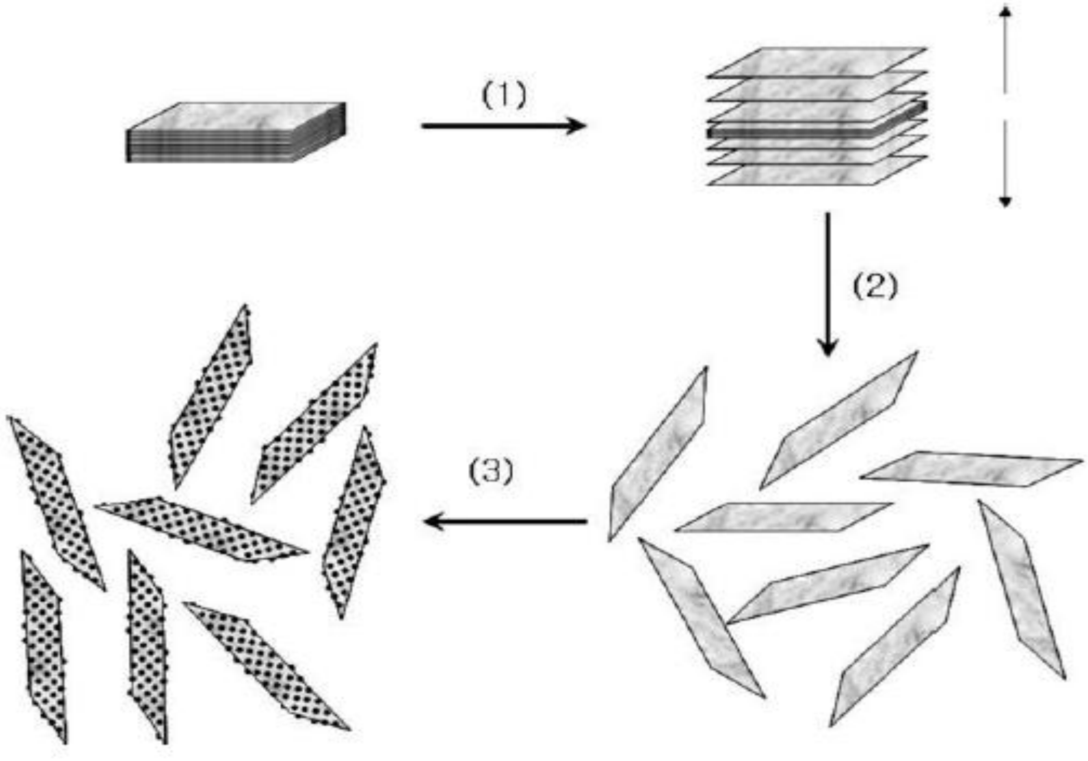

Figure 2.7: Schematic representation of synthesis of graphene nanosheet supported catalyst.
(1) Oxidation of graphite to graphite oxide with larger inter layer distance,
(2) Exfoliation of graphite oxide by ultrasonication and
(3) Preparation of GNS based catalyst by colloidal method (Bong *et al.*, 2010).

2.2.4. Onion-like fullerenes (OLFs)

OLFs have been synthesized by chemical vapor deposition of ferrocene in a mixed stream of C_2H_2 and Ar at 1100 °C (Wang *et al.,* 2006). Xu *et al.* (2006) have reported the onion-like fullerenes as a support material for direct methanol fuel cell. Pt/OLFs catalysts were synthesized by an impregnation-reduction method. The Pt metal supported on OLFs had 3.05 nm, whereas Pt supported on Vulcan carbon had 4.10 nm metal particle sizes. Pt/OLFs exhibit 20 % higher current density at 0.78 V compare to Pt/Vulcan XC-72. The higher catalytic activity of the Pt/OLFs can be attributed to smaller particle size.

2.3 OTHER APPLICATIONS OF POROUS CARBONS

2.3.1 Hydrogen Storage

Hydrogen has been considered as an alternative fuel and energy carrier. However, the storage and transportation have become the major limiting factors for hydrogen economy. Among all the available fuels, hydrogen is having high calorific value per unit weight. The US Department of Energy (DOE) has targeted 6.0 wt.% hydrogen storage by 2010 and 9 wt.% by 2015. An efficient and effective storage medium for hydrogen is required for the application of hydrogen in fuel cells and as an energy carrier (Viswanathan and Scibioh, 2006). The maximum value of hydrogen adsorption depends on the amount of hydrogen that can be accommodated in a monolayer. There are multiple ways to store hydrogen, including compressed gas, liquefaction, metal hydrides, complex hydrides and porous adsorbents. The most necessary requirements for a hydrogen storage system are, to pack hydrogen as close as possible and reversibility of uptake and release. But actually none of these techniques are capable of satisfying all the criteria of size, efficiency, cost, kinetics and safety required for the transport applications. The drawbacks of the high pressure storage method are relatively low hydrogen density and very high gas pressure. Liquefaction method requires large amount of energy.

Among them carbon materials have attracted lot of attention for hydrogen storage due to its adsorption ability, fast kinetics, complete reversibility, low cost and mainly high surface area, pore microstructure and low mass density. Textural parameters (surface area, pore volume and pore size) and surface properties (functionality) are determining the hydrogen storage capacity of porous carbon. The hydrogen storage values are dependent on many parameters of the carbon nanotubes, including their structure, structure defects, pretreatment, purification, geometry (surface area, tube diameter and length), arrangement of tubes in bundles, storage pressure and temperature (Wang *et al.*, 2009).

Activated carbon is extensively studied as a hydrogen storage medium due to its storage properties. The hydrogen storage capacity of activated carbon varies linearly with specific surface area of the activated carbon (Rzepka and Lamp, 1998). The nanostructured carbon materials like carbon nanotubes (CNTs) and graphite nanofibers (GNFs) exhibit high hydrogen storage capacity (HSC). Hydrogen molecules can be located inside the nanotubes or interstitially between them. The maximum possible HSC in CNTs is about 5-7 wt.% with all the necessary conditions (Hirscher *et al.*, 2002). Some reports show greater than 7 wt.% storage capacities. But these results are not reproducible.

Hydrogen storage in CNTs can be measured by gravimetric method, volumetric method and thermal desorption spectroscopy. Gravimetric method measures the weight changes of the specimen due to absorption or desorption of hydrogen. Volumetric method measures the pressure drop due to hydrogen adsorption. Thermal desorption spectroscopy measures only the hydrogen desorption in high vacuum using mass spectrometry (Fan *et al.*, 1999). Chambers *et al.* (1998) reported 67 wt.% of hydrogen storage using GNF herringbone and 54 wt.% by GNF platelet. GNF herringbone has higher storage capacity due to its geometric structure.

2.3.2 Capacitor

A capacitor is a device that stores electrical charge as well as potential energy. The amount of energy stored is equal to the work done to charge it. Capacitors have many electronic applications like storing electric potential energy, delaying voltage changes when coupled with resistors, filtering out unwanted frequency signals, forming resonant circuits and making frequency–dependent and independent voltage dividers when combined with resistors. On the basis of electrode material and storage mechanisms, electrochemical capacitors are as classified as electrochemical double-layer capacitors (EDLCs) that employ high surface area carbon and pesudocapacitors (supercapacitors) in which transition metal oxide or conducting polymers are used as electrodes (Kim and Kim, 2006). EDLCs are one of the promising candidates for potential application in electric vehicles and other high power applications. Activated carbon is mostly explored as a capacitor. However, micropores in activated carbon can be easily accessed by the electrolyte and the exposed surface in micropores is not suitable for charge storage at high loading current density. Recently, highly ordered mesoporous carbons (HOMCs) have received much attention due to their well-defined structure and high surface area. Yuan *et al.* (2009) have reported synthesis of highly ordered mesoporous carbon via in situ template method for supercapacitors. They followed the one-step synthesis of HOMC using diluted sulfuric acid as cross-linked reagent, P123 and sucrose as the carbon precursor. The resulting ordered mesoporous carbon exhibits high surface area (1628 m^2/g) and high specific capacitance (161 F/g) at low sweep rate of 5 mV/s. And this specific capacitance does not decay in the range from 1 to100 mV/s, specifies its capability of fast ion diffusion within the mesoporous structure.

Chen *et al.* (2009) have reported the synthesis of mesoporous carbon spheres (MCSs) via a hydrothermal route. Monodisperse carbon spheres (CSs) have been synthesized via a hydrothermal method using glucose as the carbon precursor without any catalysts. The CSs with high surface area obtained with large number of hydrophilic groups by treatment with molten KOH. Single electrode of MCs has higher specific capacitance of 253 F/g. This value increases by 20 % after the introduction of Pt nanoparticles. 10 wt.% Pt loading on MCs has been shown higher specific capacitance of 302 F/g.

Chen *et al.* (2010) have demonstrated the usage of graphene oxide supported needle-like MnO_2 nanocomposites (GO-MnO_2) as supercapacitors. Graphene is having monolayer arrangement of carbon atoms in a honeycomb network and it can be considered as an unrolled CNT. They have fabricated GO-MnO_2 composite through a simple chemical route (in a water–isopropyl alcohol system) without the usage of templates or surfactants. Intercalation and adsorption of manganese oxide into the GO sheets is followed by the nucleation and growth of the crystal species in a double solvent system, which results in exfoliation of GO sheets. Electrochemical properties can be enhanced by the chemical interaction between GO and $MnO_{2.}$ The GO-MnO_2 composite exhibits good electrochemical behavior and that can be used as supercapacitor.

CHAPTER 3

EXPERIMENTAL METHODS

3.1 STARTING MATERIALS

Hexachloroplatinic acid (Sigma) and 5 wt.% Nafion solution (Sigma) were used for the electro-catalyst and electrode preparation, respectively. Mordenite and Zeolite Y (NaY) (Sud-Chemie) were used as template materials. Analytical grade of sulphuric acid (98%; Merck) was used as electrolyte for CV analysis. Analytical grades of solvents like acetone, ethanol and methanol were purchased from (SISCO). High pure N_2, O_2 and H_2 gases were used for heat treatment, ORR and reduction processes (99.95 %; Indian Oxygen).

3.2 CHARACTERIZATION TECHNIQUES

3.2.1 X-ray diffraction (XRD)

XRD patterns of the samples were recorded on Rigaku miniflex (II) X-ray diffractometer using Cu K_α (λ= 1.5405 Å). The crystallite size was calculated by X-ray line broadening method using Debye-Schrrer equation (Cullity, 1978),

$$d = K\lambda / (\beta \cos\theta) \qquad (3.1)$$

where, d is the crystallite size in nm, K is the numerical constant, 0.86, λ is the wavelength of radiation used, β is full width at half maximum in radians and θ is the Bragg diffraction angle in degrees, at the peak maximum. The XRD patterns were recorded at the scan rate of 3°/min, sampling width of 0.02° for the 2θ range of 5-90°.

3.2.2 BET surface area measurements

Nitrogen adsorption/desorption studies were carried out with Micromeritics ASAP2020. Surface area of the sample was calculated using BET equation. Degassing of the sample was done at 373 K for 2 h and at 423 K for 3 h.

3.2.3 Scanning electron microscopy (SEM)

Scanning electron micrographs were recorded using FEI, Quanta 200F (30 kV). The samples in the powder form were taken on the carbon tape and mounted on the SEM sample holder and images were recorded.

3.2.4 Transmission electron microscopy (TEM)

Transmission electron micrographs were recorded on a Philips CM20 model (200 kV). Few milligrams of the samples (1-2 mg) were dispersed in few mL (1-2 mL) of ethanol by ultrasonication for 15 minutes and a drop of the dispersion was placed on a carbon coated copper grid and allowed to dry in air at room temperature.

3.2.5 X-ray photoelectron spectroscopy (XPS)

The X-ray photoelectron spectroscopic studies were performed using Omicron Nanotechnology instrument using Mg Kα radiation. The base pressure of the analysis chamber during the scan was $2*10^{-10}$ milli bar. The pass energies for individual scan and survey are 20 and 100 eV, respectively. The spectrums were recorded with step width of 0.05 eV.

3.2.6 Electrochemical measurements

BAS Epsilon Potentiostat was used for the electrochemical studies. All the electrochemical measurements were performed with three electrode cell assembly, consists of electro-catalyst coated glassy carbon disk (dia. = 0.3 cm, geometrical surface area = 0.07 cm^2) as the working electrode, Pt foil (1.5 cm^2) as the counter electrode and SCE as the reference electrode. Cyclic voltammetric studies for hydrogen adsorption/desorption charge determinations were conducted in 1M H_2SO_4. CV and chronopotentiometric studies were carried out in 1M methanol and 1M sulphuric acid. The working electrode was fabricated by dispersing 10 mg of the catalyst in 1 mL of distilled water by ultrasonication for 15 min. 10 μL of the dispersion was placed on 0.07 cm^2 of the glassy carbon electrode, and dried in an oven at 80 °C for a few minutes. Then, the resulting dried catalyst ink was coated with 5 μL of 5 wt.% Nafion solution followed by drying in an oven for a few minutes.

<u>*Determination of Electrochemical Active Surface Area (EAS)*</u>*:* Cyclic voltammetry was employed to obtain electro-active surface area of the electrode materials in order to account for the higher current response in methanol oxidation. Fig. 3.1 depicts a model cyclic voltammogram obtained in 1M H_2SO_4 between -0.2 V and + 1.0 V Vs SCE at a scan rate of 50 mV/s. All the prepared Pt catalysts exhibits the hydrogen adsorption and hydrogen desorption peaks between -0.2 V and + 1.0 V. The active Pt surface area of the electrodes was evaluated from the columbic charge for hydrogen desorption (Q_H) of the electrode. The value of Q_H was calculated as the mean value between the amounts of charges exchanged during the electro adsorption and desorption of hydrogen on Pt sites. The area which can be used for the ESA calculation is shown in Fig. 3.1. The electrochemical active surface area of the Pt/C catalyst was determined from the charge for hydrogen adsorption/desorption using equation 3.2. A model calculation for EAS is given in the subsequent section.

Electrochemical active surface area (EAS) (m^2/g)

$$= \quad QH/\,([Pt] \times 0.21) \qquad \ldots\ldots\ldots\ldots\ldots (3.2)$$

Q_H – Average charge for hydrogen adsorption/desorption in mC/cm^2
[Pt] – loading of platinum in mg/cm^2
0.21 – charge (in mC) required to oxidize one monolayer of hydrogen from 1 cm^2
of platinum black (Ralph *et al.,* 1997; Pozio *et al.,* 2002).

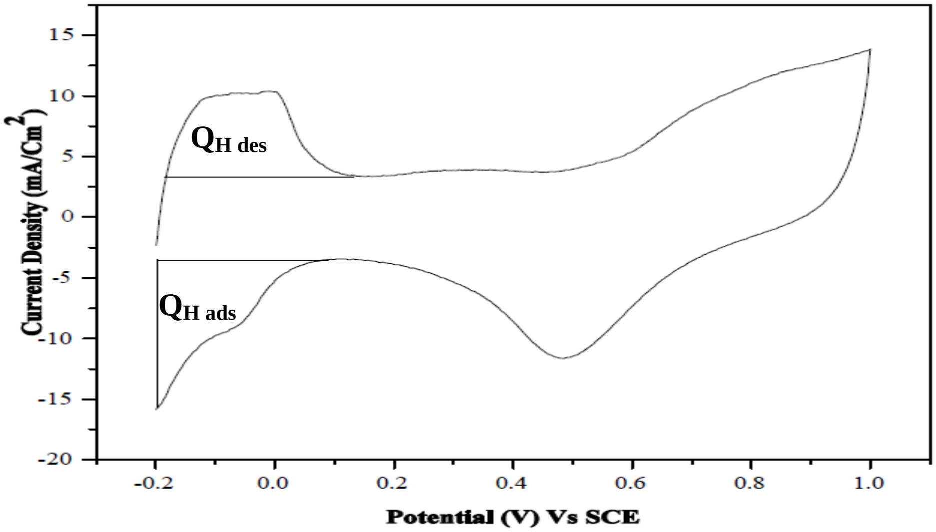

Figure 3.1: A model Cyclic Voltammogram of Pt/C catalyst in 1M H_2SO_4 at room temperature (scan rate: 50 mV/s).

Calculation of [Pt] - Pt Loading

100 mg catalyst contains 20 mg Pt
10 mg catalyst contains = (10/100) x 20 = 2 mg of Pt

2 mg of Pt is dispersed in 1 ml (1000 μl) of distilled H_2O, and 10 μL of the dispersion is dispensed on 0.07 cm^2 area of glassy carbon electrode.

10 μL contains = (2 mg/1000) x 10 μL = 0.02 mg Pt

Pt loading (mg /cm^2) = (0.02/0.07) = **0.286**

<u>Charge calculation for hydrogen desorption</u>

No. of square units during hydrogen desorption = 122

Area of each square unit = 122 x 8.33 x 0.123 (mA/cm^2) x mV

= 125 (mA/cm^2) x mV

Charge during hydrogen desorption = [125 (mA/cm^2) x mV] / 50 mVs^{-1}

= 2.5 (mA/cm^2)s

= [2.5 (mA/cm^2)s]/3600

= 6.94 x 10^{-4} mA.h/cm^2

26.8 Ah = 96500 C

Charge (mC/cm^2) = [(6.94 x 10^{-4} mA.h/cm^2) x 96500]/ 26.8

= 2.5 mC/cm^2

<u>Charge calculation for hydrogen adsorption</u>

No. of square units during hydrogen adsorption = 302

Area of each square unit = 302 x 8.33 x 0.123 (mA/cm^2) x mV

= 309.4 (mA/cm2) x mV

Charge during hydrogen adsorption = [309.4 (mA/cm^2) x mV] / 50 mVs^{-1}

= 6.19 (mA/cm^2)s

= [6.19 (mA/cm^2)s]/3600

= 1.72 x 10^{-3} mA.h/cm^2

26.8 Ah = 96500 C

Charge (mC/cm^2) = [(1.72×10^{-3} $mA.h/cm^2$) x 96500]/ 26.8

= 6.19 mC/cm^2

Average Q_H = [2.5 + 6.19]/2 = 4.345 mC/cm^2

[Pt] = 0.286 mg/cm^2

EAS = 4.345/[0.286 x 0.21] = 72.34 (mC/cm^2)/[mg/cm^2 x mC/cm^2]

= 72.34 cm^2/mg = 72.34×10^{-4} $m^2/10^{-3}g$

EAS = 7.23 m^2/g

Determination of Mass Specific Activity: Mass Specific Activity of the Pt/C catalyst was determined using equation 3.3. The current density (forward peak current density) for methanol oxidation is obtained from the cyclic voltammogram of the catalyst in 1M methanol and 1M H_2SO_4.

Mass Specific Activity (mA/ mg) = current density (mA/cm^2)/ Pt loading (mg/cm^2)...............(3.3)

Determination of Specific Activity:

Specific activity was determined using equation 3.4.

Specific Activity (A/m^2 of Pt) = Mass Specific Activity (A/g)/EAS (m^2/g)………………….(3.4)

CHAPTER 4

ORDERED NANOPOROUS CARBON (CNPI-1) AND NITROGEN-CONTAINING CARBON (NCNPI-1)

4.1 INTRODUCTION

Porous materials have both continuous skeletons and voids that can be randomly arranged (disordered pore system) or highly regular (ordered pore system) with large surface areas. According to the definition of IUPAC (International Union of Pure and Applied Chemistry), porous materials can be divided into microporous (with pore diameter < 2 nm), mesoporous (pore size in the range of 2-50 nm) and macroporous materials (pore size >50 nm). Porous carbon materials form a large and important class of porous materials, which have been widely used for gas separation, water purification, catalyst supports, shape-selective catalysis, chemical separations and electrodes for electrochemical double layer capacitors and fuel cells (Lee *et al.*, 2006; Lu *et al.*, 2010).

Porous carbon materials constitute a very flexible set of supports for the preparation of heterogeneous catalysts. Their physical and chemical surface properties can easily be tailored to develop a large surface area to disperse the active phases, the proper pore size distribution to facilitate the diffusion of reactants and products to and from the surface, and the acid–base character needed for obtaining the best performance. The use of carbon as a catalyst support depends primarily on the relative inertness of its surface, which facilitates the interaction between active phases or between active phases and promoters, thus enhancing the catalytic behavior. This makes porous carbons an excellent choice as catalyst support in a great number of reactions.

Carbon materials are the most widely used support for fuel cell electro-catalysts due to its various properties. These properties include corrosion resistance, anisotropic electronic property, formation of intercalation compounds, strong covalent bond formation with variety of surface modifiers and adsorbing capacity of wide variety of materials. The nature of the carbon determines the electrochemical performance of electro-catalysts (Serp and Figueiredo, 2009).

Interactions between the noble metal and the support may increase the catalyst performance. Carbon material has a strong influence on the properties of the supported noble metal catalysts, such as metal particle size, morphology, size distribution, degree of alloying, stability and dispersion. Carbon supports also affect the performance of supported catalysts in fuel cells, such as mass transport, catalyst layer electronic conductivity, electrochemical active surface area, and metal nanoparticle stability during the operation. Hence, the optimization of carbon supports is very important in DMFC development.

For a fuel cell to operate efficiently, carbon materials must provide high dispersion of nanoparticles, be chemically inert and corrosion resistant, should have high electron conductance, should contain adequate porosity for the efficient mass transport of reactants and products and provide optimum water management. Carbon black, Vulcan XC-72 is the most common support material for fuel cell electro-catalyst. But nowadays various carbon materials have been investigated as electro-catalyst support like carbon nanofibers, carbon nanotubes, carbon aerogels and ordered nanoporous carbon (micro and mesoporous carbon).

Microporous carbons are widely used for gas and liquid separation, which are conventionally carried out by controlled pyrolysis of a carbon precursor or by post-modification of the existing pores. In comparison with zeolites, microporous carbons have several attractive features such as high hydrophobicity, heat resistance and high corrosion-resistance.. For preparing microporous carbons, the most important parameter is finding an efficient method to control their pore size. Microporous carbons can be prepared with well-defined pore structures through the nanocasting process. For the sake of classification, the microporous carbons are designated here as ordered nanoporous carbons (ONCs).

4.2 PREPARATION METHODS

Conventionally, there are three major methods for preparing porous carbons, including: 1) activation of carbon-containing precursors to prepare porous carbons (both physical and chemical activation); 2) carbonization of carbon-containing precursors to prepare porous carbons; 3) combination of sol-gel processes and carbonization to synthesize porous carbons; 4) the nanocasting approach to replicate porous carbons.

Although the above methods are useful for the preparation of porous carbon materials with tunable properties, such as porosity, surface area and pore volume, the synthesis of uniform porous carbon materials has been very challenging. Among the above methods, nanocasting method has been widely used for preparing micro and meso structured materials. Nanocast porous carbons have many novel properties such as high surface area, large pore volume, uniform pore size, tunable surface chemistry, and good thermal stability and electronic conductivity (Lu *et al.*, 2010).

4.3 NANOCASTING

Nanocasting is a process used to infiltrate a fluid (liquid, or even gas) precursor into the nanometer-sized pore channels of the hard templates, to convert the precursor by the nanostructure confinement into a target nanomaterial that duplicates the morphology and structure of the template, and finally to remove the template (Fig. 4.1). Various inorganic materials, including silica nanoparticles (silica sol), zeolites, anodic alumina membranes, and mesoporous silica materials, have been used as templates (Lu and Schuth, 2006).

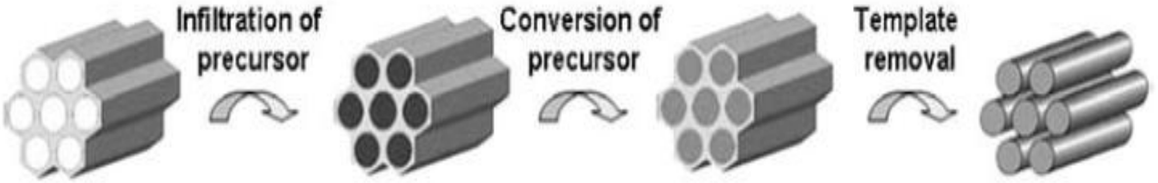

Figure 4.1: Schematic representation of nanocasting pathway, showing the change of the mesostructure during the process. The process mainly includes three steps: (1) Precursor infiltration inside mesochannels of the silica template; (2) Conversion of the precursor in the nanochannels; (3) Removal of mesoporous silica template (Lu *et al.*, 2010).

4.3.1 Zeolites as Hard Template

Zeolites are highly crystalline aluminosilicate materials which possess uniform and ordered pore structure. Since the wall thickness for zeolites is less than 1 nm, the periodic pore structures and well-defined internal nanospaces of zeolites provide opportunities to control the nanostructure and morphology of microporous carbon materials at the nanometer level. It is reasonable to expect that if such a nanospace in a zeolite is filled with carbon, the generated porous carbon should reflect the porosity of the original zeolite template. Zeolites have therefore been widely used as inorganic templates for the synthesis of microporous carbons with uniform pore sizes.

4.3.2 Use of furfural alcohol as carbon precursor

1 g of template (H-Mordenite) was impregnated with 4 ml of furfural alcohol and stirred for overnight. And then the suspension was filtered and washed with mesitylene to remove the carbon from the external surface of the template. Then the filtered sample was dried at 80 °C for 24 h and polymerized at 150 °C for 8 h. The polymerized sample was heat treated in the N_2 atmosphere at 700 °C for 3 h at the rate of 5 °C/min. After the heat treatment, the acquired sample was HF treated to remove the template and dried at 120 °C. The obtained ordered microporous carbon was designated as CNPI-1. Then the prepared CNPI-1 was characterized by XRD, BET, SEM and XPS.

4.3.3 Use of pyrrole as carbon/nitrogen precursor

Nitrogen can be introduced in carbons essentially in two ways, either by carbonizing nitrogen-containing organic compounds or mixtures of nitrogen containing precursors with nitrogen-free materials, or by treatment of carbon materials at high temperatures with nitrogen-containing gases which decompose at these temperatures with generation of highly reactive radicals. Here, carbonization of nitrogen-containing organic compounds had been followed for the preparation of nitrogen containing microporous carbon.

1 g of template (H-Mordenite) was impregnated with 4 ml of pyrrole and stirred for overnight. And then the suspension was dried at 80 °C for 3 h in an oven and then 3 h in vacuum oven for polymerization. The polymerized sample was heat treated in the N_2 atmosphere at 700 °C for 3 h at the rate of 5 °C/min. After the heat treatment, the acquired sample was HF treated to remove the template and dried at 120 °C. The obtained nitrogen containing ordered microporous carbon was designated as NCNPI-1. Then the prepared NCNPI-1 was characterized by XRD, SEM, XPS and BET. The presence of nitrogen atoms in the carbon framework generates specific surface properties including the enhanced polarity, basicity and heterogeneity

in terms of hydrophilic sites. The presence of nitrogen functional groups in the carbon framework also has a substantial effect on their catalytic activity.

4.4 CHARACTERIZATION

4.4.1 XRD

XRD patterns of the CNPI-1 samples are shown in Fig. 4.2. FA / H-MOR composite and heat treated sample retained the ordered structure of the H-Mordenite. During the HF treatment, CNPI-1 from template can collapse and form an amorphous like structure due to insufficient impregnation of the precursor. Therefore, template removal process has to be optimized to get an ordered carbon structure. In this case, HF treatment had been optimized for 2 and 5 % of HF. And also different time duration had been employed like 3, 6 and 9 h. From XRD patterns, we can conclude that, different time duration was not making significant variations in the morphology of the prepared CNPI-1.

XRD patterns of the NCNPI-1 samples are shown in Fig. 4.3. Both pyrrole/ H-MOR composite and heat treated sample retained the ordered structure of the H-Mordenite. During the HF treatment, NCNPI-1 from template can collapse and form an amorphous like structure due to insufficient impregnation of the precursor. Therefore, template removal process has to be optimized to get an ordered carbon structure. In this case, HF treatment had been optimized for 5 % of HF. And also different time duration had been employed like 1- 9 h. From XRD patterns, we can conclude that, different time duration was not making significant variations in the morphology of the prepared NCNPI-1.

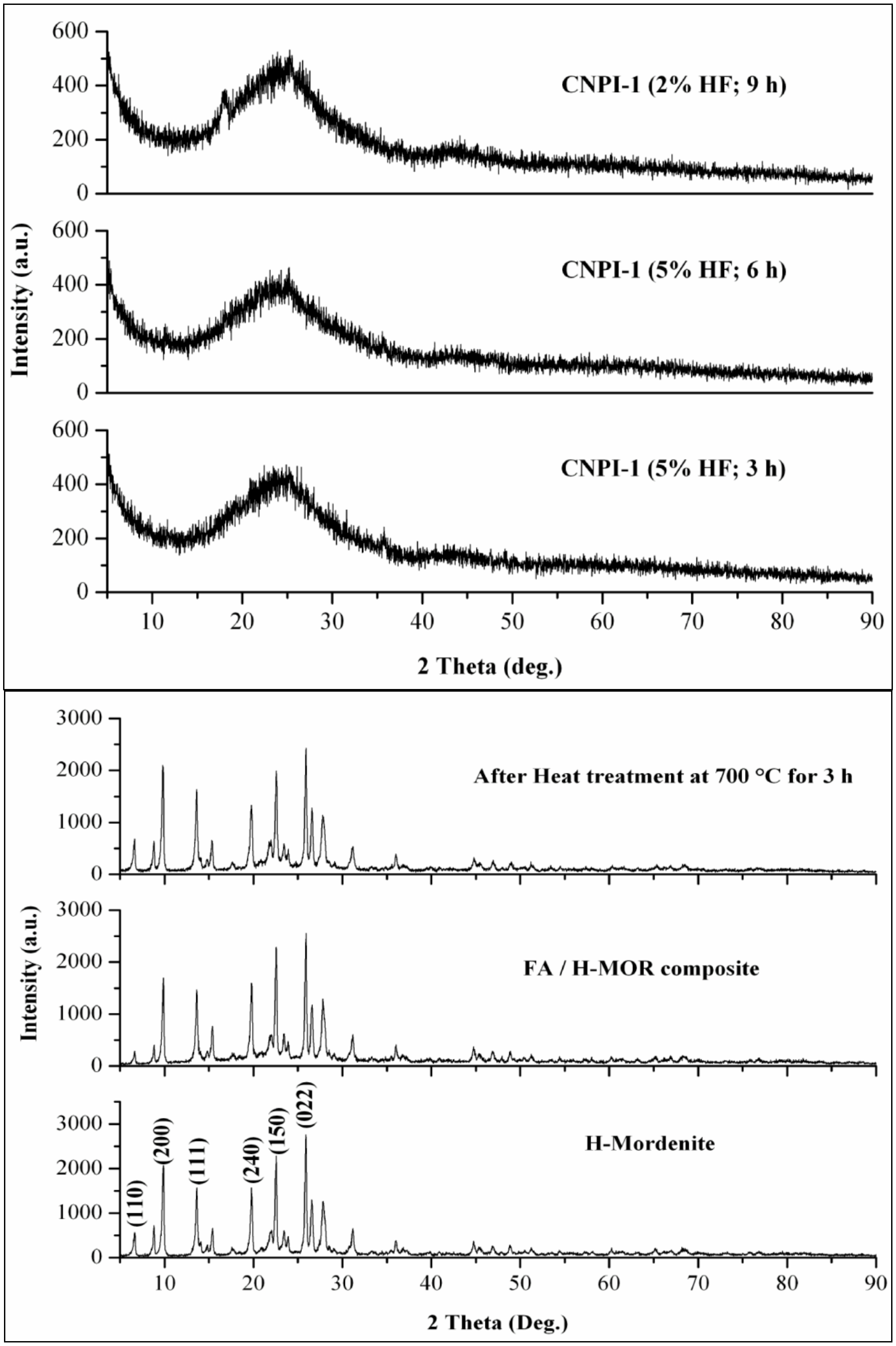

Figure 4.2: XRD pattern of CNPI-1.

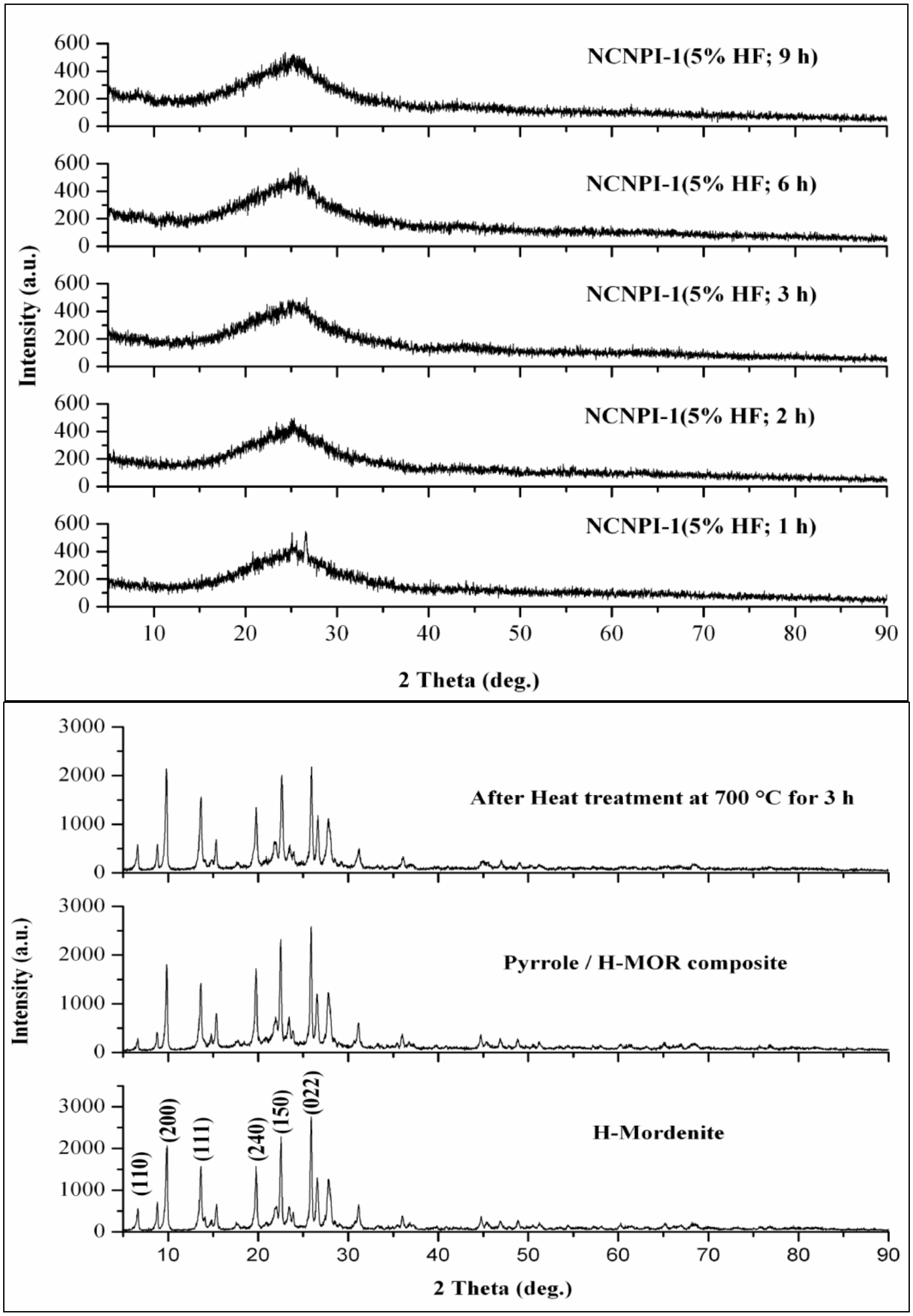

Figure 4.3: XRD pattern of NCNPI-1.

4.4.2 Textural properties

Nitrogen adsorption/desorption isotherms and pore size distributions of the CNPI-1 and NCNPI-1 are shown in Fig. 4.4 and 4.5 respectively. Textural properties of CNPI-1 and NCNPI-1 are given in Table 4.1. It is reported that the higher the degree of activation of the carbon sample, the higher is the decrease in surface area and pore volume, as increase in the degree of activation makes the pore walls thinner and thus are easily destroyed.

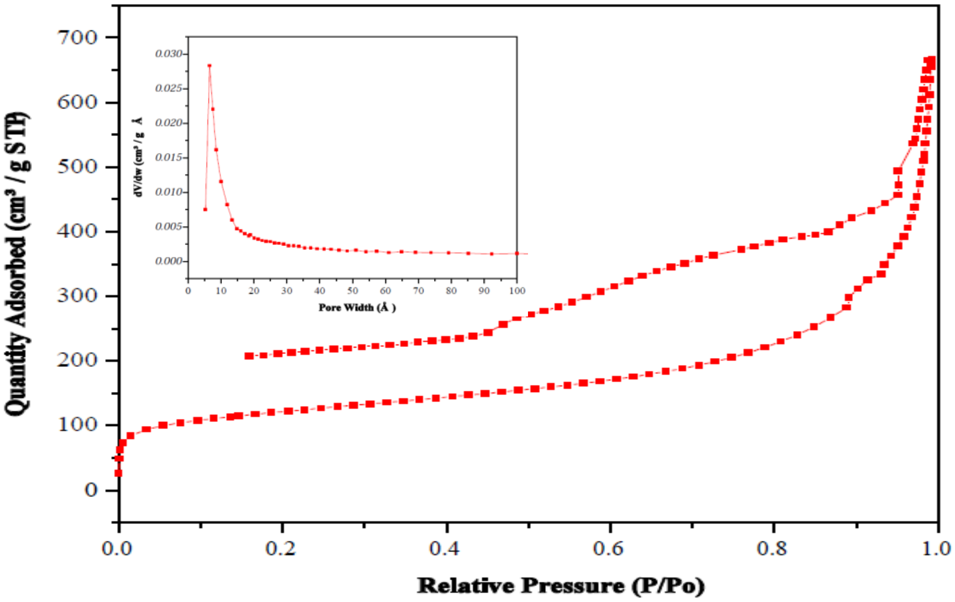

Figure 4.4: N_2 sorption isotherm of CNPI-1. Inset: Pore size distribution of CNPI-1.

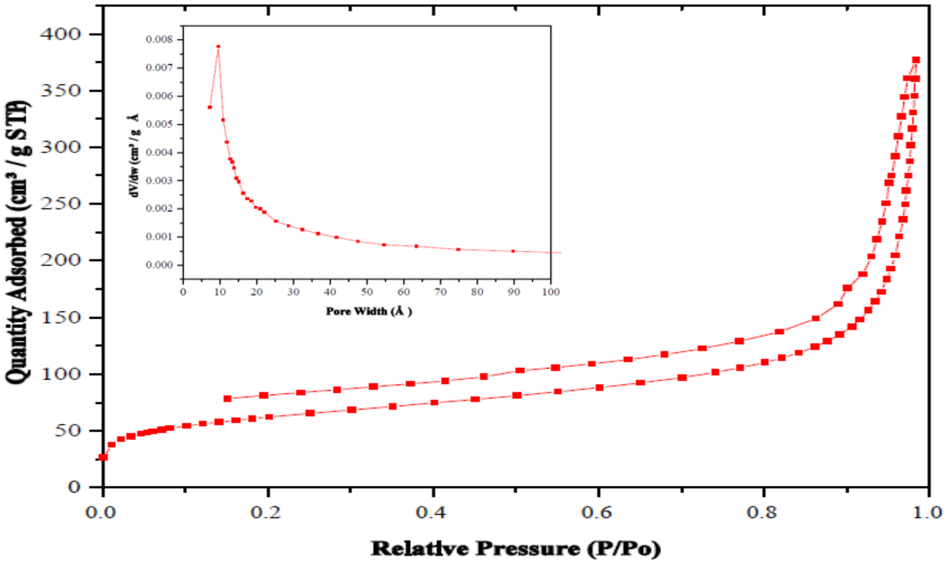

Figure 4.5: N_2 sorption isotherm of NCNPI-1. Inset: Pore size distribution of NCNPI-1.

The N_2 sorption studies on H-Mordenite templated microporous carbons showed micropores (type-I isotherm) with a significant proportion of mesopores (type-IV isotherm), and the ordered structure of the H-Mordenite was not completely transferred to the resulting carbons. This could be due to low carbon precursor loading and/or spatial restrictions (within the H-Mordenite template pores) during the precursor polymerization and limited subsequent carbon growth. The incomplete carbon infiltration and filling of the template pores implies that the resulting porous carbon was not a true replica of H-Mordenite despite its morphology, being similar to that of the H-Mordenite template.

The generation of mesopores results from the partial collapse of the carbon framework after the removal of the template by HF etching because the thin wall thickness of the carbon, derived from the small pores of the H-Mordenite template, does not exhibit a sufficiently high mechanical strength to survive the removal of the template. Therefore, both the microporous carbons contained both micropores and mesopores. Also, they had narrow pore size distribution unlike the amorphous carbon. From N_2 adsorption and pore size distribution plots, we can conclude that, the prepared microporous carbons contained an ordered pore structure. Horvath-Kawazoe differential pore volume plot was used for the pore size distribution plot. Due to the condensed nature of the NCNPI-1, BET surface area is less compared to CNPI-1 (Table 4.1).

Table 4.1: Textural properties of CNPI-1 and NCNPI-1.

Microporous carbons	BET surface area (m^2/g)	Pore volume (cm^3/g)	Avg. Pore size (Å)
CNPI-1	409	0.80	6.58
NCNPI-1	218	0.56	9.58

4.4.3 SEM

Even though XRD patterns of CNPI-1 (Fig. 4.2) and NCNPI-1 (Fig. 4.3) showed an amorphous structure, from SEM images (Fig. 4.6 and 4.7) and pore size distributions (Fig. 4.4 and 4.5) we can conclude that, the prepared microporous carbons were partially amorphous and partially ordered. Both the composites and heat treated samples retained the morphology of the H-Mordenite template. After the HF treatment, carbon samples started forming the amorphous kind of structure. Elemental analysis of H-Mordenite, composites and heat treated samples showed large amount of Al and Si content. HF treatment was required to remove the template.

In the case of CNPI-1 (2 % HF; 9 h), template was not completely removed. It was validated by both SEM image and EDX. But 5 % HF treatment was completely removing the template, leaving the required CNPI-1. Finally we can conclude that, (5% HF; 3 h) can remove Si and Al completely. EDX spectra of that corresponding carbon, CNPI-1 (5% HF; 3 h) showed almost negligible amount of Si and Al. The elemental analysis results of CNPI-1 are tabulated (Table 4.2). The corresponding EDX spectrums of CNPI-1 are shown in Appendix A: Fig. A.1.

In case of NCNPI-1, 5% HF treatment was done for different time durations to verify the effect of time for 5 % HF treatment. After the first hour only traces of Al and Si were there in NCNPI-1. Those traces of Al and Si have also been removed in the second hour. After the second hour, HF treatment gives almost the similar kind of NCNPI-1. These conclusions have been validated by the EDAX results. The elemental analysis results of NCNPI-1 are tabulated (Table 4.3). The corresponding EDX spectrums of NCNI-1 are shown in Appendix A: Fig. A.2.

Table 4.2: Elemental analysis results of CNPI-1.

Samples	**Composition (atom %)**			
	C	**O**	**Al**	**Si**
H-Mordenite (H-MOR)	40.0	51.8	0.5	7.8
FA / H-MOR composite	32.4	53.3	0.6	13.7
Heat treated sample	23.6	54.7	0.7	21.0
CNPI-1 (2 % HF; 9 h)	87.8	11.6	0.01	0.61
CNPI-1 (5 % HF; 3 h)	88.1	11.9	0.01	0.02
CNPI-1 (5 % HF; 6 h)	90.2	9.7	0.03	0.05

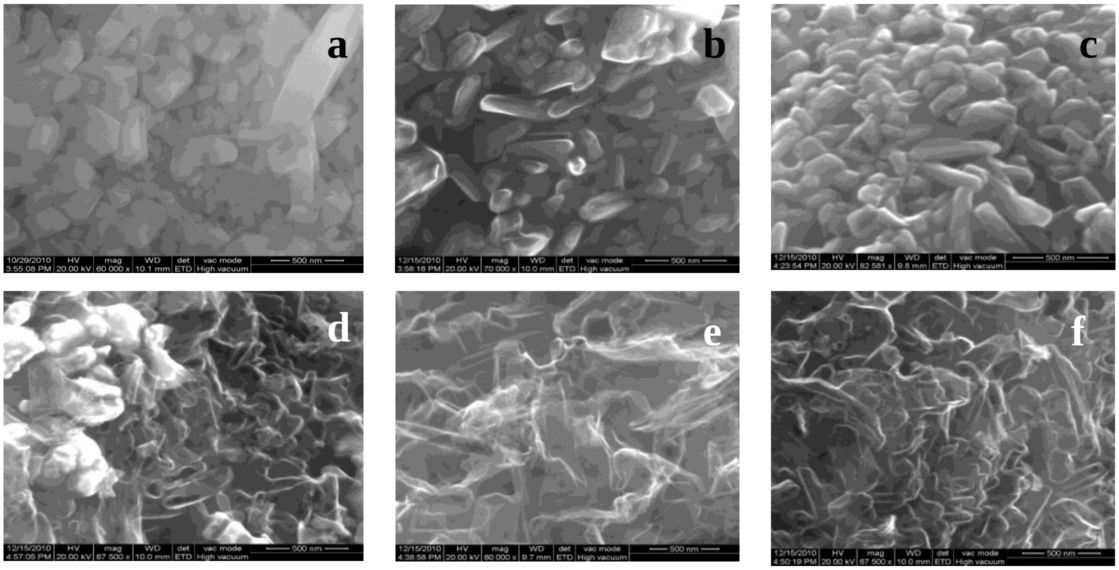

Figure 4.6: SEM images of: (a) H-Mordenite; (b) FA / H-MOR composite; (c) Heat treated sample; (d) CNPI-1(2 % HF; 9 h); (e) CNPI-1 (5 % HF; 3 h); (f) CNPI-1 (5 % HF; 6 h).

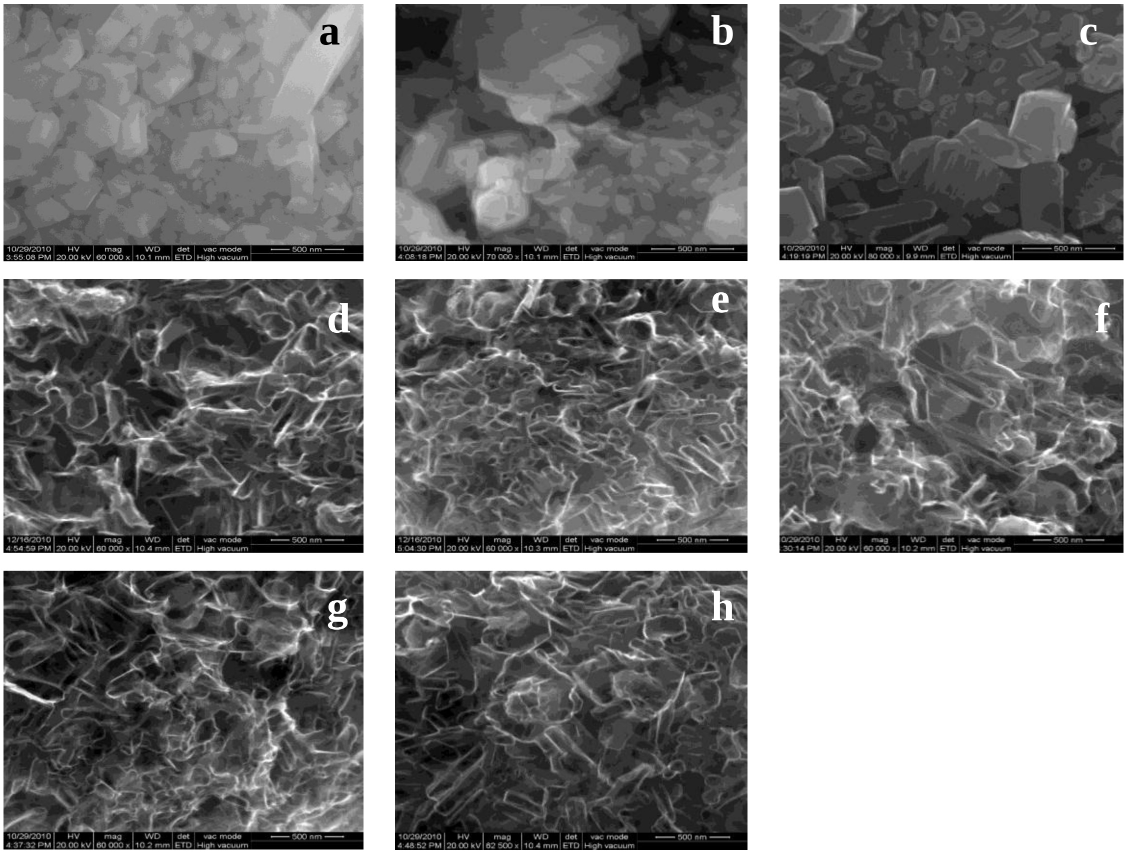

Figure 4.7: SEM images of (a) H-Mordenite; (b) Pyrrole / H-MOR composite; (c) Heat treated sample; (d) NCNPI-1 (5 % HF; 1 h); (e) NCNPI-1 (5 % HF; 2 h); (f) NCNPI-1 (5 % HF; 3 h); (g) NCNPI-1 (5 % HF; 6 h); (h) NCNPI-1 (5 % HF; 9 h).

Table 4.3: Elemental analysis results of NCNPI-1.

Samples	Composition (atom %)			
	C	O	Al	Si
H-Mordenite (H-MOR)	40.0	51.8	0.5	7.8
Pyrrole / H-MOR composite	43.4	44.3	0.6	11.8
Heat treated sample	47.3	43.1	0.3	9.4
NCNPI-1 (5 % HF; 1 h)	92.8	7.1	0.04	0.08
NCNPI-1 (5 % HF; 2 h)	90.1	9.9	0.02	0.03
NCNPI-1 (5 % HF; 3 h)	90.2	9.7	0.03	0.1
NCNPI-1 (5 % HF; 6 h)	91.1	8.8	0.05	0.03
NCNPI-1 (5 % HF; 9 h)	89.5	10.5	0.04	0.05

4.4.4 XPS

Fig. 4.8 shows survey spectra of CNPI-1 and NCNPI-1 by XPS. In the survey spectra, there are peaks of C 1s and O 1s in CNPI-1 is common with NCNPI-1. Anyhow, N 1s peak (399.6 eV) in survey XPS spectrum showed the presence of nitrogen only in the NCNPI-1 and not in CNPI-1. This obvious difference is due to the presence of nitrogen in the NCNPI-1 matrix.

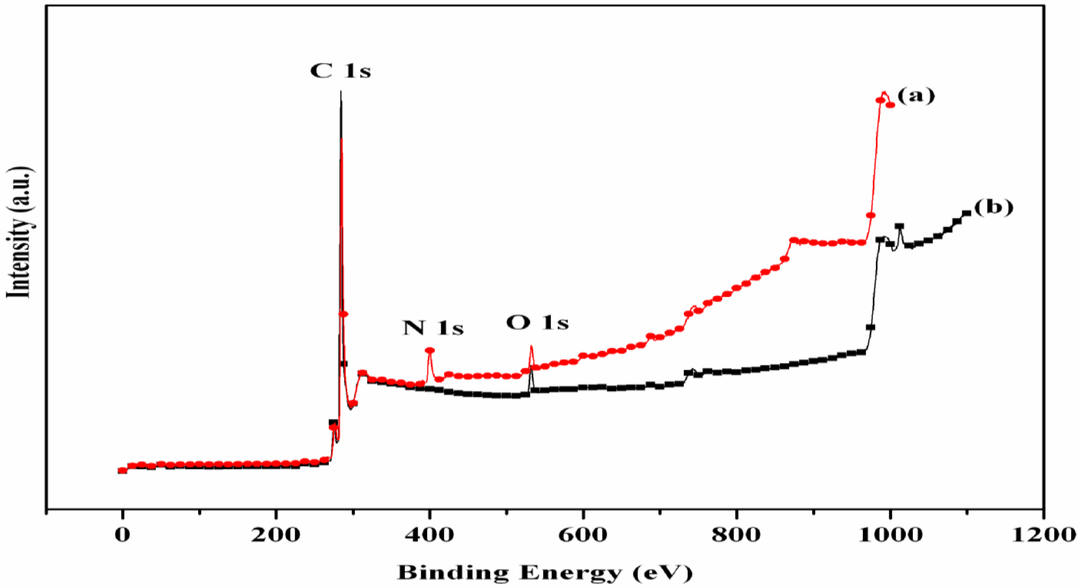

Figure 4.8: Survey XPS spectra of (a) NCNPI-1; (b) CNPI-1.

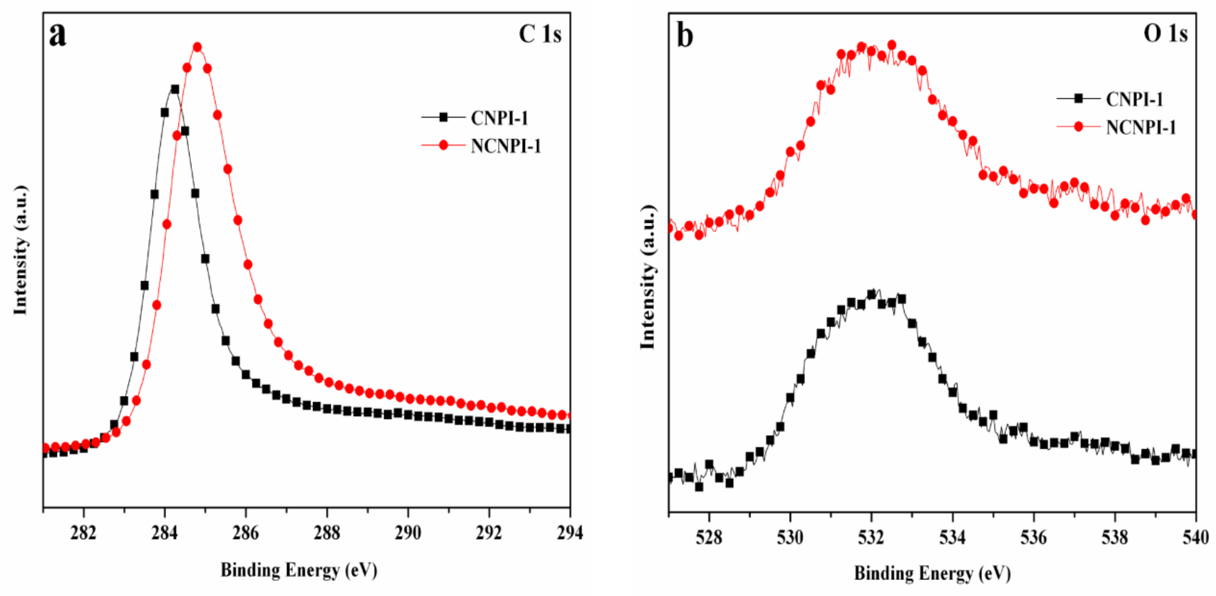

Figure 4.9: XPS spectra of CNPI-1 and NCNPI-1(a) C (1s); (b) O (1s).

C 1s and O 1s XPS spectras for CNPI-1 and NCNPI-1 are shown in Fig. 4.9a and 4.9b, respectively. Both C 1s and O 1s peaks of NCNPI-1 were slightly shifted to higher binding energy and suggested that this phenomenon occurred as a result of coordination between carbon and nitrogen and oxygen and nitrogen, respectively. Therefore the presence of C-N and N-O bonds in NCNPI-1 had been confirmed by XPS analysis.

Deconvoluted C 1s spectra for CNPI-1 and NCNPI-1 are shown in Fig. 4.10a and 4.10b. The C 1s of CNPI-1 was deconvoluted in to three lines peaked at 284.2, 285.2 and 286.5 eV. C 1s peak of CNPI-1 at 284.2, 285.2 and 286.5 eV was attributed to the sp^2 C–C bond in graphitic type carbon (77.3 %), carbon in the hydroxyl group (6.2 %) and carbonate species (16.6 %), respectively. One more peak also possible, which can be corresponding to carbonyl (C=O) group. The C 1s of NCNPI-1 was deconvoluted in to four lines peaked at 284.7, 285.8, 287.0 and 288.5 eV. C 1s peak of NCNPI-1 at 284.7, 285.8, 287.0 and 288.5 eV was attributed to the sp^2 C–C bond in graphitic type carbon (66.1 %), sp^2 C-N (22.5 %), sp^3 C-N (8.1 %) and carbonate species (3.3 %), respectively.

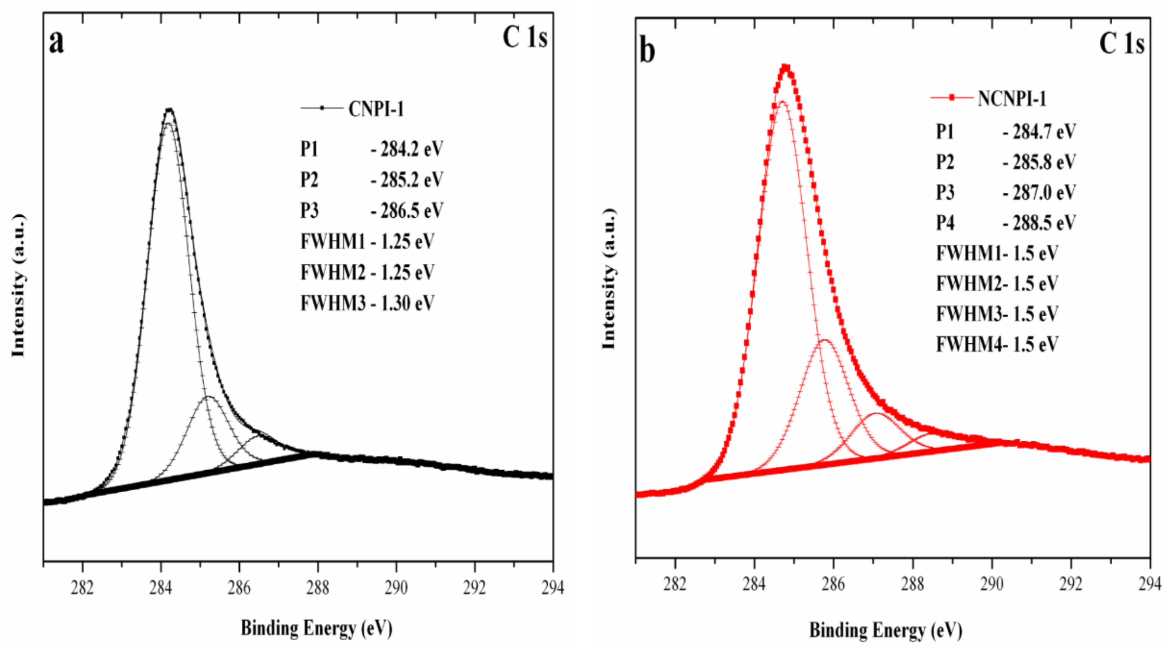

Figure 4.10: Deconvoluted XPS spectra of C 1s of (a) CNPI-1; (b) NCNPI-1.

Deconvoluted O 1s spectra for CNPI-1 and NCNPI-1 are shown in Fig. 4.11a and 4.11b. The O 1s of CNPI-1 was deconvoluted in to two lines peaked at 531.1 and 532.8 eV. O 1s peak of CNPI-1 at 531.1 and 532.8 eV was attributed to the C–O bond (47.6 %) and carbonyl (C=O) group (52.4 %). The O 1s of NCNPI-1 was deconvoluted in to three lines peaked at 530.7, 532.3 and 533.7 eV. O 1s peak of NCNPI-1 at 530.7, 532.3 and 533.7 eV was attributed to the C–O bond (46.8 %), carbonyl (C=O) group (18.7 %) and N-OH (34.5 %), respectively. O 1s spectras can be deconvoluted into one more peak corresponding to carbonate species. Both the O 1s spectras contained lesser concentration of carbonate species. Usually carbonate species will come in the higher binding energy region.

N 1s spectrum was deconvoluted with three types of nitrogen (Fig. 4.12). Peaks at 398.5, 400.5, and 401.4 eV were attributed to pyridinic, pyrrolic, and quaternary kind of nitrogen, respectively. Peaks of pyridinic (39.3 %) and pyrrolic (42.5 %) kind of nitrogens showed the highest proportion among the deconvoluted peaks. The peak at 401.4 eV was attributed to sp^2 N, i.e. substitutional N in the graphite sheets. Only 18 % of nitrogen was present in the carbon framework. This can be due to the partial infiltration of the pyrrole precursor in the microchannels of the H-Mordenite. In order to get the high activity of the NCNPI-1 supported catalyst, carbon framework should contain larger proportion of sp^2 N. Possible types of nitrogen in carbon materials are given in Fig. 4.13.

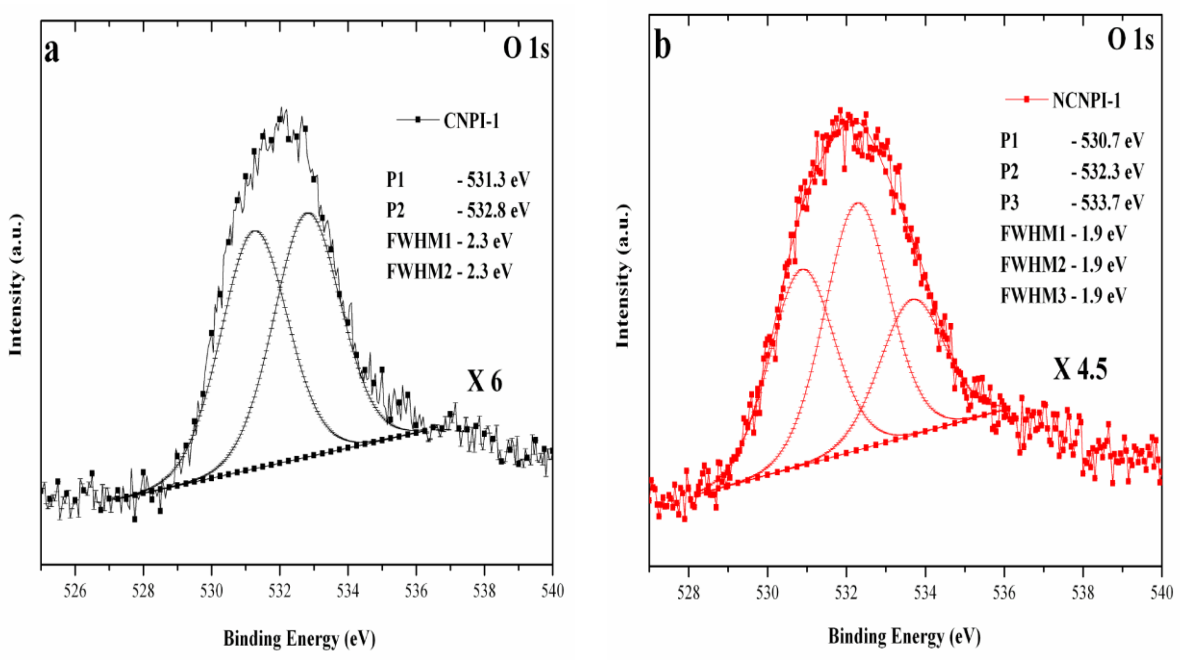

Figure 4.11: Deconvoluted XPS spectra of O 1s of (a) CNPI-1; (b) NCNPI-1.

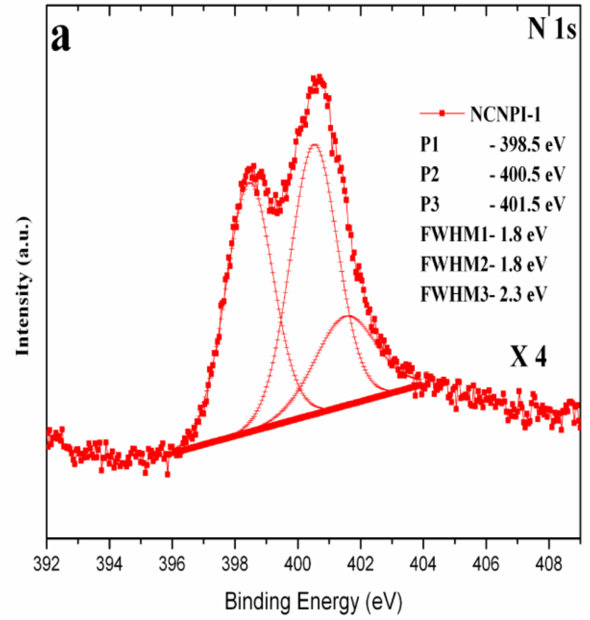

Figure 4.12: Deconvoluted XPS spectra of N 1s of NCNPI-1.

In XPS, the nitrogen 1s electron binding energy distribution is analyzed by deconvolution. Globally four or five types of nitrogen can be distinguished in carbonaceous materials by XPS: N-6 (398.7 ± 0.3 eV), N-5 (400.3 ± 0.3 eV), N-Q (401.4 ± 0.5 eV), N-X1 and N-X2 (402–405 eV). A schematic picture of nitrogen in carbon materials is given in Fig. 4.13. N-6 corresponds to pyridinic nitrogen. N-5 to pyrrolic nitrogen and to pyridinic nitrogen in association with oxygen functionality, the so-called pyridones exhibit a shift relative to pyridinic nitrogen due to some charge distribution. N-Q in carbon is represented by nitrogen which substitutes for carbon in the aromatic graphene structure. Nitrogen oxide and nitrate structures represent the two N-X types (-CN and $-NH_2$) that are generally found in the deconvolution of the spectra (Kapteijn *et al.*, 1999).

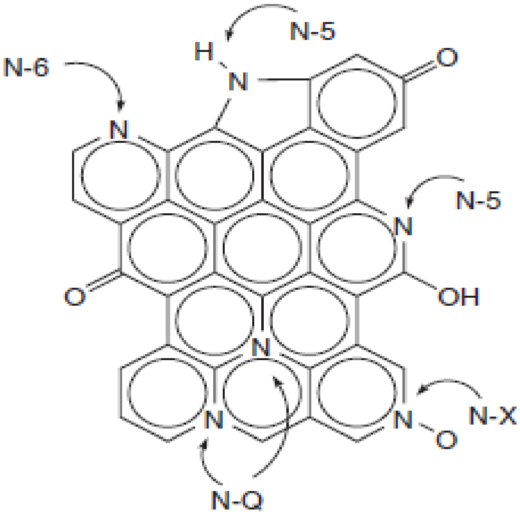

Figure 4.13: Model of a carbon layer with nitrogen atoms bonded differently (Kapteijn *et al.*, 1999).

CHAPTER 5

Pt/CNPI-1 AND Pt/NCNPI-1 ELECTRODES FOR DMFC APPLICATIONS

5.1 ELECTRODE MATERIALS FOR METHANOL OXIDATION

Pt is the only element found to give at least appreciable methanol oxidation current density and also could sustain the acidic condition of the fuel cell. It is due to its good adsorption capacity for methanol and its stability under oxidative conditions. The direct methanol fuel cell (DMFC) shown in Fig 1.2, consists of an anode at which methanol is oxidized to CO_2 through the following reaction (Hamnett, 1997),

$$CH_3OH + H_2O \rightarrow CO_2 + 6\,H^+ + 6\,e^- \qquad E_0 = 0.016\text{ V Vs SHE} \qquad (1)$$

And a cathode at which oxygen (usually as air) is reduced to water or steam.

$$1.5\,O_2 + 6\,H^+ + 6\,e^- \rightarrow 3\,H_2O \qquad E_0 = 1.229\text{ V Vs SHE} \qquad (2)$$

With the over all reaction of,

$$CH_3OH + 1.5\,O_2 \rightarrow CO_2 + 2\,H_2O \qquad E_{cell} = 1.213\text{ V Vs SHE} \qquad (3)$$

The basic mechanism for methanol oxidation was reviewed by Parsons and VanderNoot, 1988, and can be summarized in terms of two basic functionalities: (a) Electrosorption of methanol onto the substrate. (b) Addition of oxygen to adsorbed carbon containing intermediates to generate CO_2. Very few electrode materials are capable of adsorption of methanol; only platinum and platinum based catalysts have been found to show both sensible activity and stability in acidic condition of fuel cells. The mechanism of oxidation of methanol is supposed to follow the sequence of steps as below (Viswanathan and Scibioh., 2006);

$$Pt(s) + CH_3OH \rightarrow Pt - CH_2OH + H^+ + e^- \qquad (1)$$

$$Pt - CH_2OH + Pt(s) \rightarrow Pt_2–CHOH + H^+ + e^- \qquad (2)$$

$$Pt_2\text{–}CHOH + Pt(s) \rightarrow Pt_3\text{–}COH + H^+ + e^- \quad (3)$$

$$Pt_3\text{–}COH \rightarrow Pt\text{–}CO + 2\,Pt(s) + H^+ + e^- \quad (4)$$

$$Pt(s) + H_2O \rightarrow Pt\text{–}OH + H^+ + e^- \quad (5a)$$

$$Pt\text{–}OH + Pt\text{-}CO \rightarrow 2\,Pt + CO_2 + H^+ + e^- \text{ (or)} \quad (6)$$

The formation of OH by water activation on the Pt surface (5a), which is a necessary step for the oxidative removal of adsorbed CO, requires a high potential. In terms of methanol oxidation at anode, such a high potential will limit the fuel cell application of a pure platinum catalyst. Therefore a second metal that can provide oxygenated species at lower potentials for oxidative removal of adsorbed CO is visualized. Binary Pt-based alloys, such as PtRu, PtOs, PtSn, PtW and PtMo have been investigated in order to improve the electro-oxidation activities of methanol. Among them, the Pt–Ru alloy has been found to be the most active binary catalyst. The enhanced activity of the Pt–Ru catalyst when compared with Pt for methanol oxidation has been attributed to both a bi-functional mechanism and a ligand (electronic) effect. The bi-functional mechanism involves the adsorption of oxygen containing species on Ru atoms at lower potentials thereby promoting the oxidation of CO to CO_2, which can be summarized as follows:

$$Pt + CH_3OH \rightarrow Pt\text{-}CO_{ads} + 4H^+ + 4e^- \quad (7)$$

$$Ru + H_2O \rightarrow Ru(OH)_{ads} + H^+ + e^- \quad (8)$$

$$Pt\text{-}CO_{ads} + Ru(OH)_{ads} \rightarrow CO_2 + Pt + Ru + H^+ + e^- \quad (5b)$$

The catalytic activity of the Pt–Ru catalyst is strongly dependent on the composition, structure, morphology, particle size and degree of alloying. The current consensus is that the optimal Pt/Ru ratio is 1:1, and the particle sizes are better brought down to the nanoscale in order to improve the catalyst utilization. Alloying and nanoparticle supporting strategies could dramatically reduce the Pt content in the catalysts without performance compromise. The other strategy is support modification. Rapid development of nanotechnology, especially in the area of the synthesis of carbon nano-materials, expected to create more stable and active supported catalysts.

5.2 PREPARATION METHODS OF Pt/ONCs

Due to its simplicity, impregnation method is often used for the preparation of catalysts. Catalyst preparation by impregnation is carried out by contacting the support with a solution containing the precursors of the active phases. Two different modes of impregnation are practiced: wet impregnation and incipient-wetness impregnation. In wet impregnation the support material is brought into contact with a large excess of solution containing the metal precursors; after filtration and reduction, the final catalyst is obtained. In general, wet impregnation results in large particles since the majority of the metal precursor is present in the solution outside the pore system of the support. During drying the metal precursors often deposit on the outer surface of the support particles, resulting in large crystals. This method does not permit precise control of the amount of catalyst precursor loaded on the support. Thus, it is likely that some of the catalyst precursor will remain in the liquid phase after filtration.

To make effective use of the pore structure of the support, incipient-wetness impregnation can be performed in which the metal precursor is dissolved in just enough solvent to fill the pores of the support. In that case, closer contact is achieved between the metal precursor and the support, which in general results in smaller particles if reduction is executed carefully. Two major factors govern the final dispersion of the active phase: precursor–support interaction and pore structure. Micropores in the carbon support might be beneficial for metal dispersion. However, during the catalysis reaction these micropores might give rise to diffusion limitations (Serp and Figueiredo, 2009).

5.2.1 Colloidal deposition Method

*$NaBH_4$ (SBH) reduction***:** 50 mM $H_2PtCl_6.6H_2O$ and 4 mL 50 mM sodium citrate were mixed with 120 mL de-ionized water in a 250 ml beaker. 2 mL 0.5 M SBH was added drop wise under vigorous stirring at room temperature. SBH was used in excess for the complete reduction of Pt^{4+} to the elemental state. Stirring continued for 6 h, after that appropriate amount of carbon was added to the Pt sol. The mixture was then ultra-sonicated for 1 h followed by overnight stirring to allow for the equilibrium adsorption of Pt sol on carbon. The solid phase was then recovered by filtration, and washed copiously with water. The recovered solid was then dried at 80 °C overnight (Zeng *et al.,* 2007). ONCs and activated carbon (AC) were used as a support material

for the preparation of SBH reduced Pt catalysts. The obtained carbon supported Pt catalysts were designated as X wt.% Pt/CNPI-1 (SBH), X wt.% Pt/NCNPI-1 (SBH), and X wt.% Pt/AC (SBH) respectively. Then the prepared catalysts were characterized by XRD, XPS, TEM, CV and CA.

Ethylene Glycol (EG) reduction: 50 mM $H_2PtCl_6.6H_2O$ and 4 mL 50 mM sodium citrate were mixed with 60 mL of ethylene glycol (EG) in a 100 ml beaker. Ethylene glycol was used in excess for the complete reduction of Pt^{4+} to the elemental state. Stirring continued at 120 °C for 4 h in an oil bath. After the reduction, appropriate amount of carbon was added to the Pt sol. The mixture was then ultra-sonicated for 1 h followed by overnight stirring to allow for the equilibrium adsorption of Pt sol on carbon. The solid phase was then recovered by filtration, and washed copiously with water. The recovered solid was then dried at 80 °C overnight. CNPI-1, NCNPI-1 and AC were used as a support material for the preparation of ethylene glycol reduced Pt catalysts. The obtained carbon supported Pt catalysts were designated as X wt.% Pt/CNPI-1 (EG), X wt.% Pt/NCNPI-1 (EG), and X wt.% Pt/AC (EG) respectively. Then the prepared catalysts were characterized by XRD, XPS, TEM, CV and CA.

5.2.2 Wet impregnation method

50 mM $H_2PtCl_6.6H_2O$ and 4 mL 50 mM sodium citrate were mixed with 120 mL de-ionized water which contained appropriate amount of carbon. After 30 min of sonication, 2 mL 0.5 M of SBH was introduced drop wise to the carbon suspension with vigorous stirring at room temperature. The mixture was then stirred for overnight. The solid phase was recovered by filtration, and washed copiously with water. The recovered solid was then dried at 80 °C overnight (Zeng *et al.*, 2007). Then the prepared catalyst was characterized by XRD.

5.2.3 Incipient-wetness impregnation method

50 mM $H_2PtCl_6.6H_2O$ was mixed with 10 mL de-ionized water containing appropriate amount of carbon. The suspension was evaporated slowly under stirring. Finally solid phase was recovered and reduced under H_2 atmosphere at 450 °C for 8 h. Then the prepared catalyst was characterized by XRD. High temperature and long duration were used as reduction conditions for the complete reduction of Pt^{4+} to the elemental state.

5.3 CHARACTERIZATION

5.3.1 XRD

Fig. 5.1 shows XRD patterns of 10 wt.% Pt/AC prepared by different methods. Fig. 5.2 shows XRD patterns of 10 wt.% Pt/ONCs prepared by colloidal deposition method using SBH as a reducing agent. 10 wt.% Pt supported on activated carbon and ONCs had been done for the optimization process. The broad diffraction peak observed on carbon supported Pt catalysts at around 25° was corresponding to the carbon. The diffraction peaks at about 39°, 46°, 67° and 81° were from the Pt (1 1 1), (2 0 0), (2 2 0) and (3 1 1) planes, respectively (JCPDS file No. 87-0647). The high intensity and well resolved Pt (1 1 1) diffraction peak was used for the crystallite size calculation. The crystallite sizes of Pt, calculated from the Pt (1 1 1) diffraction peak by means of Scherrer equation, for 10 wt.% Pt/AC prepared by incipient-wetness, wet impregnation and sol methods were 11.8, 4.5 and 4.6 nm, respectively (Table 5.1).

The carbon supported Pt catalyst prepared by incipient-wetness method showed the higher crystallite size because of high temperature reduction process. Therefore, we can conclude that the incipient-wetness was not a suitable method for the preparation of carbon supported Pt catalyst. Even though, Pt catalysts prepared by both the wet impregnation and colloidal deposition method resulted the similar crystallite size, we preferred colloidal deposition as a best method. Because in the latter case, size of the sol controls the crystallite size, while in the former case, precipitation capacity of the Pt nanoparticles plays the major role in controlling the crystallite size. The crystallite sizes of Pt, for 10 wt.% Pt/CNPI-1 (SBH) and 10 wt.% Pt/NCNPI-1 (SBH) prepared by colloidal deposition method were 4.3 and 4.5 nm, respectively (Table 5.2). The lattice constant value of ~ 0.39 nm correlates well with the FCC lattice of Pt metal supported on carbon materials (JCPDS file No. 87-0647). The lattice constant value of Pt metal is 0.3923 nm (Liu *et al.,* 2004).

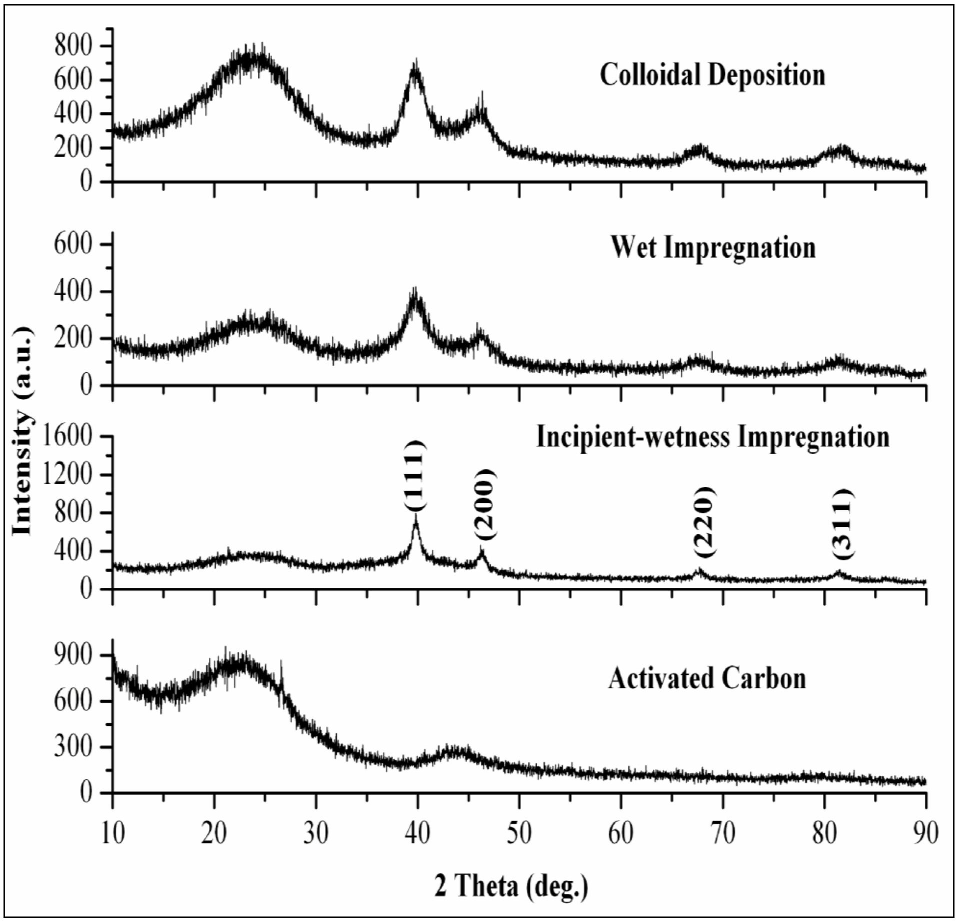

Figure 5.1: XRD patterns of 10 wt.% Pt/AC prepared by different methods.

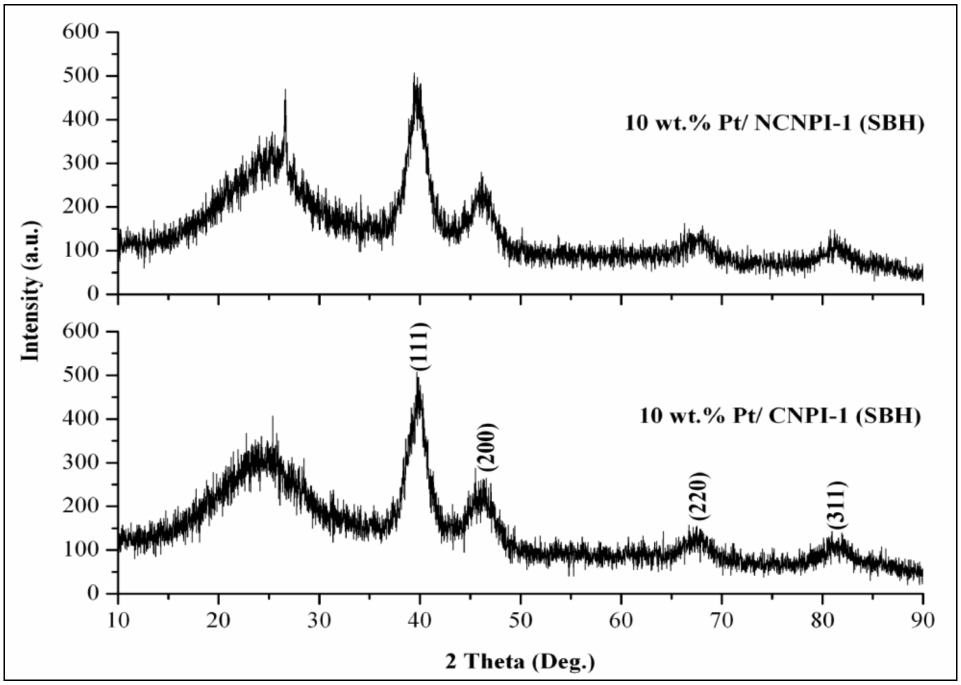

Figure 5.2: XRD patterns of 10 wt.%Pt/ ONCs prepared by colloidal deposition method using SBH as a reducing agent.

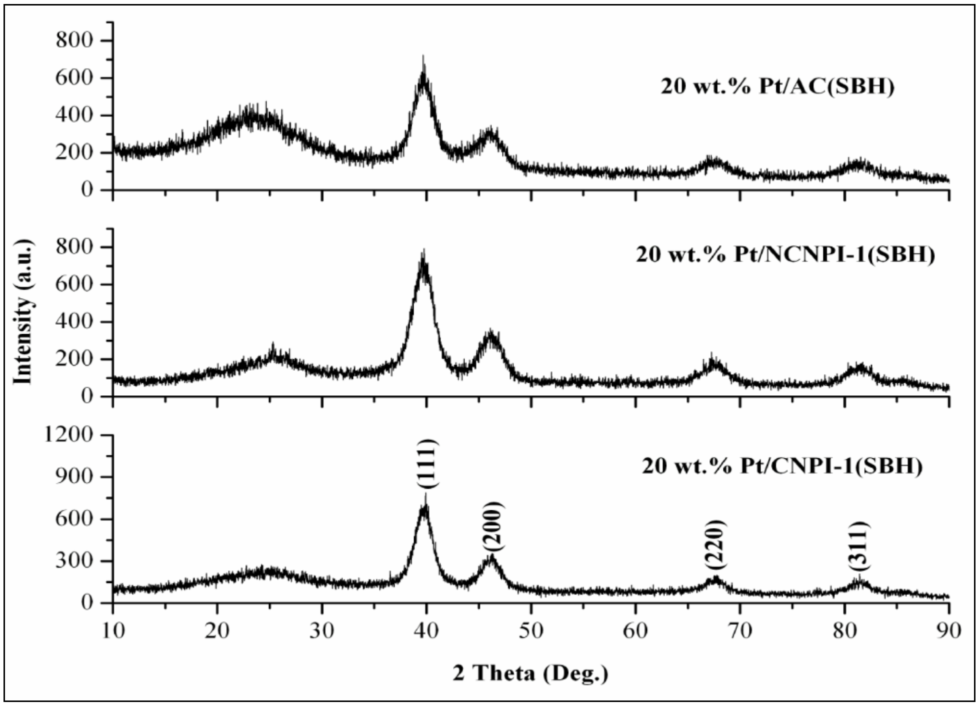

Figure 5.3: XRD patterns of 20 wt.% Pt supported on ONCs and AC prepared by colloidal deposition method using SBH as a reducing agent.

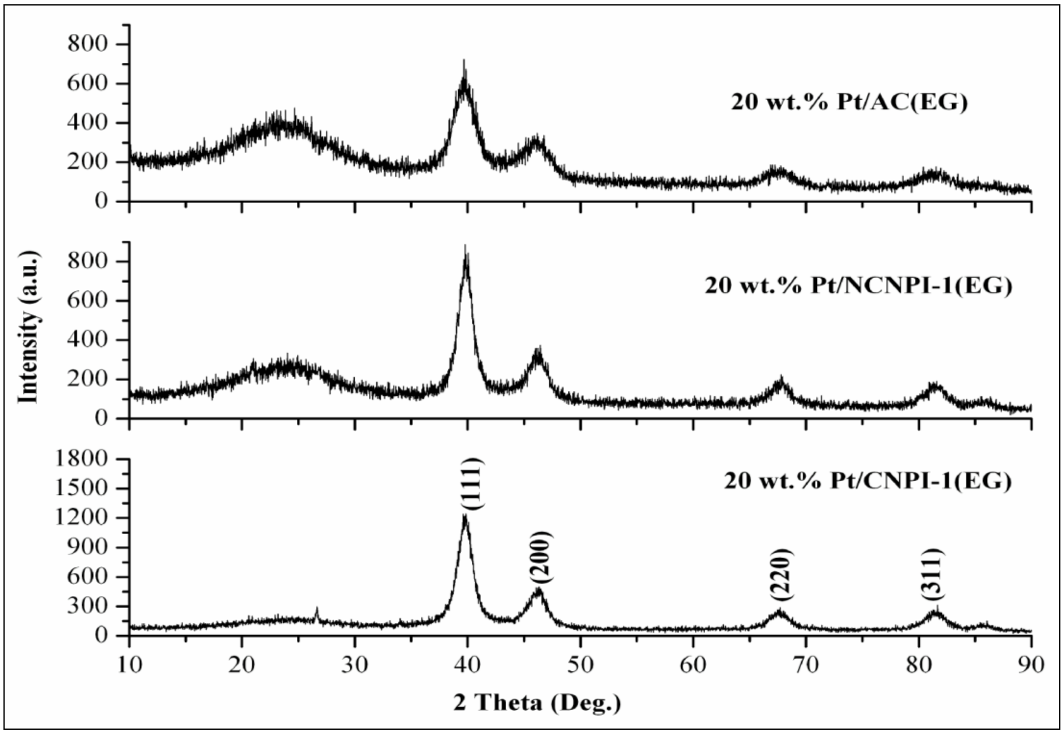

Figure 5.4: XRD patterns of 20 wt.% Pt supported on ONCs and AC prepared by colloidal deposition method using EG as a reducing agent.

Fig. 5.3 and 5.4 shows XRD patterns of 20 wt.% Pt supported on carbons (ONCs and AC) prepared by colloidal deposition method using different reducing agents (SBH and EG). The broad diffraction peak observed on carbon supported Pt catalysts at around 25° was corresponding to the carbon. The diffraction peaks at about 39°, 46°, 67° and 81° were from the Pt (1 1 1), (2 0 0), (2 2 0) and (3 1 1) planes, respectively (JCPDS file No. 87-0647). The crystallite sizes of carbon supported Pt catalysts were calculated from the high intensity and well resolved Pt (1 1 1) diffraction peak by means of Scherrer equation. The crystallite size values of those catalysts were tabulated (Table 5.2).

Table 5.1: Effect of preparation methods on the crystallite size of the AC supported Pt catalysts.

10 wt.% Pt/AC Preparation methods	Reducing Medium	Pt Lattice Constant (nm)	Pt Crystallite Size (nm)
Incipient-Wetness Impregnation	H_2	0.3911	11.8
Wet Impregnation	SBH	0.3916	4.5
Colloidal deposition	SBH	0.3912	4.6

Table 5.2: Effect of reducing agents and platinum loading on the crystallite size of the carbon (ONCs and AC) supported Pt catalysts.

Catalysts	Pt Lattice Constant (nm)	Pt Crystallite Size (nm)
20 wt.% Pt/CNPI-1 (SBH)	0.3918	4.8
20 wt.% Pt/NCNPI-1 (SBH)	0.3923	4.0
20 wt.% Pt/AC (SBH)	0.3919	4.4
20 wt.% Pt/CNPI-1 (EG)	0.3919	6.0
20 wt.% Pt/NCNPI-1 (EG)	0.3907	6.2
20 wt.% Pt/AC (EG)	0.3918	6.4
10 wt.% Pt/CNPI-1 (SBH)	0.391	4.3
10 wt.% Pt/NCNPI-1 (SBH)	0.3917	4.5
40 wt.% Pt/E-TEK	0.3909	3.9

SBH reduced Pt catalysts showed lower crystallite size (~ 4 nm) compare to EG reduced Pt catalysts (~ 6 nm) (Table 5.2). In the case of EG reduced Pt catalysts, nature of the carbon support was not showing any significant difference in the crystallite size.

5.3.2 TEM

Fig. 5.5 shows the TEM, Electron diffraction images and Fig. 5.6 shows the histograms (particle size distribution) of ONCs supported Pt catalysts. Fig. 5.5a and 5.6a show that the Pt nanoparticles in the 20 wt.% Pt/CNPI-1 (SBH) had an average particle size of 4.4 nm ($\sigma = 0.9$ nm), and were highly dispersed.

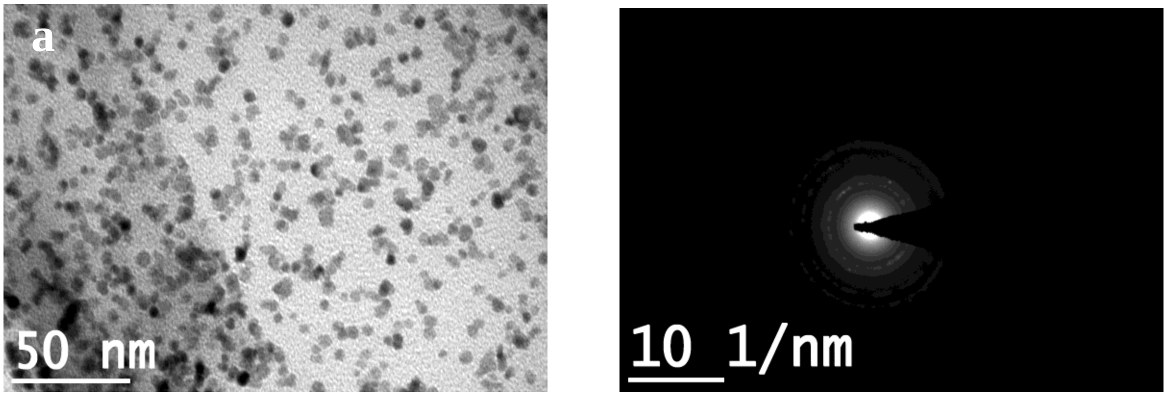

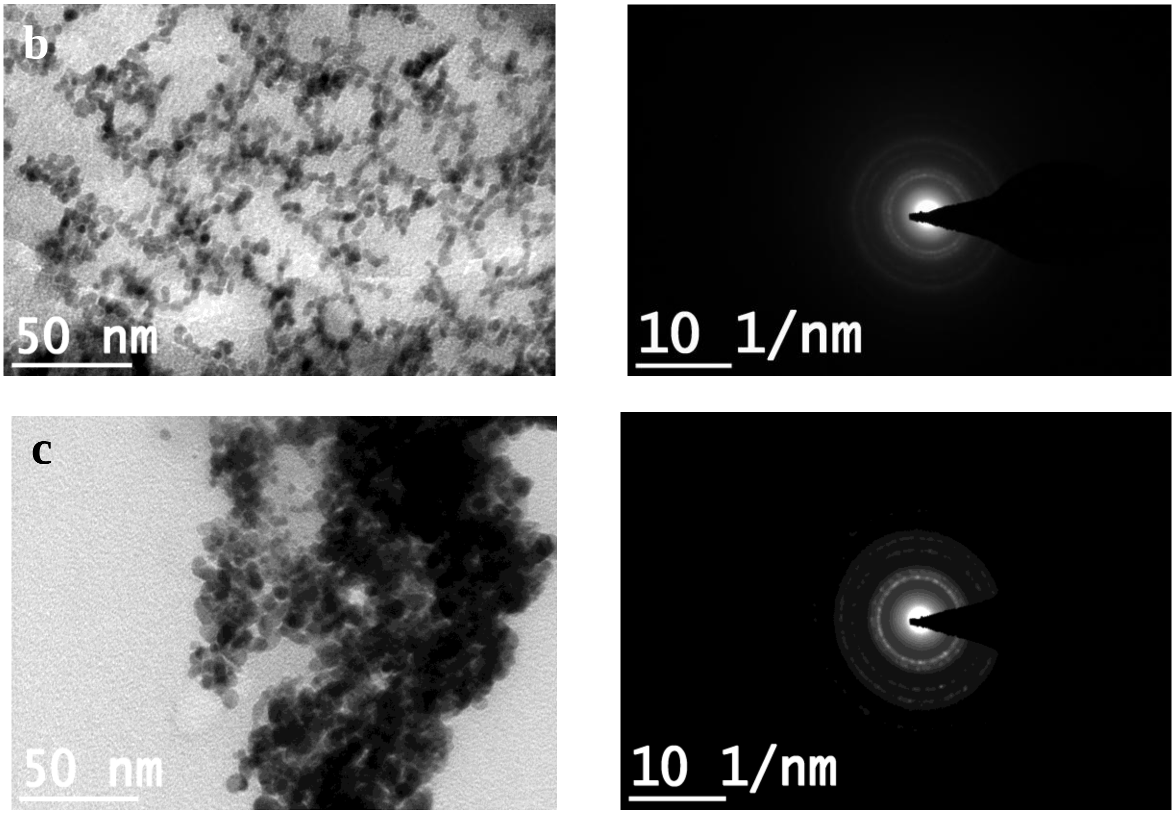

Figure 5.5: TEM and ED of: (a) 20 wt.% Pt/CNPI-1 (SBH); (b) 10 wt.% Pt/NCNPI-1 (SBH); (c) 20 wt.% Pt/CNPI-1 (EG).

Fig. 5.5b and 5.6b show that the Pt nanoparticles in the 10 wt.% Pt/NCNPI-1 (SBH) had an average particle size of 3.9 nm (σ = 0.6 nm), and were lightly agglomerated despite electrostatic stabilization by the adsorbed citrate ions due to presence of nitrogen in the NCNPI-1 matrix. Fig. 5.5c and 5.6c show the that the Pt nanoparticles in the 20 wt.% Pt/CNPI-1 (EG) had an average particle size of 6.7 nm (σ = 1.7 nm), and were highly agglomerated compare to SBH reduced catalysts. EG reduced catalyst was having higher particle size compared to SBH reduced catalysts. This is also validating the XRD results.

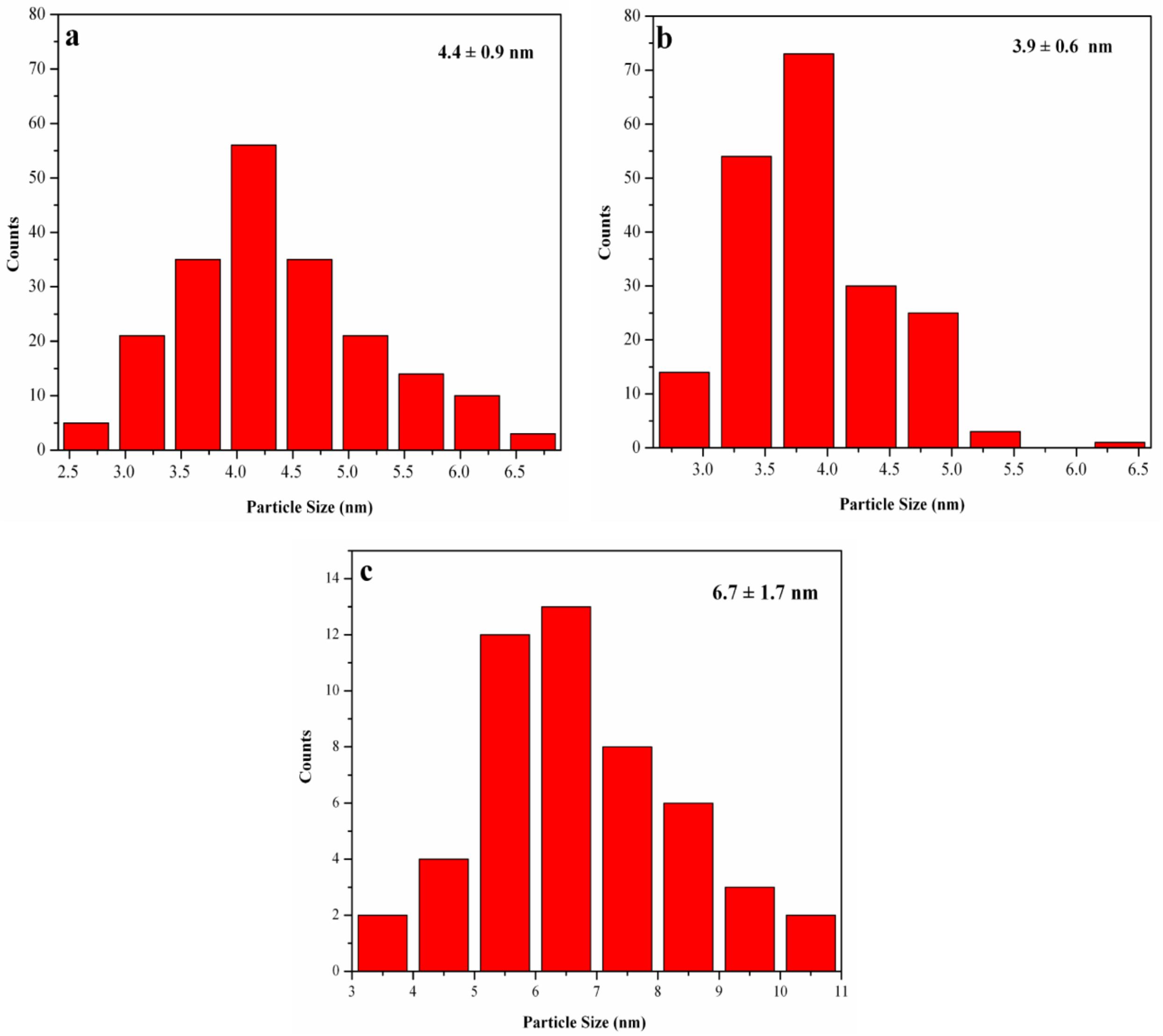

Figure 5.6: Histogram of the ONCs supported Pt catalysts (a) 20 wt.% Pt/CNPI-1 (SBH); (b) 10 wt.% Pt/NCNPI-1 (SBH); (c) 20 wt.% Pt/CNPI-1 (EG).

5.3.3 XPS

Fig. 5.7 shows survey spectra of (a) 20 wt.% Pt/AC (EG); (b) 20 wt.% Pt/CNPI-1 (SBH) in XPS. In the survey spectra, there are peaks of Pt 4f, C 1s, Pt 4d, Pt 4p, and O 1s are common in all the carbon supported Pt catalysts. Fig. 5.8 shows survey spectra of (a) 10 wt.% Pt/NCNPI-1 (SBH); (b) 10 wt.% Pt/CNPI-1 (SBH) in XPS. In the survey spectra, there are peaks of Pt 4f, C 1s, Pt 4d and O 1s are common in all the carbon supported Pt catalysts. Anyhow, N 1s peak (399.8 eV) in survey XPS spectrum showed the presence of nitrogen only in the 10 wt. %

Pt/NCNPI-1 (SBH) and not in10 wt.% Pt/CNPI-1 (SBH). This obvious difference was due to the presence of nitrogen in the NCNPI-1 matrix.

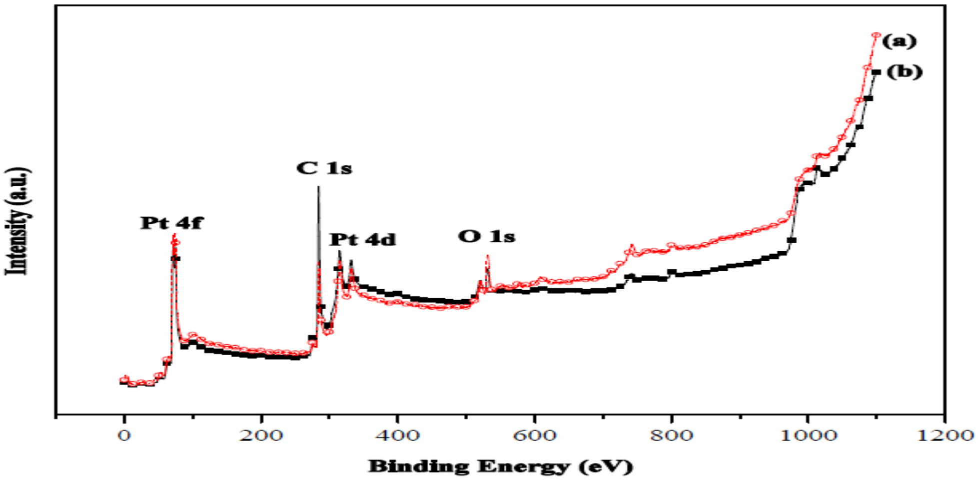

Figure 5.7: Survey XPS spectra of (a) 20 wt.% Pt/AC (EG); (b) 20 wt.% Pt/CNPI-1 (SBH).

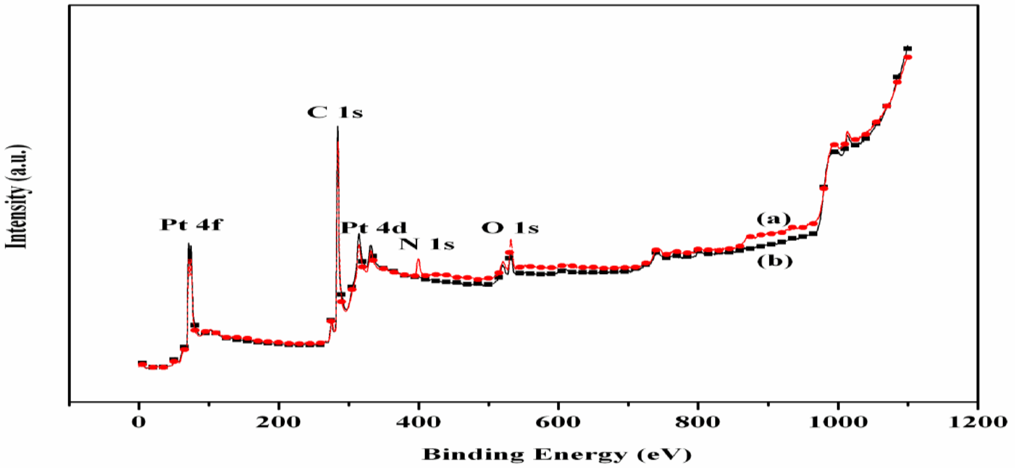

Figure 5.8: Survey XPS spectra of (a) 10 wt.% Pt/NCNPI-1 (SBH); (b) 10 wt.% Pt/CNPI-1 (SBH).

Fig. 5.9a and 5.9b show the XPS of Pt 4f spectrum for the 20 wt.% Pt/C and 10 wt.% Pt/ONCs prepared by colloidal deposition method, respectively. The Pt 4f spectrum shows a doublet containing a low- energy band (Pt 4f $_{7/2}$) and a high energy band (Pt 4f $_{5/2}$) at 71.2 and 74.6 eV, respectively. These binding energy values are in good agreement with the literature data for Pt (Hufner and Wertheim, 1975). These peaks indicated that Pt is present in metallic state, Pt (0).

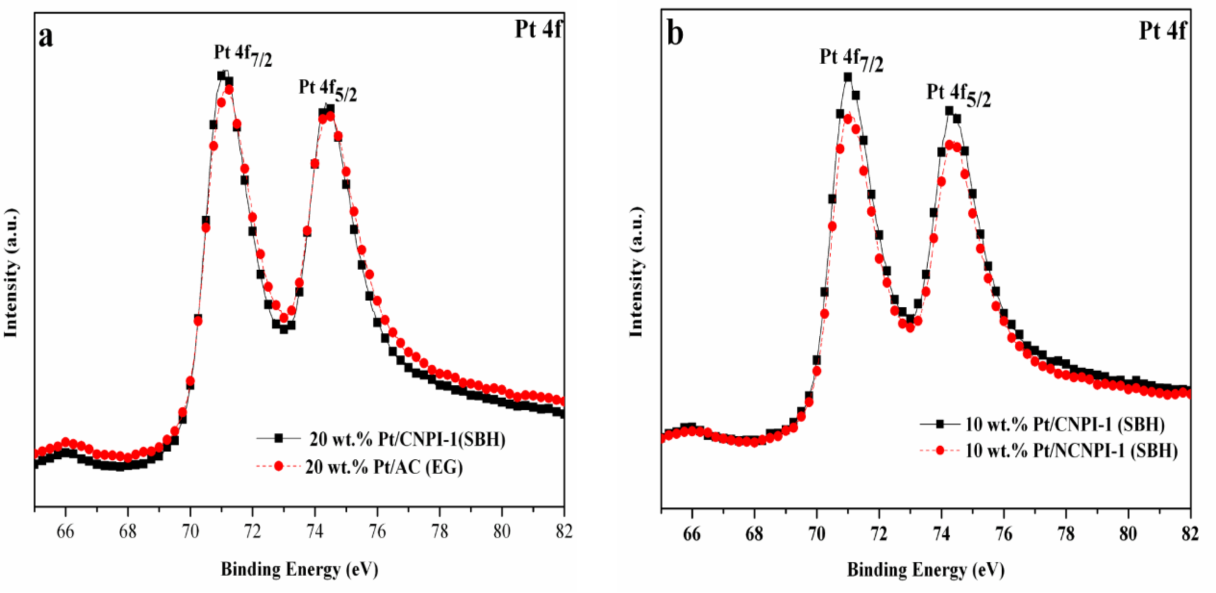

Figure 5.9: XPS spectra of Pt 4f of (a) 20 wt.% Pt/C; (b) 10 wt.% Pt/ONCs.

Both C 1s spectra and O 1s spectra of 10 wt.% Pt/CNPI-1 (SBH) had a more positive binding energy value compared to CNPI-1 (Fig. 5.10a and 5.10b). The peak position of C 1s for CNPI-1 and 10 wt.% Pt/CNPI-1 (SBH) were 284.2 and 284.3 eV, respectively. The peak position of O 1s for CNPI-1 and 10 wt.% Pt/CNPI-1 (SBH) were 532.0 and 532.5 eV, respectively.

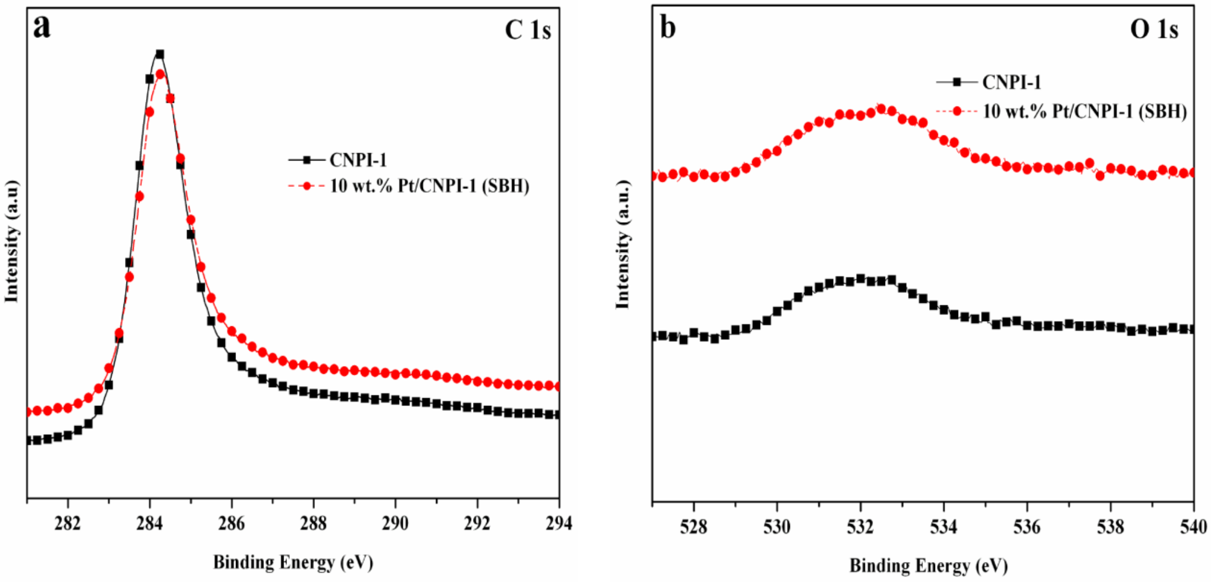

Figure 5.10: XPS spectra of CNPI-1 and 10 wt.% Pt/CNPI-1 (SBH) (a) C (1s); (b) O (1s).

C 1s spectra of 10 wt.% Pt/NCNPI-1 (SBH) have a more negative binding energy value compared to NCNPI-1 (Fig. 5.11a). The main peak position of C 1s is 284.8 eV, 284.6 eV at the NCNPI-1 and 10 wt.%Pt/NCNPI-1 (SBH), respectively. The shift in the C 1s peak is mainly due to the Pt incorporation in the carbon framework. O 1s spectra of 10 wt.% Pt/NCNPI-1 (SBH) have a more positive binding energy value compared to NCNPI-1 in Fig. 5.11b. The main peak position of O 1s is 532.1 eV, 532.4 eV at the NCNPI-1 and 10 wt.% Pt/NCNPI-1 (SBH), respectively. N 1s spectra of 10 wt.% Pt/NCNPI-1 (SBH) have a more negative binding energy value compared to NCNPI-1 (Fig. 5.11c). N 1s spectrum was deconvoluted with three types of nitrogen. Peaks at 398.5, 400.5, and 401.4 eV were attributed to pyridinic, pyrrolic, and quaternary nitrogen, respectively. Peak of pyrrolic kind of nitrogen showed the highest proportion among the deconvoluted peaks (Fig. 4.12). Lesser proportion of nitrogen was present in the carbon framework compared to pore walls.

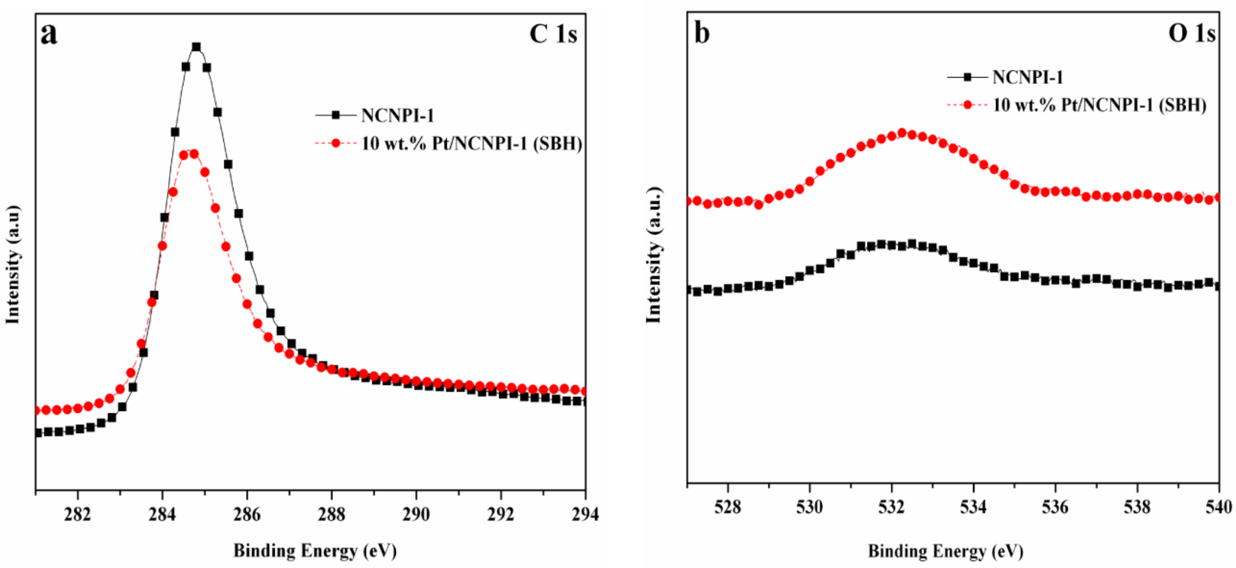

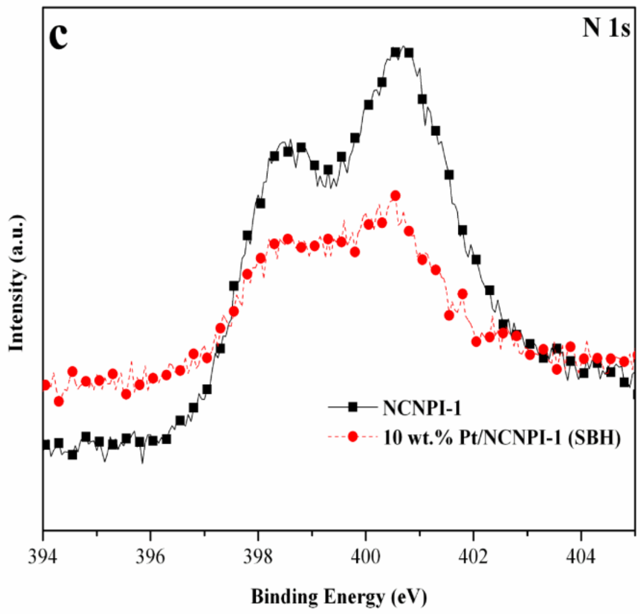

Figure 5.11: XPS spectra of NCNPI-1 and 10 wt.% Pt/NCNPI-1 (SBH) (a) C (1s); (b) O (1s); (c) N (1s).

5.3.4 Electro oxidation of methanol - Cyclic Voltammetry

The cyclic voltammograms (CV) for the carbon (Activated Carbon, ONCs and E-TEK) supported Pt catalysts, in 1 M H_2SO_4 are shown in Fig. 5.12-5.14. The redox couple (+ 0.4 V in the forward scan and + 0.26 V in the backward scan) in the CV of the supported platinum catalysts could arise from surface species on the carbon support. The peak in the reverse scan at + 0.55 V belonged most likely to Pt oxide reduction. The peak potential was the same for all the catalysts indicating that the Pt particles on the carbon support had similar physiochemical attributes (size and composition), validating the XRD measurements. The calculation of electrochemically active surface areas, which is often carried out by integrating the well-resolved peaks in the hydrogen adsorption region, was evaluated. ESA was calculated for different catalysts and tabulated in Table 5.4. The model ESA calculation is shown in section 3.2.6. The area used for ESA calculation for different catalysts are shown in appendix D.

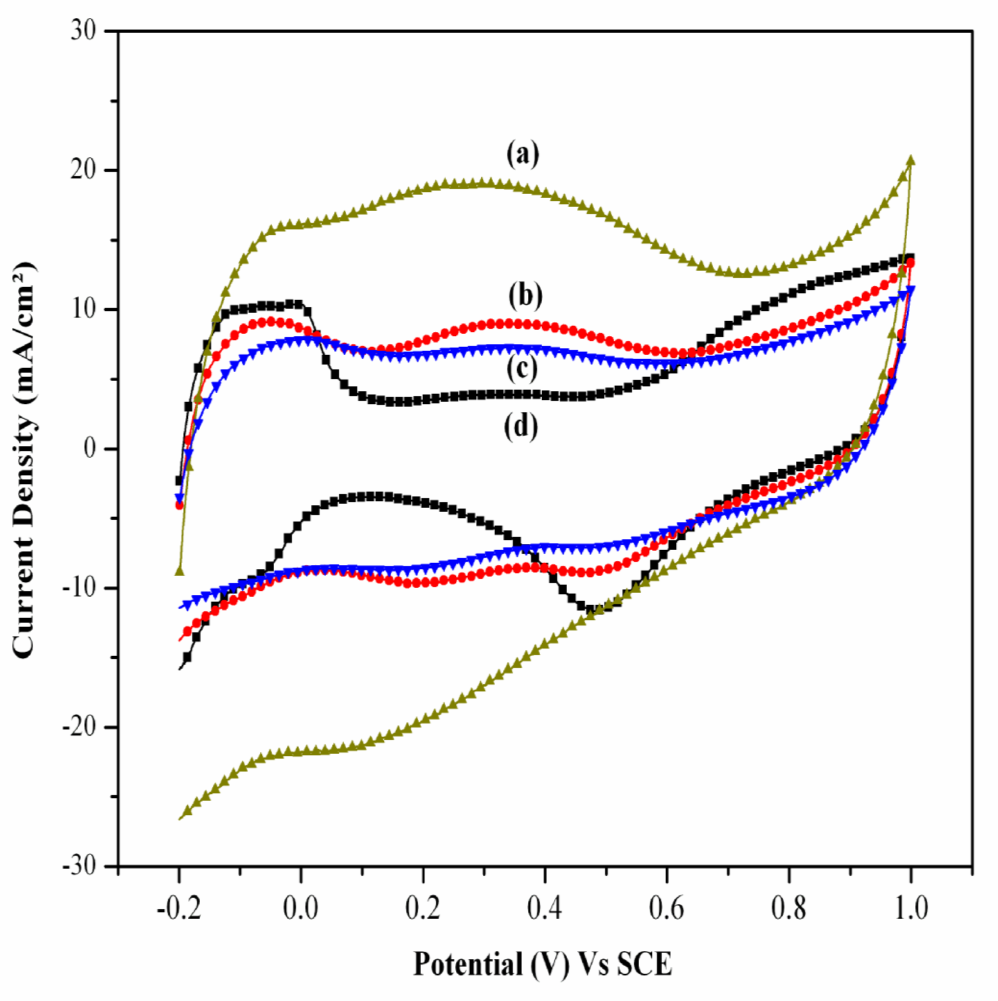

Figure 5.12: Cyclic voltammograms of (a) 20 wt.% Pt/NCNPI-1 (SBH); (b) 20 wt.% Pt/CNPI-1 (SBH); (c) 20 wt.% Pt/AC (SBH); (d) 40 wt.% Pt/E-TEK measured in 1 M H_2SO_4 electrolyte at room temperature (scan rate: 50 mV/s).

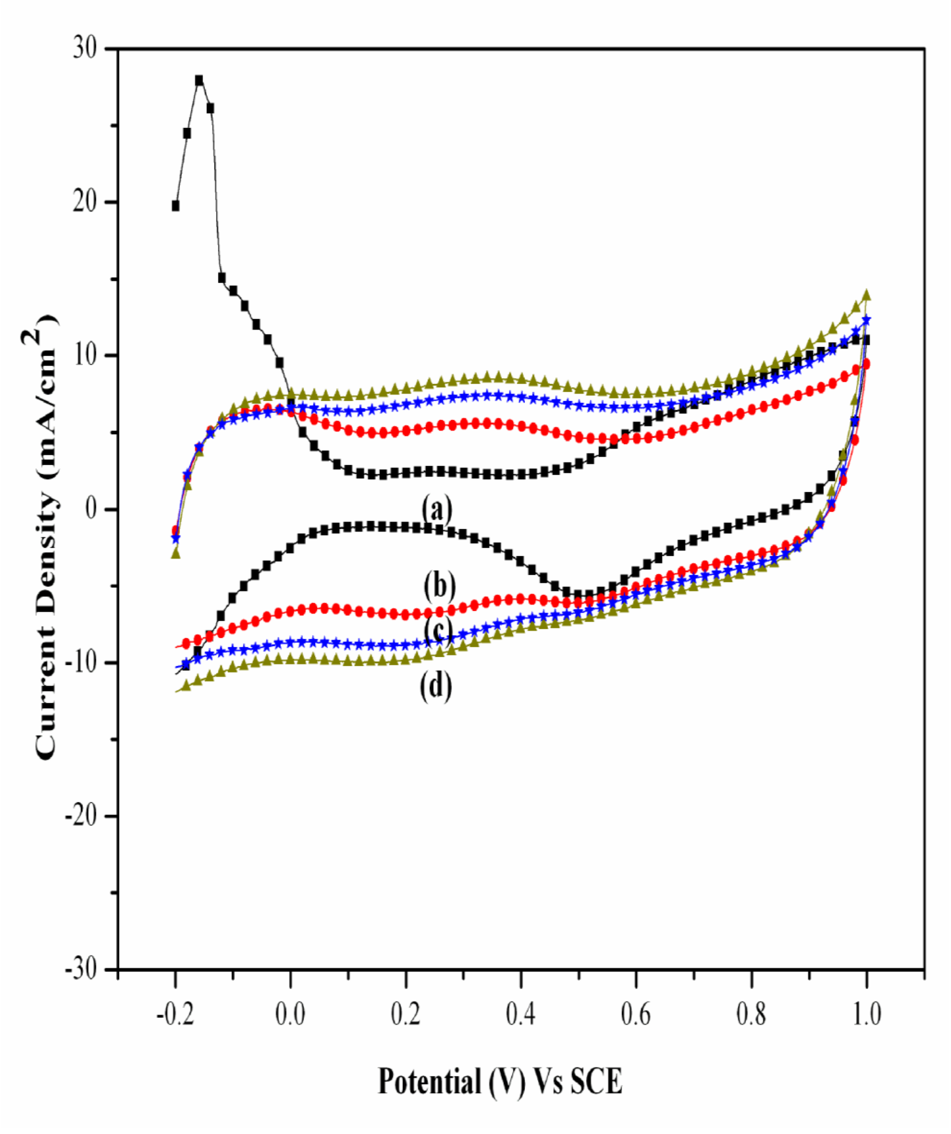

Figure 5.13: Cyclic voltammograms of (a) 20 wt.% Pt/E-TEK; (b) 20 wt.% Pt/CNPI-1 (EG); (c) 20 wt.% Pt/AC (EG); (d) 20 wt.% Pt/NCNPI-1 (EG) measured in 1 M H_2SO_4 electrolyte at room temperature (scan rate: 50 mV/s).

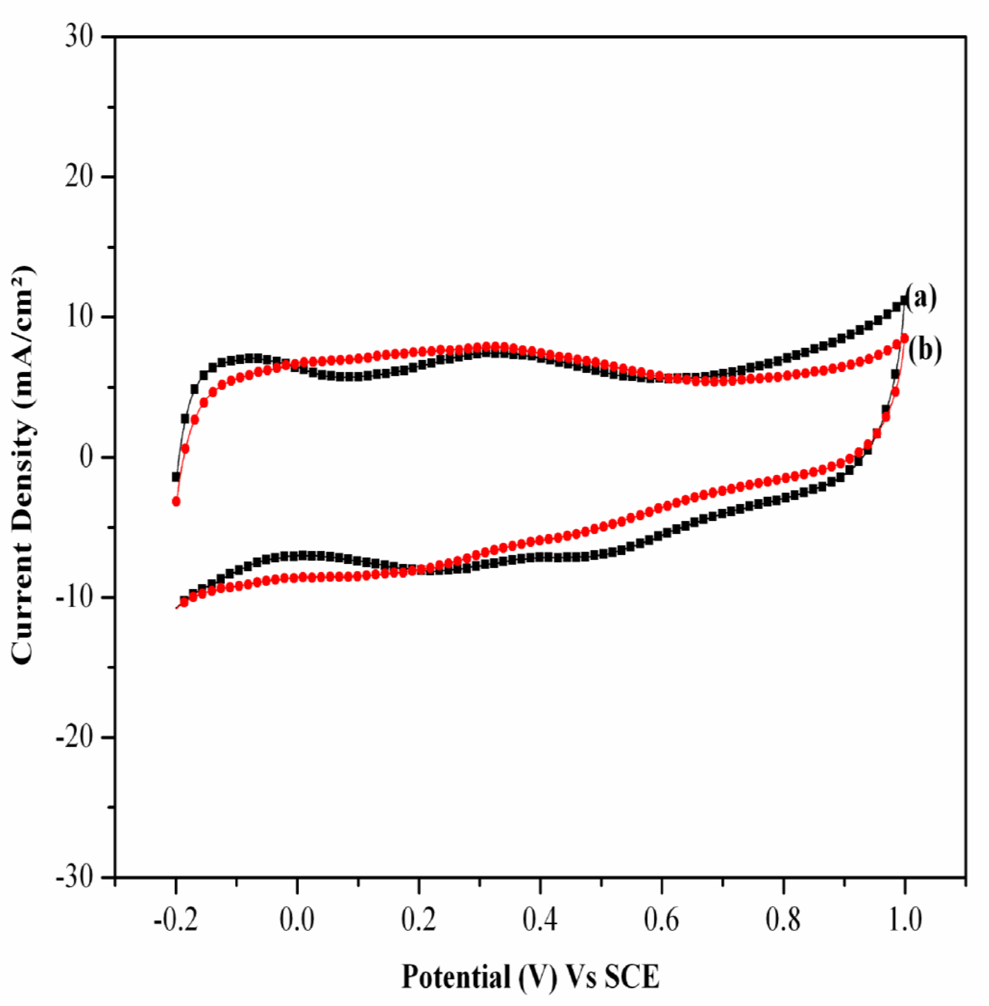

Figure 5.14: Cyclic voltammograms of (a) 10 wt.% Pt/CNPI-1 (SBH); (b) 10 wt.% Pt/NCNPI-1 (SBH) measured in 1 M H_2SO_4 electrolyte at room temperature (scan rate: 50 mV/s).

5.3.5 Evaluation of Mass Specific Activity (MSA) of the prepared catalysts

The mass normalized cyclic voltammograms recorded with electrodes fabricated using 10 and 20 wt. % Pt supported on carbon material ONCs and AC in 1M H_2SO_4 and 1M CH_3OH are shown in Fig. 5.15-5.17. The feature common to all the cyclic voltammograms is that one anodic peak is observed in the forward scan and another in the reverse scan. The anodic peak in the forward scan is attributed to oxidation of methanol. The anodic peak in the reverse scan is attributed to the removal of the incompletely oxidized carbonaceous species (mostly in the form of linearly bonded Pt=C=O) formed in the forward scan. The critical parameter that determines the usefulness of an electrode is the onset potential. A less positive value of the onset potential is preferred. A lower onset (less positive potential) potential value implies the requirement of lower energy for the methanol oxidation reaction to take place (Sobkowski *et al.,* 1992). The onset potential value is related to the breaking of the C-H bond of methanol which is the primary step involved in the mechanism of oxidation of methanol (Wu *et al.*, 2007).

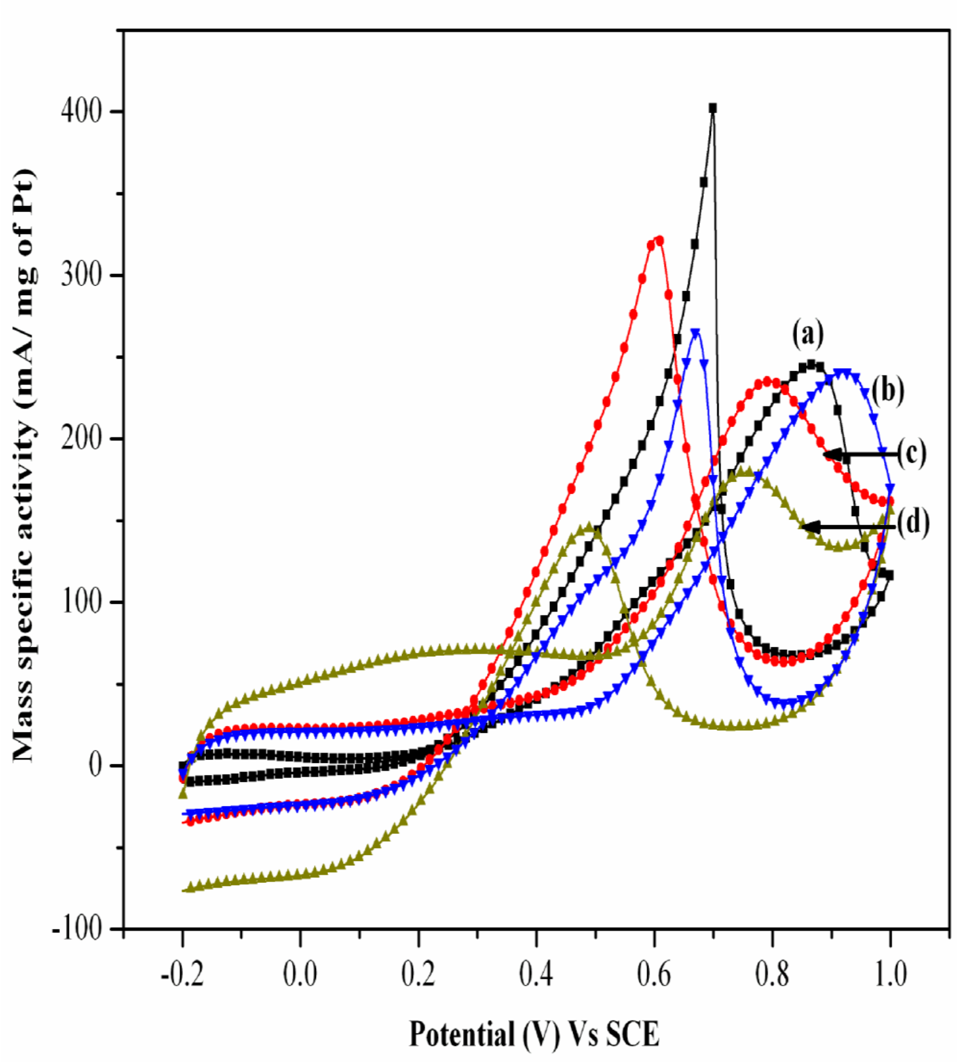

Figure 5.15: MSA of (a) 40 wt.% Pt/E-TEK; (b) 20 wt.% Pt/AC (SBH); (c) 20 wt.% Pt/CNPI-1(SBH); (d) 20 wt.% Pt/NCNPI-1 (SBH) for methanol electro oxidation reaction in 1 M CH_3OH + 1 M H_2SO_4 at room temperature (scan rate: 50 mV/s).

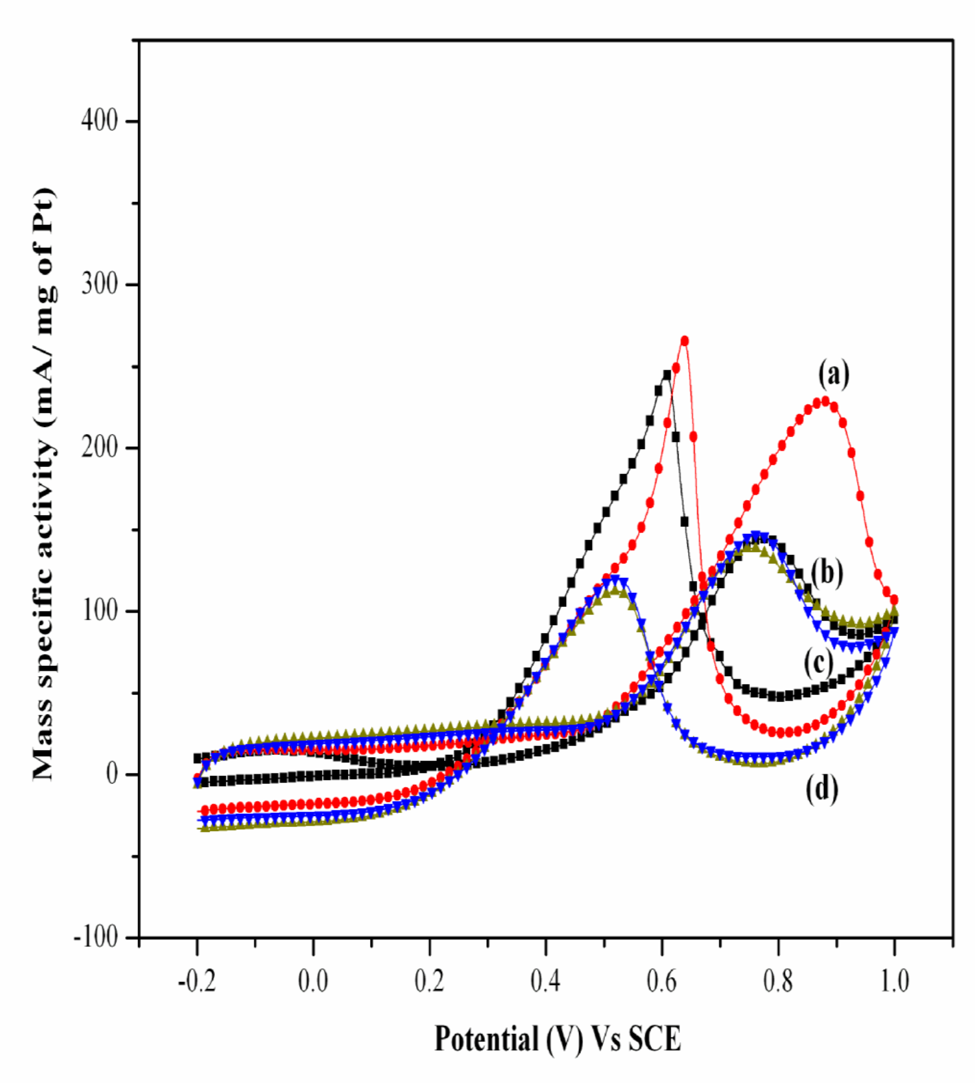

Figure 5.16: MSA of (a) 20 wt.% Pt/CNPI-1 (EG); (b) 20 wt.% Pt/NCNPI-1 (EG); (c) 20 wt.% Pt/E-TEK; (d) 20 wt.% Pt/ AC (EG) for methanol electro oxidation reaction in 1 M CH_3OH + 1 M H_2SO_4 at room temperature (scan rate: 50 mV/s).

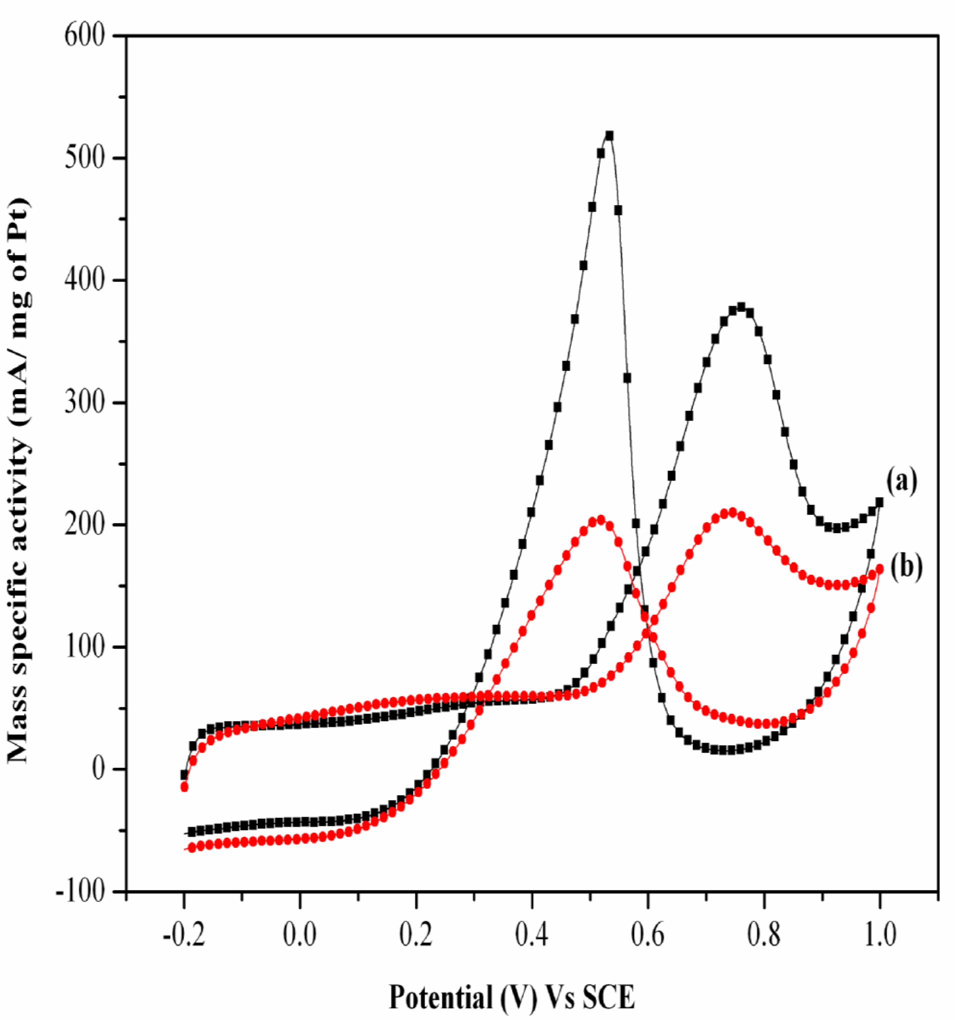

Figure 5.17: MSA of (a) 10 wt.% Pt/CNPI-1 (SBH); (b) 10 wt.% Pt/NCNPI-1 (SBH) for methanol electro oxidation reaction in 1 M CH_3OH + 1 M H_2SO_4 at room temperature (scan rate: 50 mV/s).

The onset potential values for the electro oxidation of methanol deduced from the cyclic voltammograms obtained over different electrodes, along with peak potential and current values corresponding to the methanol oxidation (anodic peak in the forward sweep) as well as the oxidation of the intermediate species formed during the oxidation of methanol (anodic peak in the reverse sweep) are summarized in Table 5.3. Liu *et al*. (2004) have reported the onset potential values of 0.27 V and 0.28 V, respectively, on Pt/Vulcan XC 72 R and Pt/CNTs for the electro oxidation of methanol in 1 M H_2SO_4 and 2 M CH_3OH at a scan rate of 50 mV/sec. Kuppan *et al.* (2011) have reported the onset potential and i_f/i_b values of 0.33 V and 0.72, respectively for 20 wt.% Pt/E-TEK (Table 5.3). 20 wt.% Pt/CNPI-1 (SBH) exhibited lower onset potential and higher $i_f/i_{b,}$ compare to commercial E-TEK catalyst. Mass specific activity and specific activity values of all the prepared Pt catalysts at + 0.7 V are tabulated (Table 5.4). 20 wt.% Pt/CNPI-1 (SBH) catalyst showed lower onset potential (0.20 V) than the commercial 40 wt.% Pt/E-TEK (0.23 V). And also, it showed a higher MSA which is an indication of higher electrochemical catalytic activity. Such a high MSA value derivable from the modest wt.% loading of Pt is an indication of the effective utilization of Pt over the CNPI-1 support. The improved performance of the electro-catalyst, 20 wt.% Pt/CNPI-1 (SBH) can be attributed to the smaller Pt nano crystallites (4.4 nm) finely dispersed over the carbon support and higher EAS. The ratio of the anodic peak current densities in the forward (i_f) and reverse (i_b) scans too gives a measure of the catalytic performance. A higher i_f/i_b ratio indicates superior oxidation activity of methanol during the anodic scan and less accumulation of carbonaceous species on the nano catalyst surface and thus an indication of better CO tolerance. All the prepared Pt catalysts show higher i_f/i_b compared to commercial Pt catalysts (Table 5.3). For comparison, Lei *et al*. (2009) have evaluated the performance of 20 wt. % Pt/Vulcan XC 72 under identical conditions and observed an i_f/i_b value of 0.89.

Table 5.3: Effect of Pt loading and the nature of the carbon support on the electro-catalytic activity of methanol oxidation of Pt/ONCs and Pt/AC.

Catalysts	Onset Potential, V	i_f/i_b	Activity*			
			Peak Current at Forward sweep		Peak Current at Reverse sweep	
			I (mA/cm^2)	E (V)	I (mA/cm^2)	E (V)
20 wt.% Pt/CNPI-1 (SBH)	0.20	0.73	67.29	0.80	92.29	0.61
20 wt.% Pt/NCNPI-1 (SBH)	0.35	1.24	51.43	0.76	41.43	0.49
20 wt.% Pt/AC (SBH)	0.34	0.91	68.86	0.92	75.86	0.67
20 wt.% Pt/CNPI-1 (EG)	0.32	0.86	65.43	0.88	75.86	0.64
20 wt.% Pt/NCNPI-1 (EG)	0.37	1.23	39.57	0.74	32.14	0.52
20 wt.% Pt/AC (EG)	0.39	1.23	42.00	0.76	34.29	0.53
10 wt.% Pt/CNPI-1 (SBH)	0.38	0.73	54.00	0.76	74.29	0.53
10 wt.% Pt/NCNPI-1 (SBH)	0.34	1.02	30.00	0.74	29.29	0.52
20% Pt/E-TEK	0.33	0.60	41.31	0.78	70.08	0.61
40% Pt/E-TEK	0.23	0.61	140.00	0.87	229.86	0.70

*Activity evaluated in 1 M H_2SO_4 and 1 M CH_3OH, at a scan rate of 50 mV/s between -0.2 to + 1.0 V Vs SCE.

Table 5.4: Effect of Pt loading and the nature of the carbon support on the EAS, MSA and SA of methanol electro oxidation of Pt/ONCs and Pt/AC at +0.7 V.

Catalysts	EAS (m^2/g)	MSA (mA/mg of Pt) at + 0.7 V	SA (A/m^2 of Pt) at + 0.7 V
20 wt.% Pt/CNPI-1 (SBH)	98.2	186.0	1.9
20 wt.% Pt/NCNPI-1 (SBH)	n.d.*	161.0	n.d.*
20 wt.% Pt/AC (SBH)	88.3	131.0	1.5
20 wt.% Pt/CNPI-1 (EG)	71.8	133.5	1.9
20 wt.% Pt/NCNPI-1 (EG)	n.d.*	125.5	n.d.*
20 wt.% Pt/AC (EG)	n.d.*	126.5	n.d.*
10 wt.% Pt/CNPI-1 (SBH)	159.1	331.9	2.1
10 wt.% Pt/NCNPI-1 (SBH)	n.d.*	196.9	n.d.*
20 wt.% Pt/E-TEK	n.d.*	116.3	n.d.*
40 wt.% Pt/E-TEK	42.6	158.3	3.7

* n.d. → not determined

5.3.6 Methanol Electro Oxidation – Effect of Scan Rate

The effect of scan rate on the electrochemical performance (current out put) of different electrodes, at the scan rates of 25, 50, 75 and 100 mV/sec in 1 M H_2SO_4 and 1 M CH_3OH between – 0.2 to + 1.0 V Vs SCE was evaluated. It was observed that the MSA values due to the methanol oxidation increased as the scan rate increased from 25 to 100 mV/s. A small increment in the peak potential with an increase in the scan rate was also observed (Fig. 5.18).

The peak currents were found to be linearly proportional to the square root of scan rates as shown in Fig. 5.19. Such a linear proportionality relationship between the current response and square root of scan rate indicates that the oxidation process of methanol is controlled by diffusion (Wang *et al.*, 2006). For all other electro-catalysts the effect of scan rate on the MSA and dependence of the peak currents on the square root of scan rates, figures were shown in appendix E.

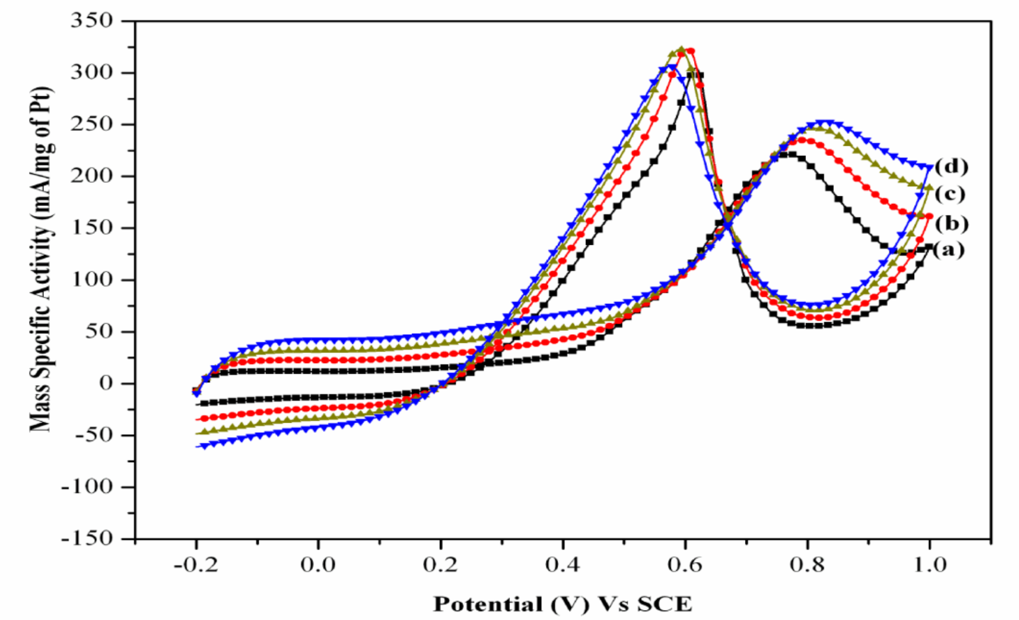

Figure 5.18: Cyclic voltammograms of 20 wt.% Pt/CNPI-1 (SBH) at different scan rates ((a) 25 mV/s; (b) 50 mV/s; (c) 75 mV/s; (d) 100 mV/s) in 1 M CH_3OH and 1 M H_2SO_4 at room temperature.

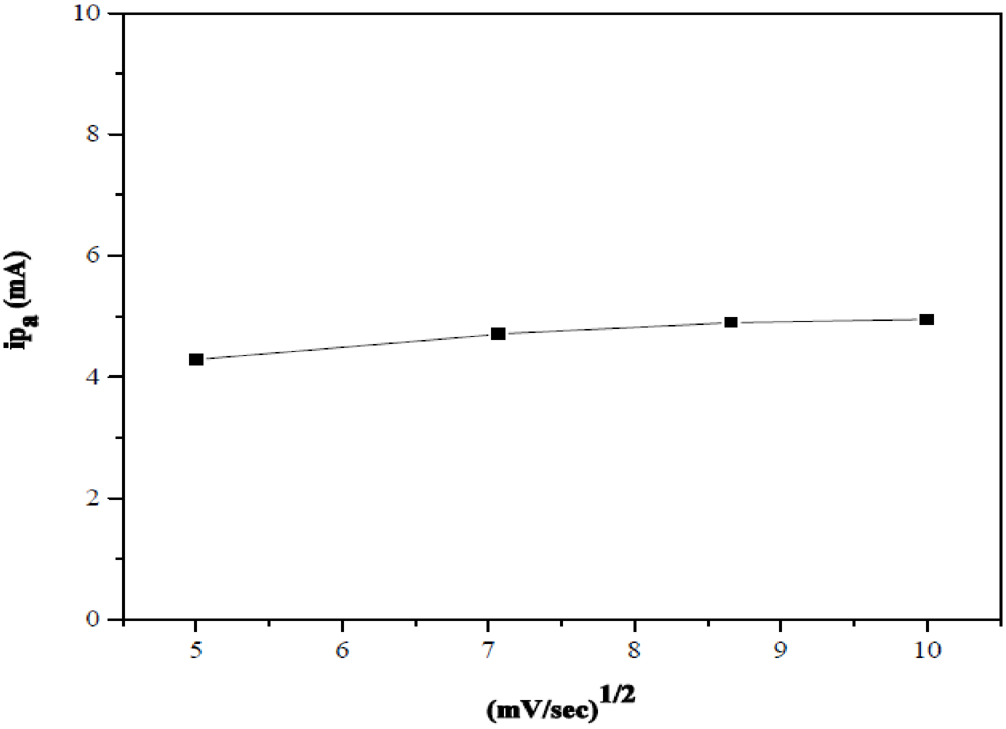

Figure 5.19: Dependence of the peak currents on the square root of scan rates for 20 wt.% Pt/CNPI-1 (SBH) in 1 M CH_3OH and 1 M H_2SO_4 at room temperature.

5.3.7 Evaluation of activity loss of the electrodes for Methanol electro oxidation by Chronoamperometry

The stable activity of the electrode under potentiostatic conditions is essential for oxidation of methanol for the possible application in DMFC. The activity loss of the fabricated electrodes was evaluated by chronoamperometric studies carried out for a duration of 0.5 h with the electrode being polarized at + 0.7 V Vs SCE in 1 M H_2SO_4 and 1 M CH_3OH. The MSA Vs time plots derived from the fabricated electrodes are shown in Fig. 5.20-5.22. There was a constant decay in the mass specific activity with respect to time, possibly suggesting the poisoning of the electrodes by CO. The initial and final (after 0.5 h) MSA values derivable from the electrodes fabricated from 20 wt.% Pt/ONCs (SBH), 20 wt.% Pt/ONCs (EG) and 10 wt.% Pt/ONCs (SBH) catalysts are summarized in Table 5.5. The percentage decrease of the activity of the aforementioned electrodes after 0.5 h was also shown in Table 5.5.

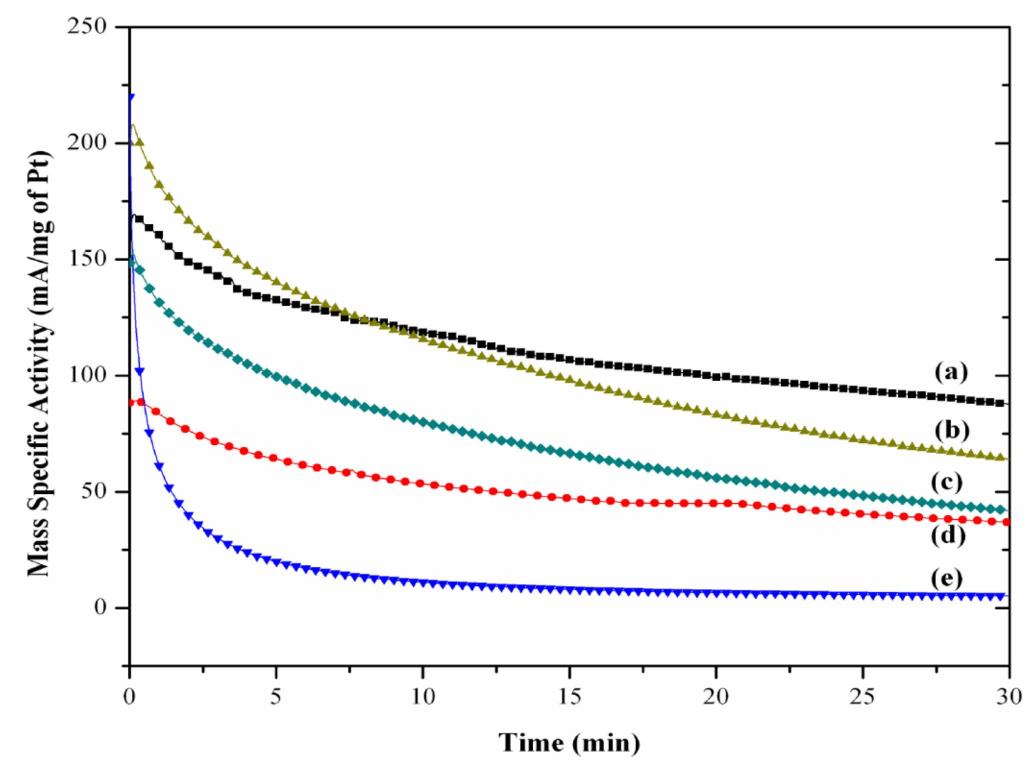

Figure 5.20: Chronoamperometry of (a) 40 wt.% Pt/E-TEK; (b) 20 wt.% Pt/CNPI-1 (SBH); (c) 20 wt.% Pt/AC (SBH); (d) 20 wt.% Pt/E-TEK; (e) 20 wt.% Pt/NCNPI-1 (SBH) for methanol electro oxidation reaction in 1 M CH_3OH + 1 M H_2SO_4 at room temperature.

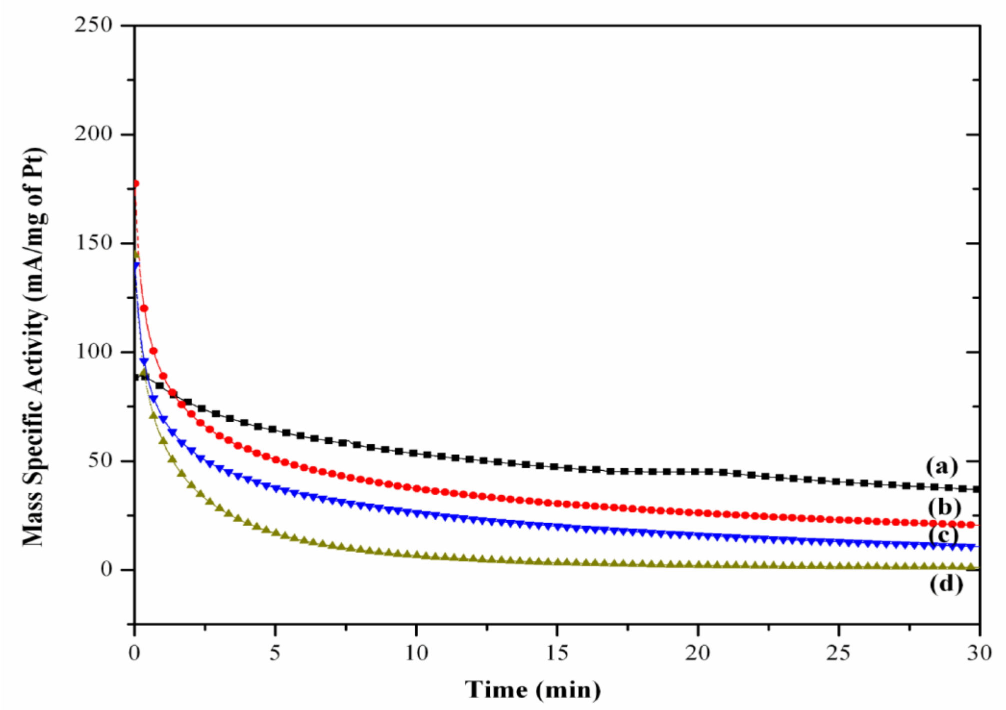

Figure 5.21: Chronoamperometry of (a) 20 wt.% Pt/E-TEK; (b) 20 wt.% Pt/CNPI-1 (EG); (c) 20 wt.% Pt/AC (EG); (d) 20 wt.% Pt/NCNPI-1 (EG) for methanol electro oxidation reaction in 1 M CH_3OH + 1 M H_2SO_4 at room temperature.

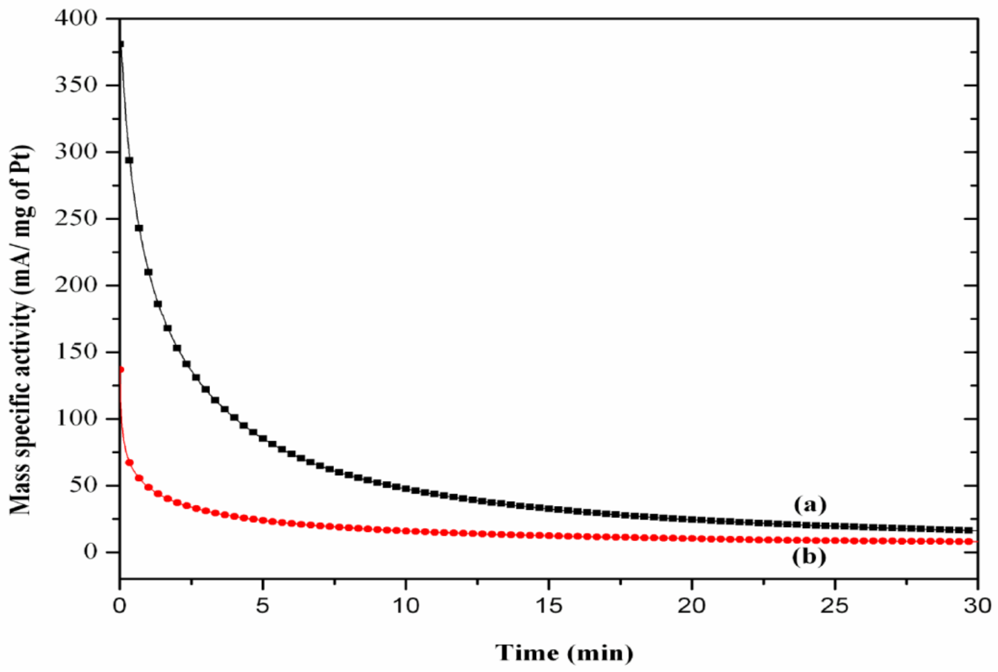

Figure 5.22: Chronoamperometry of (a) 10 wt.% Pt/CNPI-1 (SBH); (b) 10 wt.% Pt/NCNPI-1 (SBH) for methanol electro oxidation reaction in 1 M CH_3OH + 1 M H_2SO_4 at room temperature.

Table 5.5: Effect of Pt loading and the nature of the carbon support on the catalytic stable activity for methanol electro oxidation of Pt/ONCs and Pt/AC by chronoamperometry.

Catalysts	MSA*		% Decrease in activity after 0.5 h + 0.7 V
	Initial (I), mA/mg of Pt	Final (I), mA/mg of Pt	
20 wt.% Pt/CNPI-1 (SBH)	200.0	64.0	68
20 wt.% Pt/NCNPI-1 (SBH)	220.0	5.1	98
20 wt.% Pt/AC (SBH)	148.5	41.8	72
20 wt.% Pt/CNPI-1 (EG)	177.5	20.5	88
20 wt.% Pt/NCNPI-1 (EG)	144.5	1.2	99
20 wt.% Pt/AC (EG)	140.0	10.7	92
10 wt.% Pt/CNPI-1 (SBH)	380.9	16.2	96
10 wt.% Pt/NCNPI-1 (SBH)	137.0	7.9	94
20 wt.% Pt/E-TEK	88.2	36.9	58
40 wt.% Pt/E-TEK	149.3	87.8	41

* MSA evaluated in 1 M H_2SO_4 and 1 M CH_3OH for 0.5 h with the electrode being polarized at + 0.7 V Vs SCE.

The lesser activity loss of the electrode is based on the smaller crystallite size of Pt as well as the high CO tolerance (high i_f/i_b ratio value). Among the electrodes studied (excluding commercial catalysts), the 20 wt.% Pt/CNPI-1 (SBH) catalyst based electrode showed least activity loss (68 % at the end of 0.5 h). Lesser activity loss of 20 wt.% Pt/CNPI-1 can be attributed to higher dispersion of Pt nanoparticles, smaller crystallite size, higher MSA for methanol oxidation, lower onset potential and higher ESA. Even though CO tolerance of 20 wt.% Pt/CNPI-1 is less, it showed least activity loss. The reason for that behavior has to be established further. All the nitrogen containing carbon supported Pt catalyst showed higher activity loss due to the lesser concentration of nitrogen in the carbon framework. The activity loss of nitrogen containing carbon supported Pt catalyst can be reduced by better impregnation process.

CHAPTER 6

SUMMARY AND CONCLUSIONS

Ordered microporous carbon (CNPI-1) with a S_{BET} (409 m^2/g) and Vp (0.80 cm^3/g) was prepared from the H-Mordenite (template) and furfural alcohol (carbon precursor) by nanocasting method. Template removal process (HF Treatment) had been optimized for tuning the textural and morphological features of the CNPI-1 derivable. The carbon material was found to possess turbostratic graphitic structure. The CNPI-1 was employed as support for Pt and the supported catalysts (10 wt.% Pt/CNPI-1 (SBH), 20 wt.% Pt/CNPI-1 (SBH) and 20 wt.% Pt/CNPI-1 (EG)) produced by sol method were exploited as a possible electrode (anode) for the electro oxidation of methanol in Direct Methanol Fuel Cells applications.

Nitrogen containing templated microporous carbon (NCNPI-1) with a S_{BET} (218 m^2/g) and Vp (0.56 cm^3/g) was prepared from the H-Mordenite (template) and pyrrole (carbon precursor) by nanocasting method. Template removal process (HF Treatment) had been optimized for tuning the textural and morphological features of the NCNPI-1 derivable. The carbon material was found to possess turbostratic graphitic structure. The NCNPI-1 was employed as support for Pt and the supported catalysts (10 wt.% Pt/NCNPI-1 (SBH), 20 wt.% Pt/NCNPI-1 (SBH) and 20 wt.% Pt/NCNPI-1 (EG)) produced by sol method were exploited as a possible electrode (anode) for the electro oxidation of methanol in Direct Methanol Fuel Cells applications.

Different methods were tried to optimize the method for the preparation of carbon supported Pt catalysts. Finally, colloidal deposition method was found to be the best method for the preparation of methanol oxidation catalysts. Different reducing agents (SBH and EG) were also used to identify the effect of reducing agents on the dispersion of Pt nanoparticles, methanol oxidation activity and stability. Pt metal on the carbon support was found to be in FCC lattice. The lattice constant value of ~ 0.39 nm correlated well with the FCC lattice of Pt metal on the carbon support.

The crystallite size of Pt in 10 wt.% Pt/CNPI-1 (SBH), 20 wt.% Pt/CNPI-1 (SBH) and 20 wt.% Pt/CNPI-1 (EG) catalysts were respectively, 4.3, 4.8 and 6.0 nm. The crystallite size of Pt in 10 wt.% Pt/NCNPI-1 (SBH), 20 wt.% Pt/NCNPI-1 (SBH) and 20 wt.% Pt/NCNPI-1 (EG) catalysts were respectively, 4.5, 4.0 and 6.2 nm. Thus the crystallite size of Pt which is the critical parameter governing the electro-catalytic property of Pt/C catalysts was found to be dependent on the Pt loading, nature of reducing agent and also the nature of the carbon support employed.

The methanol oxidation reaction carried out on Pt/C catalysts was monitored by cyclic voltammetry. Irrespective of the carbon support and the amount of the active component, two anodic peaks appeared in the cyclic voltammogram, one in the forward scan and the other in the reverse scan respectively attributable to the oxidation of methanol and the removal of the incompletely oxidized carbonaceous species formed in the forward scan. Among different electro-catalysts evaluated, the 20 wt.% Pt/CNPI-1 (SBH) exhibited high MSA value (186 mA/mg of Pt) which is an indication of higher electrochemical activity at a relatively lower onset potential value (0.20 V). Only 68 % loss in the initial activity at the end of 0.5 h was observed in the case of 20 wt.% Pt/CNPI-1 (SBH) compared to 72 and 98 % activity losses observed in the cases of 20 wt. % Pt/AC (SBH) and 20 wt.% Pt/NCNPI-1 (SBH) as indicated from the chronoamperometric studies implying lesser activity loss of 20 wt.% Pt/CNPI-1 (SBH).

CNPI-1 was identified to be a promising support for electrode application in DMFC. SBH reduced Pt catalysts supported on CNPI-1 showed higher dispersion of Pt nanoparticles, smaller crystallite size, higher MSA for methanol oxidation, lower onset potential and better stability. But it lacked high CO tolerance capacity. Even NCNPI-1 as a support for Pt catalyst showed higher dispersion of Pt nanoparticles, smaller crystallite size, higher activity and high CO tolerance. But Pt/NCNPI-1 showed higher onset potential and higher activity loss (due to less concentration of Nitrogen in the carbon framework) compared to Pt/CNPI-1. The 20 wt.% Pt/CNPI-1 (SBH) was found to possess sufficient electro-active surface area with finely dispersed nanosized Pt particles of < 5 nm, which correlated well with the observed higher methanol oxidation activity and lesser activity loss under potentiostatic conditions.

APPENDIX A

A.1 EDX SPECTRAS OF ONCS

A.1.1 EDX Spectras of CNPI-1

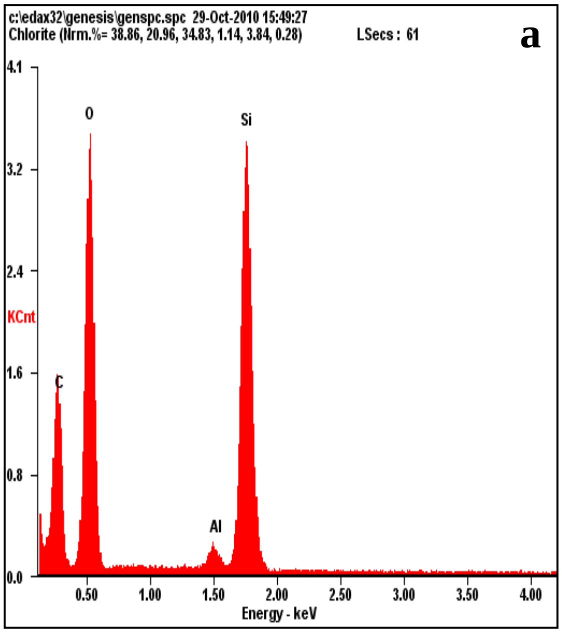

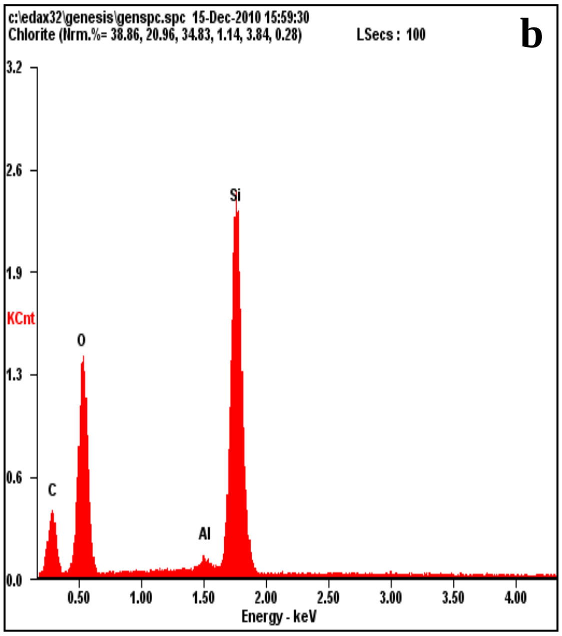

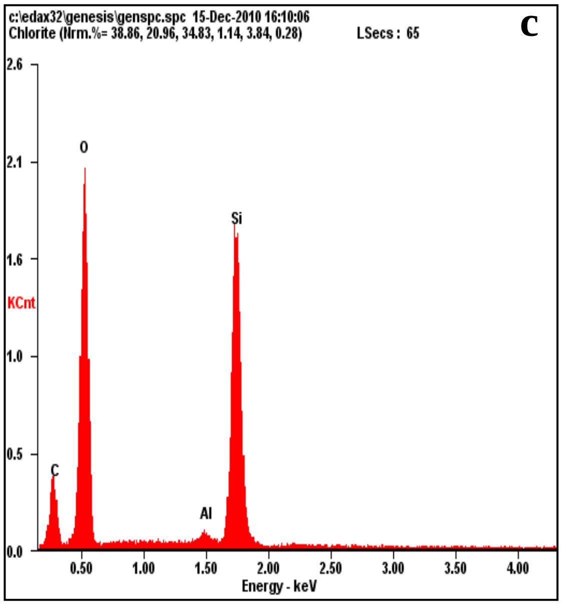

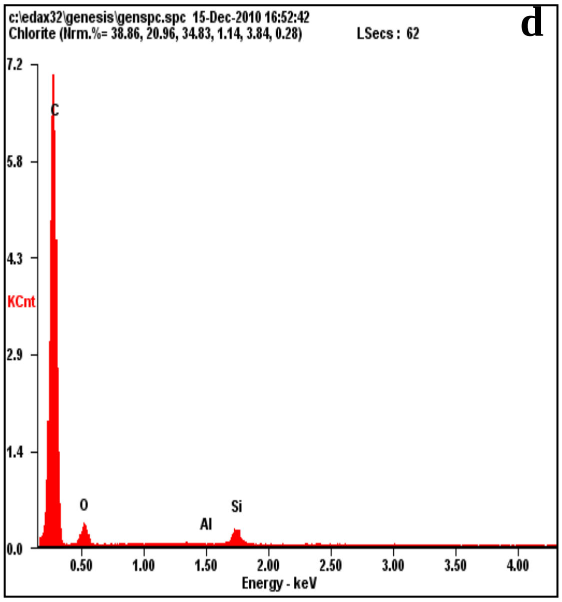

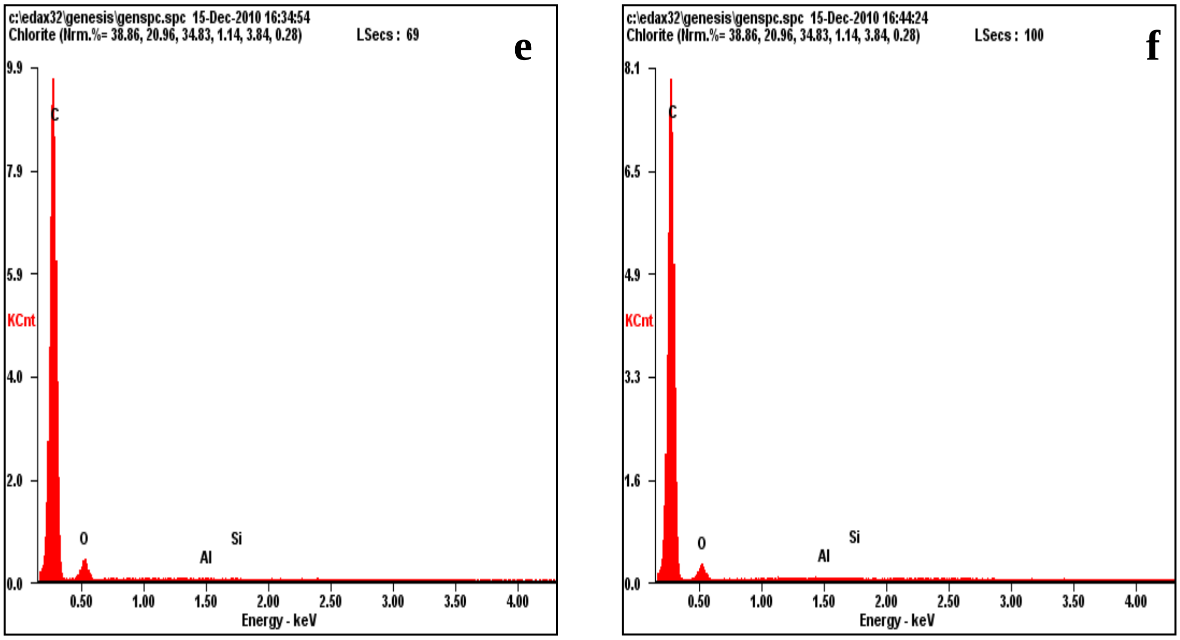

Figure A.1: EDX Spectras of (a) H-Mordenite; (b) FA / H-MOR composite; (c) Heat treated sample; (d) CNPI-1 (2 % HF; 9 h); (e) CNPI-1 (5 % HF; 3 h); (f) CNPI-1 (5 % HF; 6 h).

A.1.2 EDX Spectras of NCNPI-1

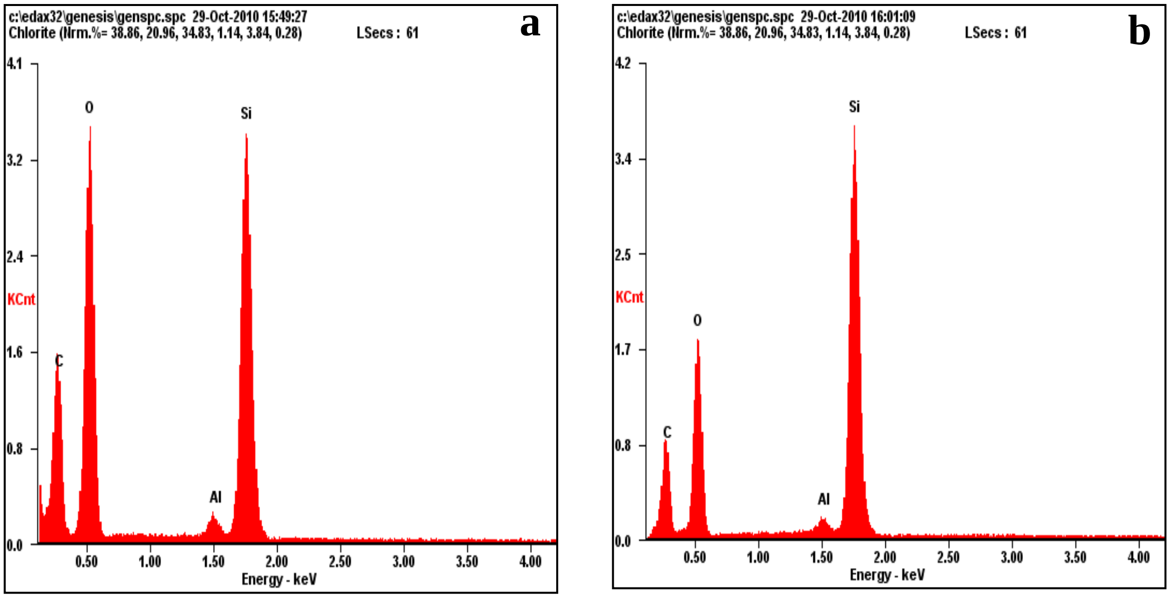

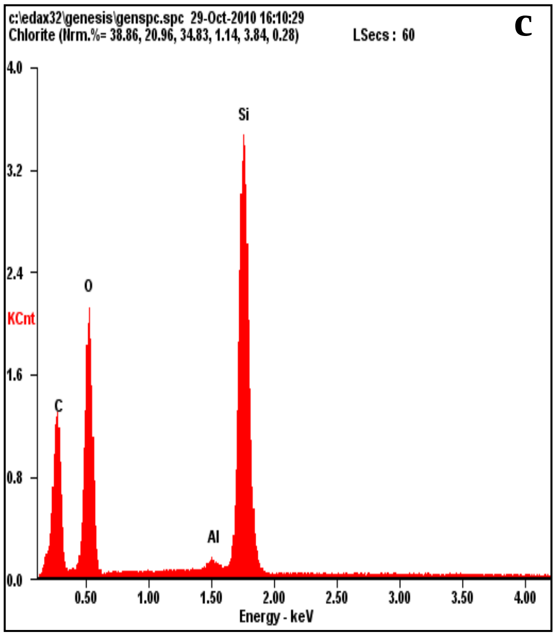
c:\edax32\genesis\genspc.spc 29-Oct-2010 16:10:29
Chlorite (Nrm.%= 38.86, 20.96, 34.83, 1.14, 3.84, 0.28)
LSecs : 60
c
4.0
3.2
2.4
KCnt
1.6
0.8
0.0
Si
O
C
Al
0.50
1.00
1.50
2.00
2.50
3.00
3.50
4.00
Energy - keV

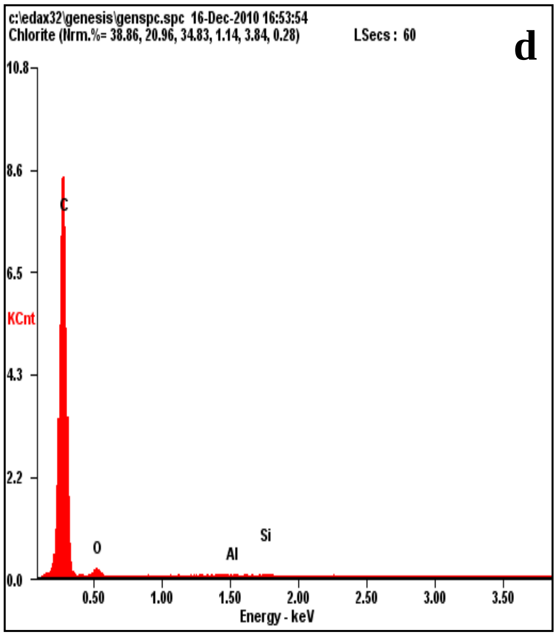
c:\edax32\genesis\genspc.spc 16-Dec-2010 16:53:54
Chlorite (Nrm.%= 38.86, 20.96, 34.83, 1.14, 3.84, 0.28)
LSecs : 60
d
10.8
8.6
6.5
KCnt
4.3
2.2
0.0
C
O
Al
Si
0.50
1.00
1.50
2.00
2.50
3.00
3.50
Energy - keV

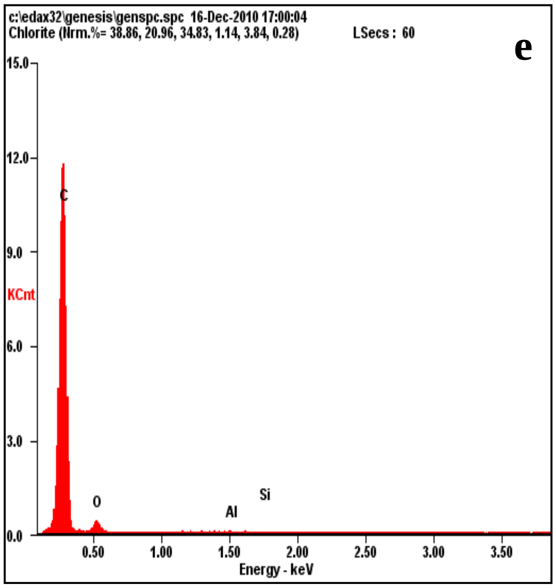
c:\edax32\genesis\genspc.spc 16-Dec-2010 17:00:04
Chlorite (Nrm.%= 38.86, 20.96, 34.83, 1.14, 3.84, 0.28)
LSecs : 60
e
15.0
12.0
9.0
KCnt
6.0
3.0
0.0
C
O
Al
Si
0.50
1.00
1.50
2.00
2.50
3.00
3.50
Energy - keV

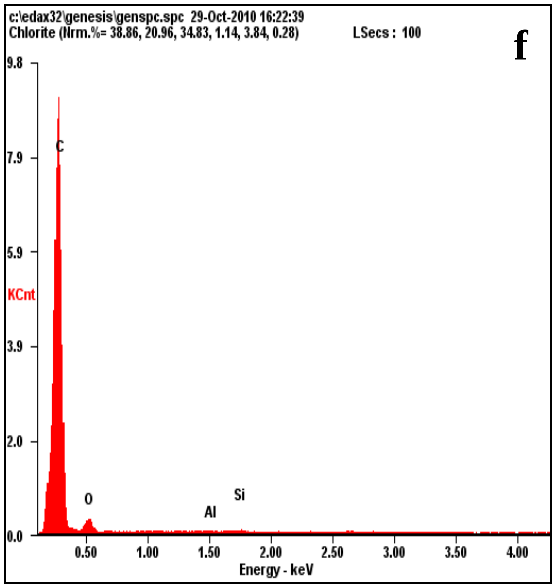
c:\edax32\genesis\genspc.spc 29-Oct-2010 16:22:39
Chlorite (Nrm.%= 38.86, 20.96, 34.83, 1.14, 3.84, 0.28)
LSecs : 100
f
9.8
7.9
5.9
KCnt
3.9
2.0
0.0
C
O
Al
Si
0.50
1.00
1.50
2.00
2.50
3.00
3.50
4.00
Energy - keV

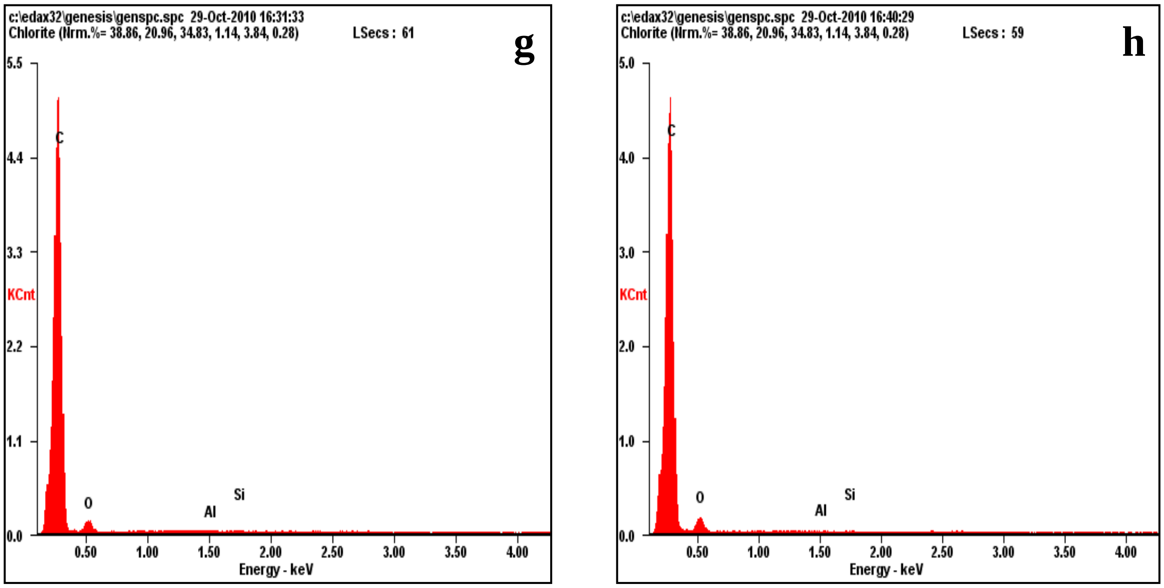

Figure A.2: EDX spectras of (a) H-Mordenite; (b) Pyrrole / H-MOR composite; (c) Heat treated sample; (d) NCNPI-1 (5 % HF; 1 h); (e) NCNPI-1 (5 % HF; 2 h); (f) NCNPI-1 (5 % HF; 3 h); (g) NCNPI-1 (5 % HF; 6 h); (h) NCNPI-1 (5 % HF; 9 h).

APPENDIX B

B.1 PREPARATION OF ONC FROM H-MORDENITE AND SUCROSE

The micropores in the H-Mordenite template were impregnated with sucrose and sulfuric acid using their aqueous solution. The template after the impregnation was heated at a temperature of 900 °C for 3 h in an inert atmosphere. The sucrose was converted to carbon by such a process using sulfuric acid as the catalyst. Finally, the template was removed by HF treatment (40 %) (Ryoo *et al.,* 1999). The resultant templated microporous carbon material was referred to as CNPI-9. Then the prepared CNPI-9 was characterized by XRD, BET and SEM.

B.2 CHARACTERIZATION

B.2.1 XRD

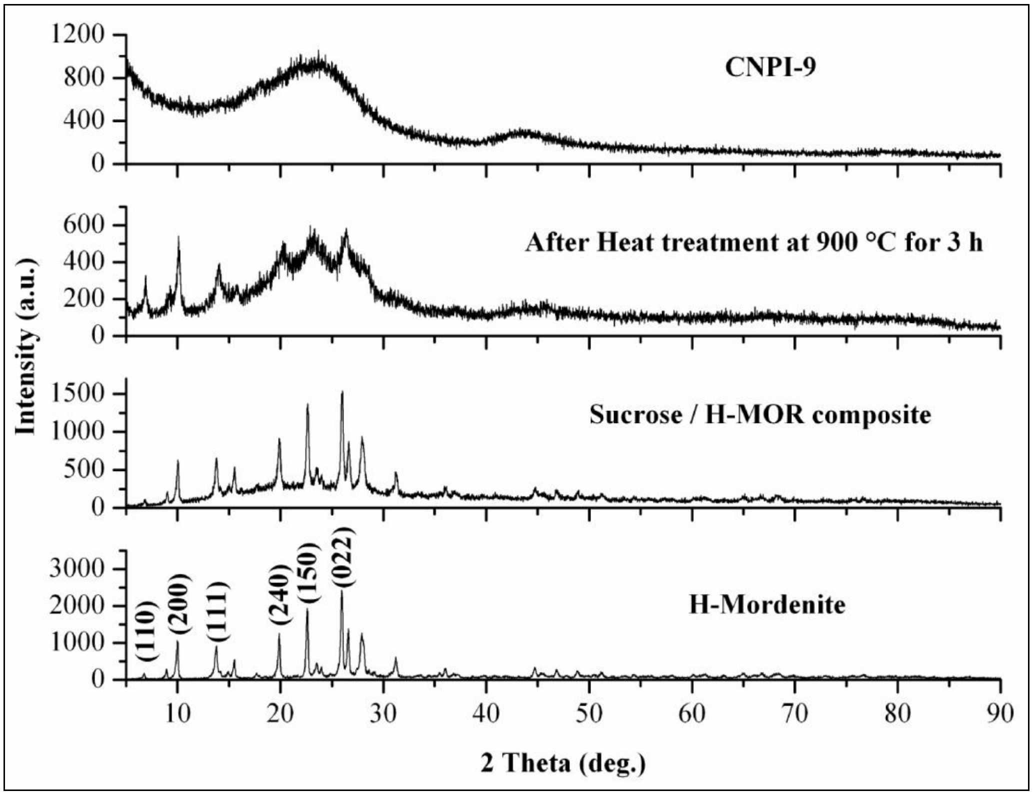

Figure B.1: XRD pattern of CNPI-9.

XRD patterns of the CNPI-9 samples are shown in Fig. B.1. Sucrose / H-MOR composite retained the ordered structure of the H-Mordenite. During the heat treatment itself the structure started collapsing. It was evident form the XRD pattern. During the HF treatment, CNPI-9 from template can collapse and form an amorphous like structure due to insufficient impregnation of the precursor. Therefore, template removal process has to be optimized to get an ordered carbon structure. In this case, 40 % HF was used for 24 h in order to remove the template. After the HF treatment, amorphous kind of CNPI-9 was obtained.

B.2.2 Textural properties

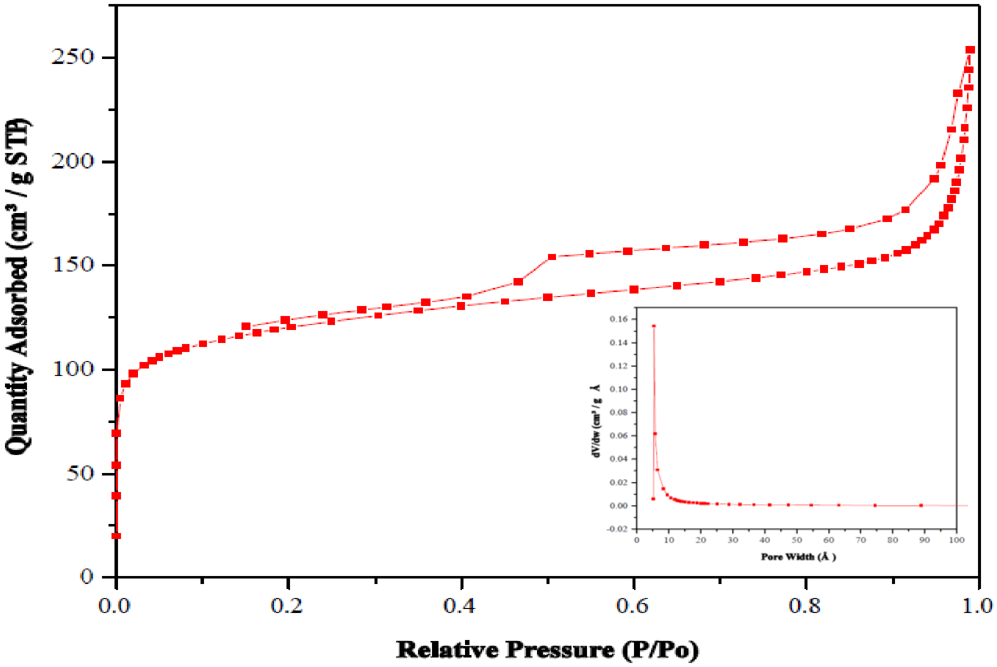

Figure B.2: N_2 sorption isotherm of CNPI-9. Inset: Pore size distribution of CNPI-9.

Table B.1: Textural properties of CNPI-9.

Microporous carbon	BET surface area (m^2/g)	Pore volume (cm^3/g)	Avg. Pore size (Å)
CNPI-9	440	0.37	5.36

B.2.3 SEM

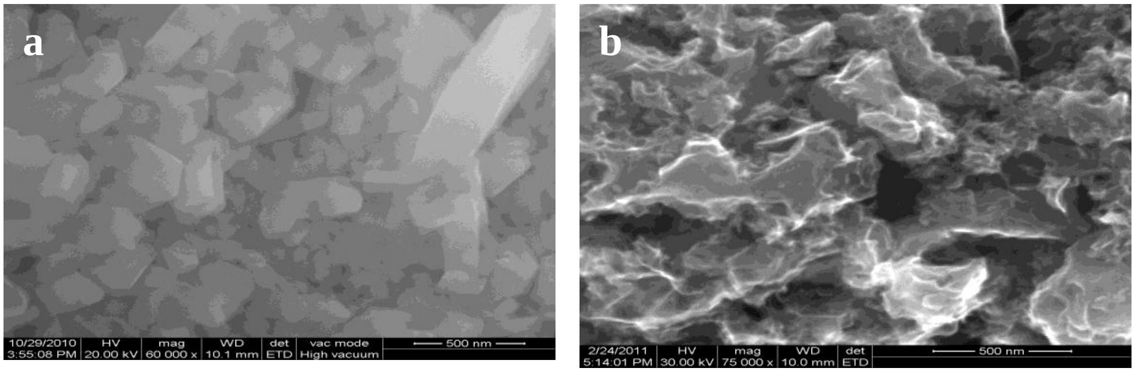

Figure B.3: SEM images of (a) H-Mordenite; (b) CNPI-9.

B.2.4. EDX

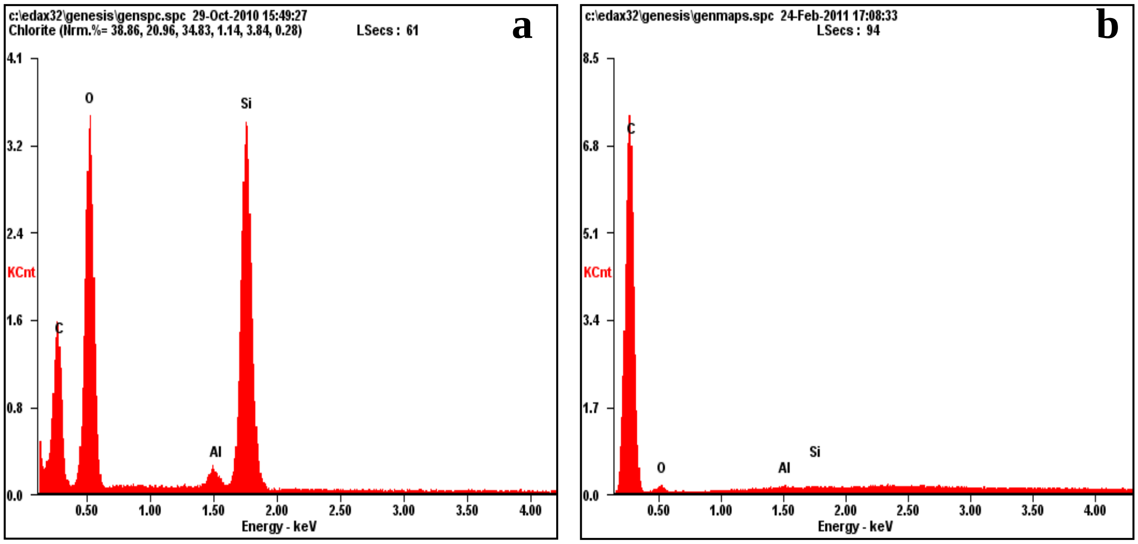

Figure B.4: EDX spectra of (a) H-Mordenite; (b) CNPI-9.

Table B.2: Elemental analysis results of CNPI-9.

Sample names	Composition (Atom %)			
	C	O	Al	Si
H-Mordenite	40.0	51.8	0.5	7.8
CNPI-9	97.2	2.7	0.07	0.03

APPENDIX C

C.1 PREPARATION OF ONCS USING ZEOLITE Y (Na-Y)

C.1.1 Furfural alcohol as a precursor

1 g of template (Na-Y) was impregnated with 4 ml of furfural alcohol and stirred for overnight. And then the suspension was filtered and washed with mesitylene to remove the carbon from the external surface of the template. Then the filtered sample was dried at 80 °C for 24 h and polymerized at 150 °C for 8 h. The polymerized sample was heat treated in the N_2 atmosphere for 700 °C for 3 h at the rate of 5 °C/min. After the heat treatment, the acquired sample was HF treated to remove the template and dried at 120 °C (Kyotani *et al.,* 1997). The obtained product was designated as CNPI-2. Then the prepared CNPI-2 was characterized by XRD and SEM. After HF treatment instead of forming microporous carbon, it formed stable sodium aluminum fluoride. Therefore extensive washing is required to remove that stable compound. The formation of that stable compound can be avoided by using H-Y.

C.1.2 Sucrose as a precursor

The micropores in the Zeolite Y (Na-Y) template were impregnated with sucrose and sulfuric acid using their aqueous solution. The template after the impregnation was heated at a temperature of 900 °C for 3 h in an inert atmosphere. The sucrose was converted to carbon by such a process using sulfuric acid as the catalyst. Finally, the template was removed by HF treatment (40 %) (Ryoo *et al.,* 1999). The resultant product material was designated as CNPI-8. Then the prepared CNPI-8 was characterized by XRD and SEM. After HF treatment instead of forming microporous carbon, it formed stable sodium aluminum fluoride. Therefore extensive washing is required to remove that stable compound.

C.2 CHARACTERIZATION

C.2.1 XRD

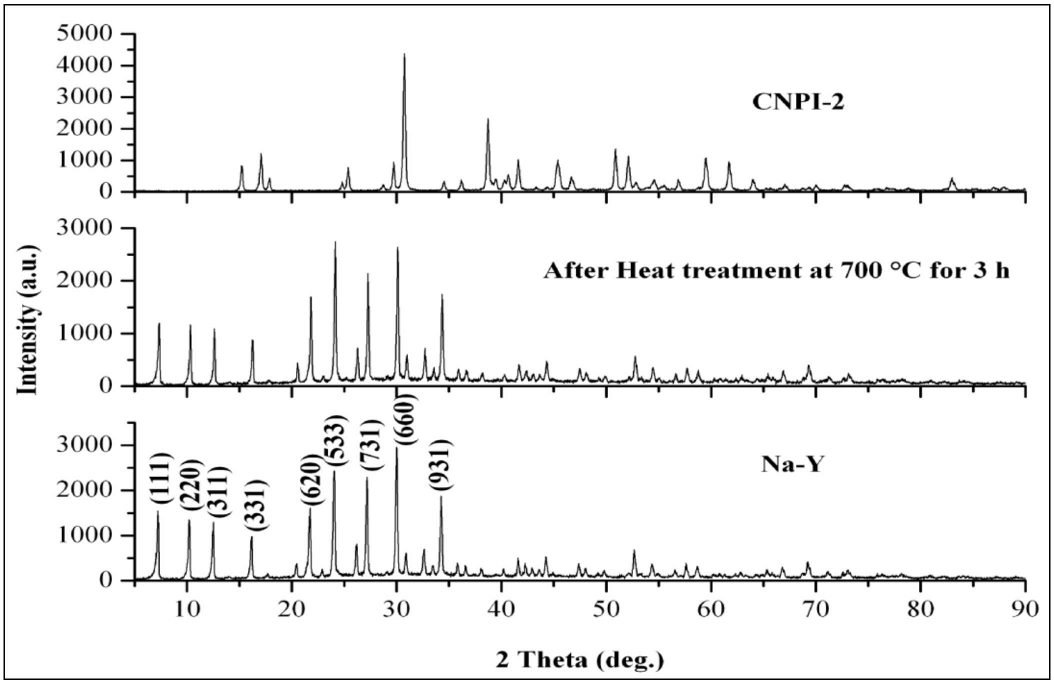

Figure C.1: XRD pattern of CNPI-2.

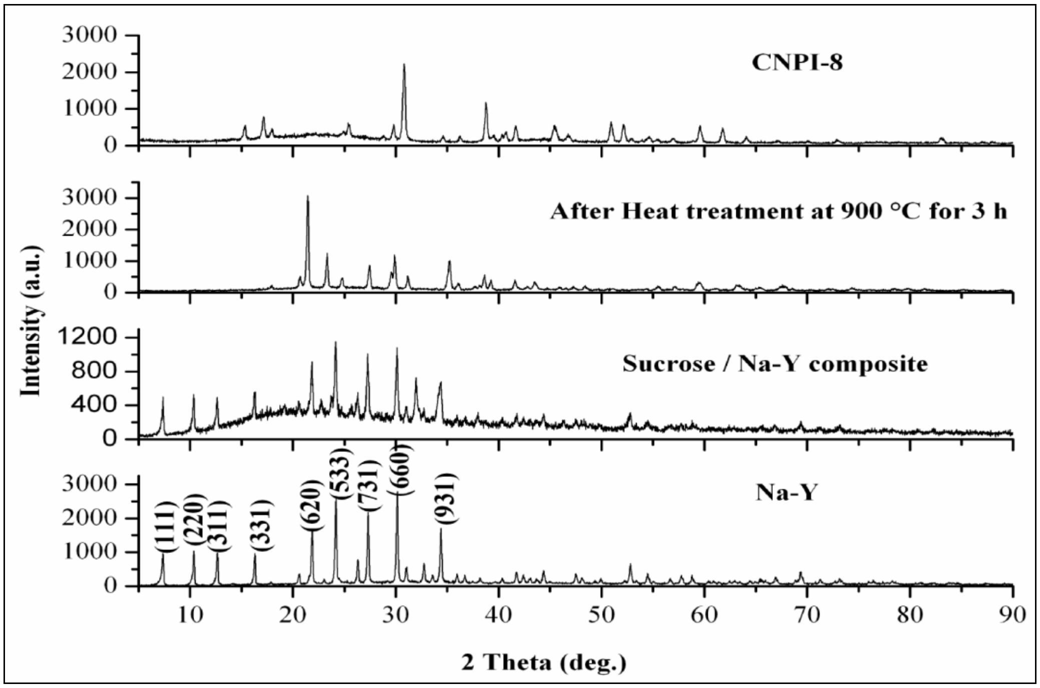

Figure C.2: XRD pattern of CNPI-8.

C.2.2 SEM

SEM Images of CNPI-2

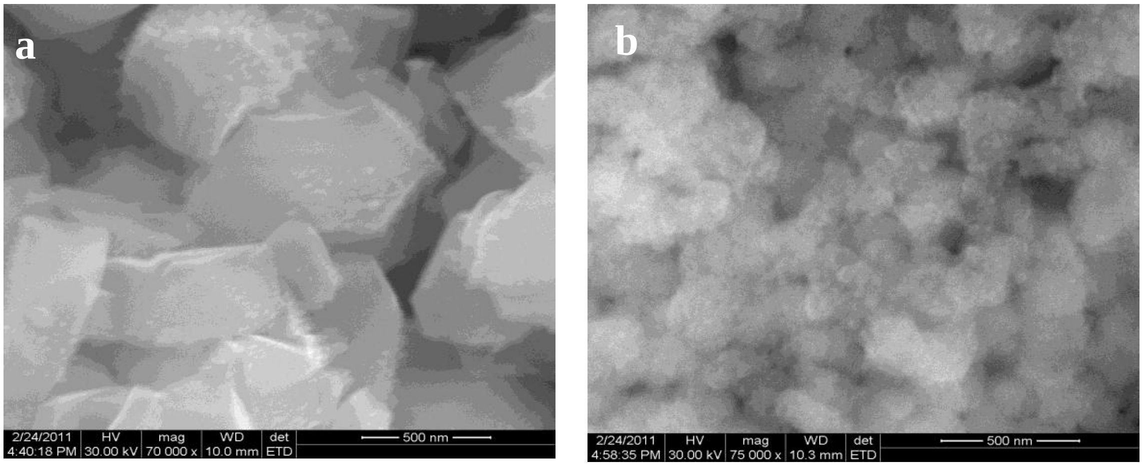

Figure C.3: SEM images of (a) Na-Y; (b) CNPI-2.

SEM Images of CNPI-8

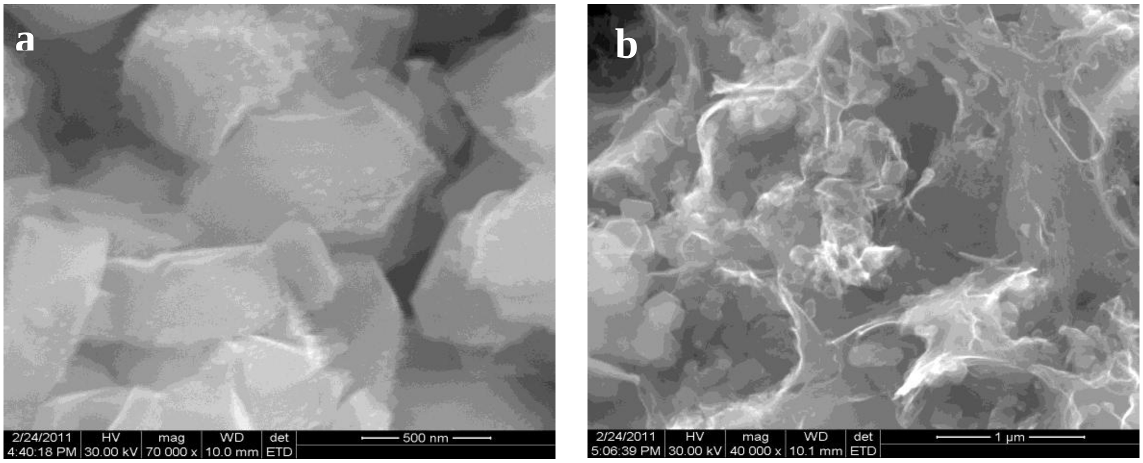

Figure C.4: SEM images of (a) Na-Y; (b) CNPI-8.

C.2.3. EDX

EDX Spectra of CNPI-2

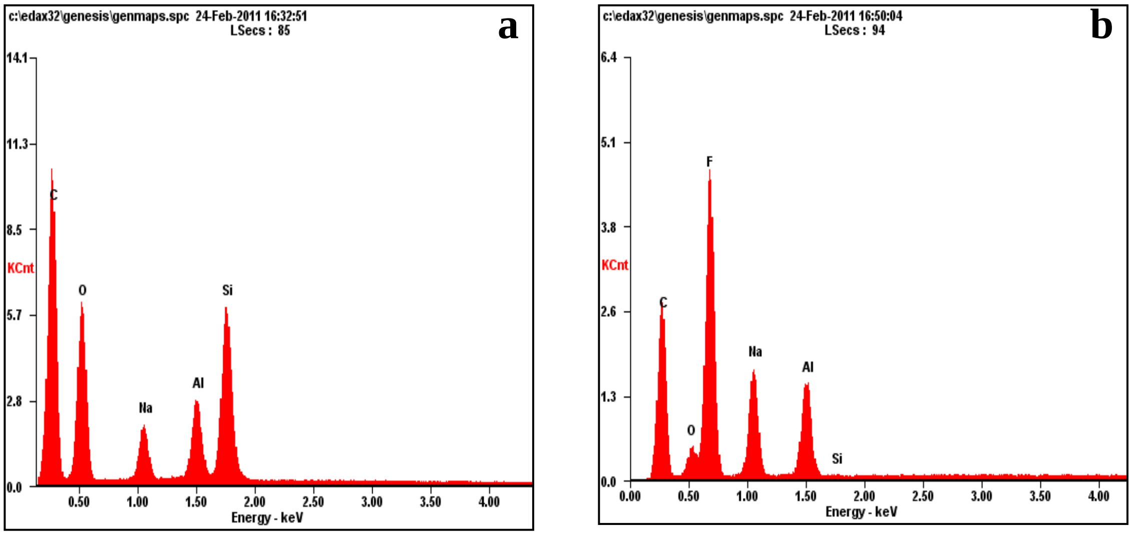

Figure C.5: EDX Spectra of (a) Na-Y; (b) CNPI-2.

EDX Spectra of CNPI-8

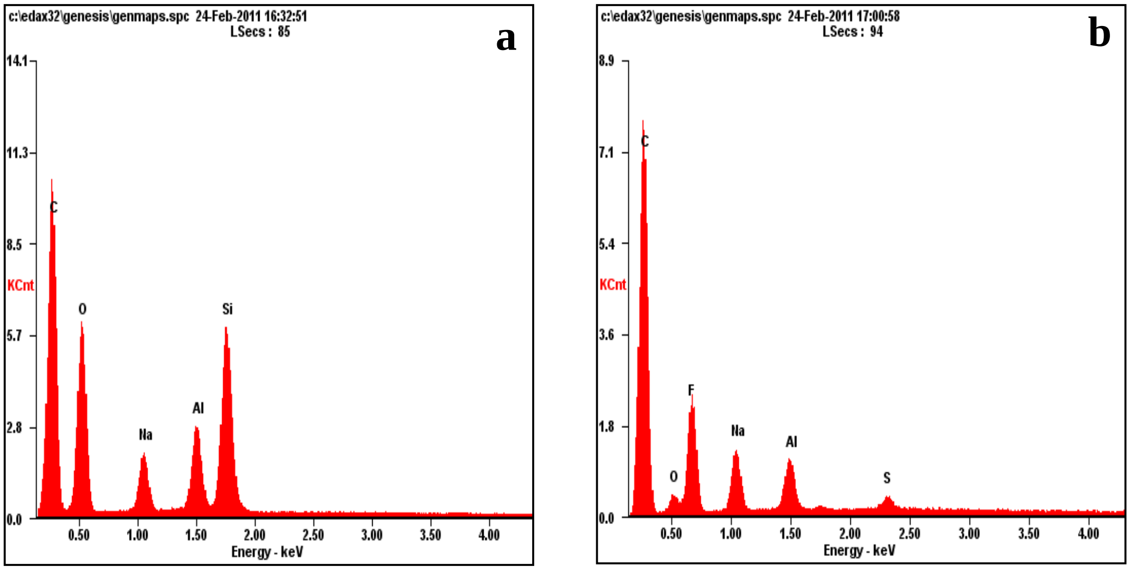

Figure C.6: EDX Spectra of (a) Na-Y; (b) CNPI-8.

Table C.1: Elemental analysis results of CNPI-2.

Sample Names	Composition (Atom %)					
	C	O	F	Na	Al	Si
Zeolite Y (Na-Y)	70.7	24.7	-	1.6	1.1	2.0
CNPI-2	63.7	5.0	24.2	5.0	2.1	0.02

Table C.2: Elemental analysis results of CNPI-8.

Sample Names	Composition (Atom %)					
	C	O	F	Na	Al	Si
Zeolite Y (Na-Y)	70.7	24.7	-	1.6	1.1	2.0
CNPI-8	83.4	3.5	10.1	2.1	0.79	0.12

APPENDIX D

D.1 AREA USED FOR ESA CALCULATIONS

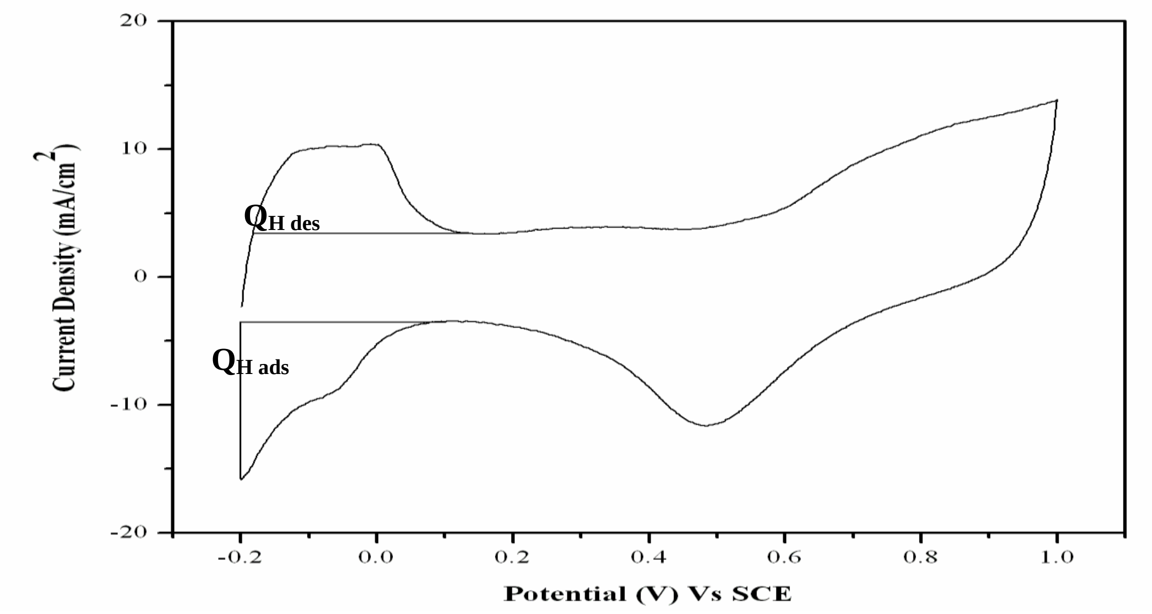

Figure D.1: Cyclic Voltammogram of 40 wt.% Pt/E-TEK catalyst in 1 M H_2SO_4 at room temperature (scan rate: 50 mV/s).

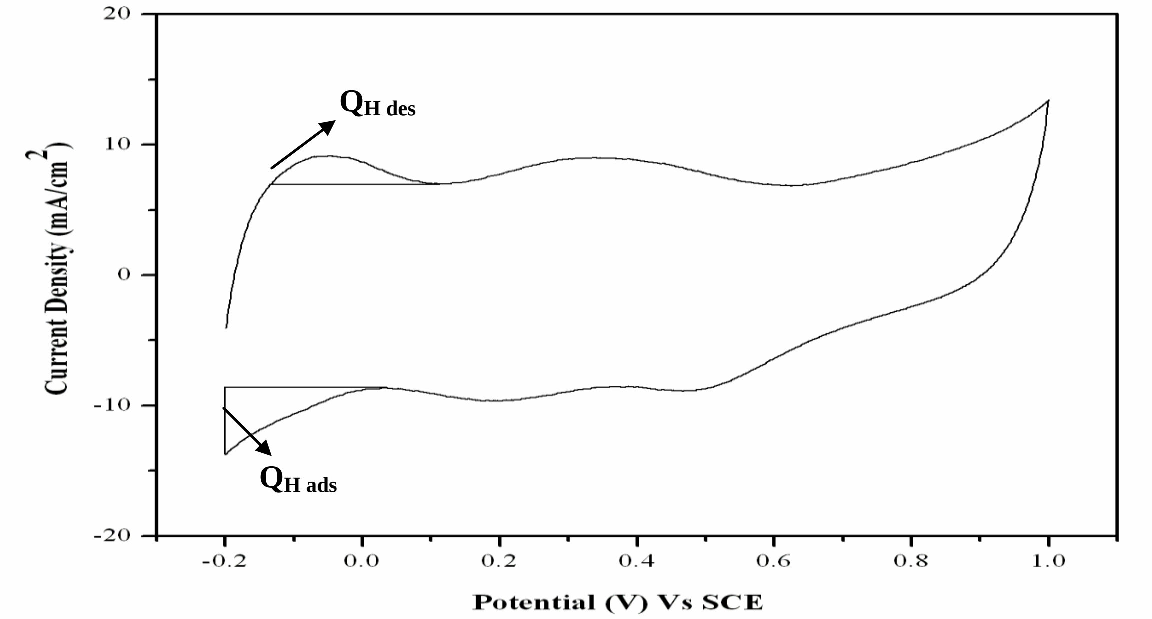

Figure D.2: Cyclic Voltammogram of 20 wt.% Pt/CNPI-1 (SBH) catalyst in 1 M H_2SO_4 at room temperature (scan rate: 50 mV/s).

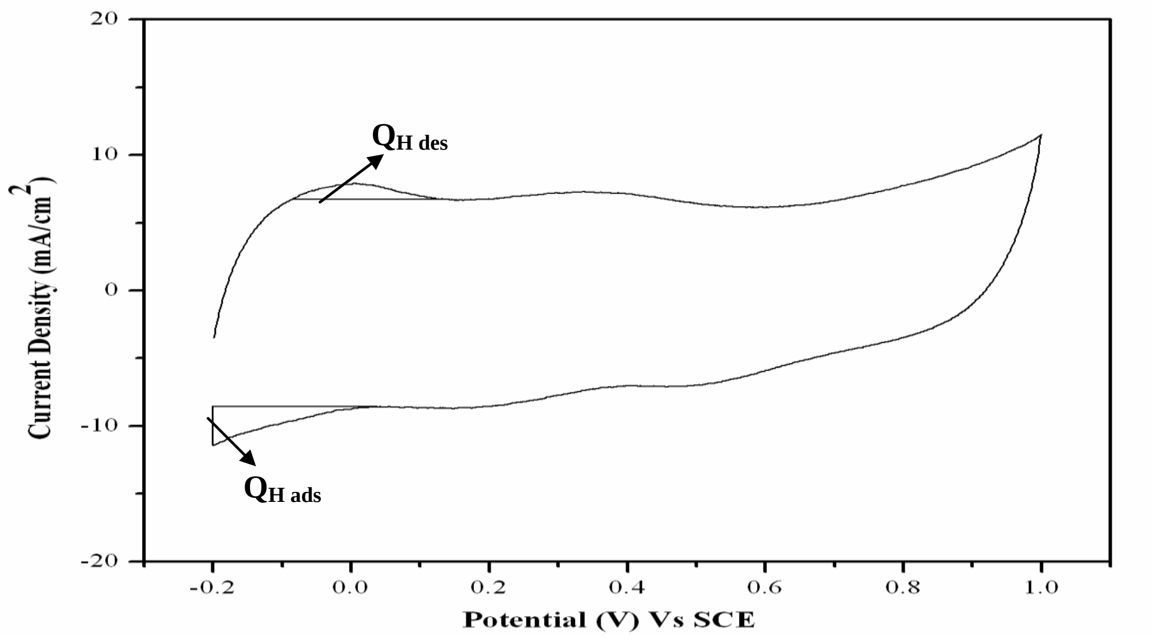

Figure D.3: Cyclic Voltammogram of 20 wt.% Pt/AC (SBH) catalyst in 1 M H_2SO_4 at room temperature (scan rate: 50 mV/s).

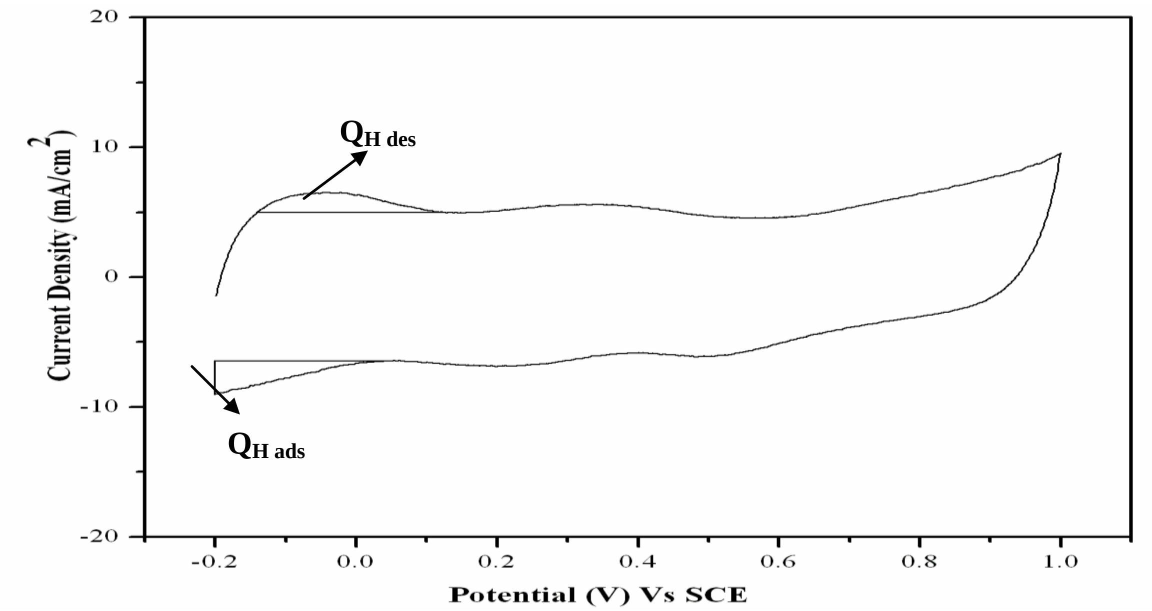

Figure D.4: Cyclic Voltammogram of 20 wt.% Pt/CNPI-1 (EG) catalyst in 1 M H_2SO_4 at room temperature (scan rate: 50 mV/s).

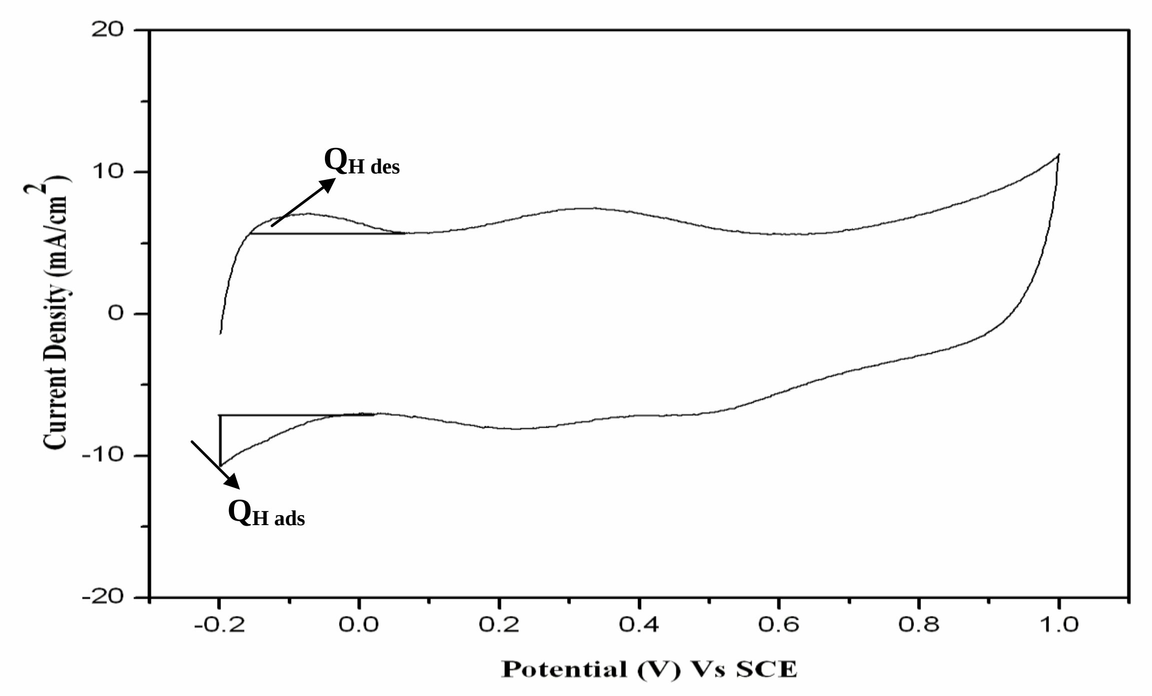

Figure D.5: Cyclic Voltammogram of 10 wt.% Pt/CNPI-1 (SBH) catalyst in 1 M H_2SO_4 at room temperature (scan rate: 50 mV/s).

APPENDIX E

E.1 METHANOL ELECTRO OXIDATION – EFFECT OF SCAN RATE

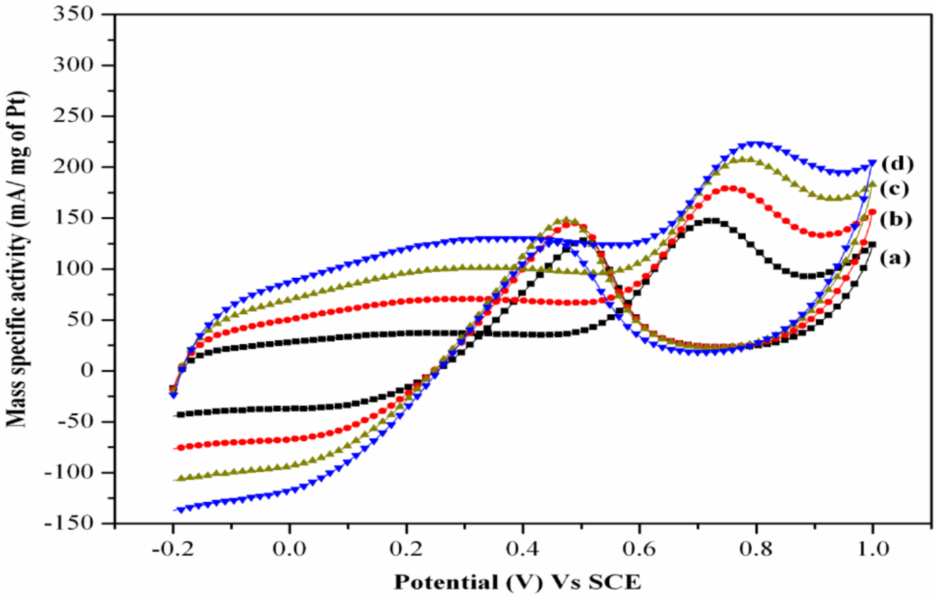

Figure E.1: Cyclic voltammograms of 20 wt.% Pt/NCNPI-1 (SBH) at different scan rates ((a) 25 mV/s; (b) 50 mV/s; (c) 75 mV/s; (d) 100 mV/s) in 1 M H_2SO_4 and 1 M CH_3OH at room temperature.

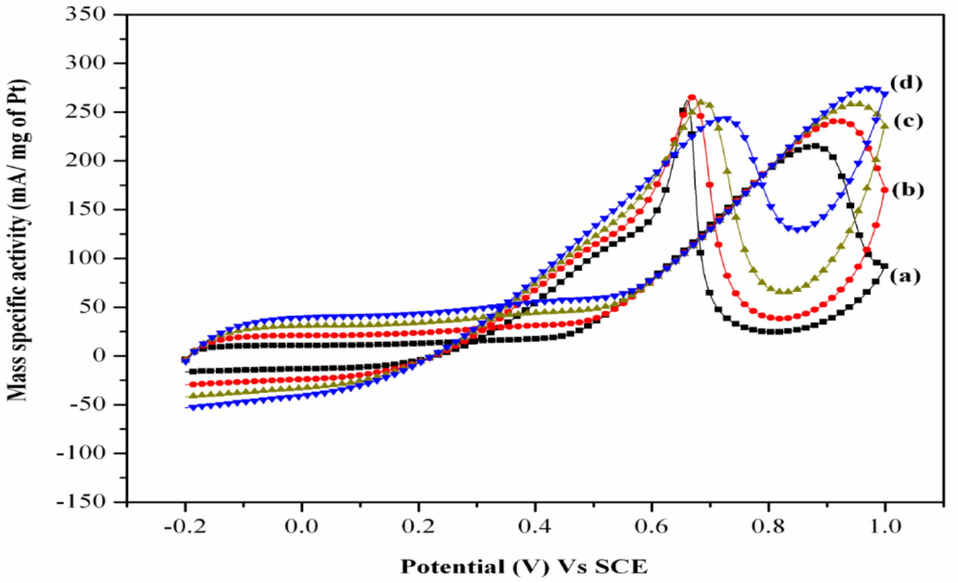

Figure E.2: Cyclic voltammograms of 20 wt.% Pt/AC (SBH) at different scan rates ((a) 25 mV/s; (b) 50 mV/s; (c) 75 mV/s; (d) 100 mV/s) in 1 M H_2SO_4 and 1 M CH_3OH at room temperature.

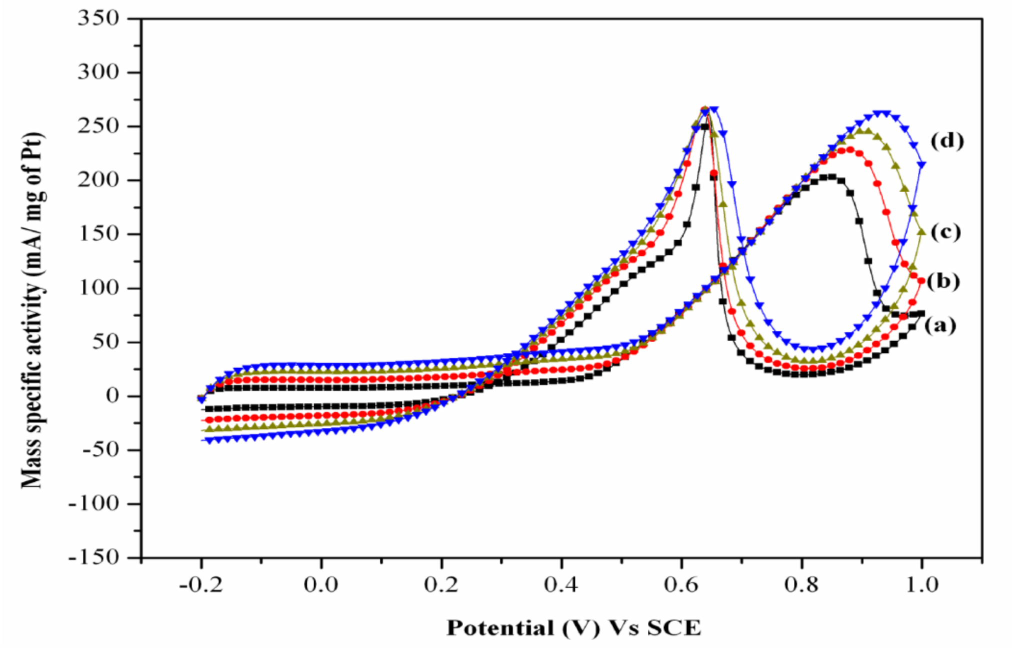

Figure E.3: Cyclic voltammograms of 20 wt.% Pt/CNPI-1(EG) at different scan rates ((a) 25 mV/s; (b) 50 mV/s; (c) 75 mV/s; (d) 100 mV/s) in 1 M H_2SO_4 and 1 M CH_3OH at room temperature.

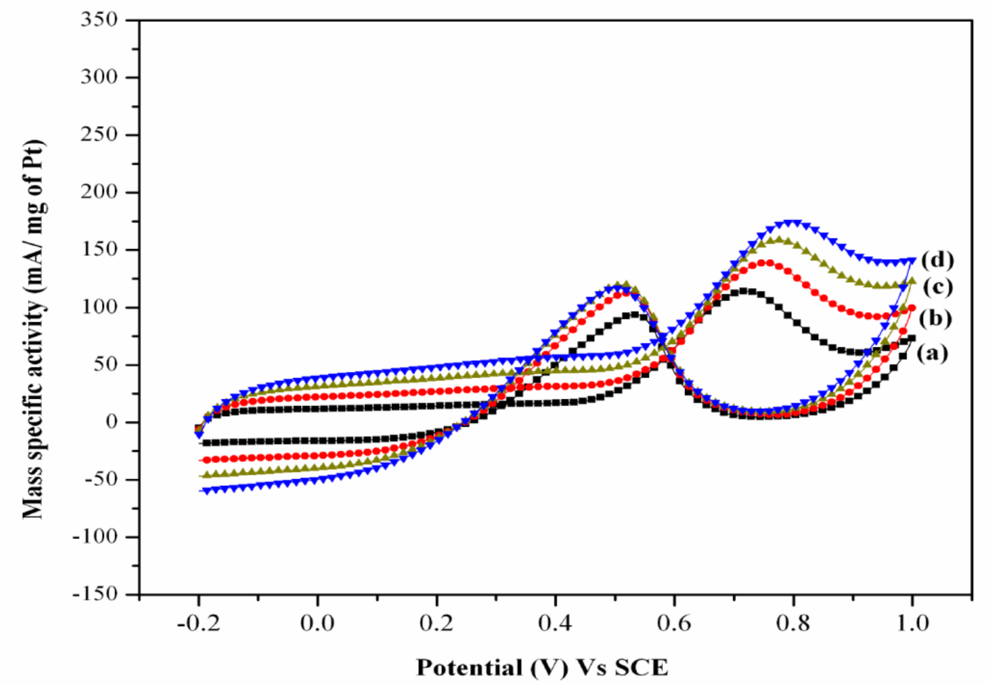

Figure E.4: Cyclic voltammograms of 20 wt.% Pt/NCNPI-1(EG) at different scan rates ((a) 25 mV/s; (b) 50 mV/s; (c) 75 mV/s; (d) 100 mV/s) in 1 M H_2SO_4 and 1 M CH_3OH at room temperature.

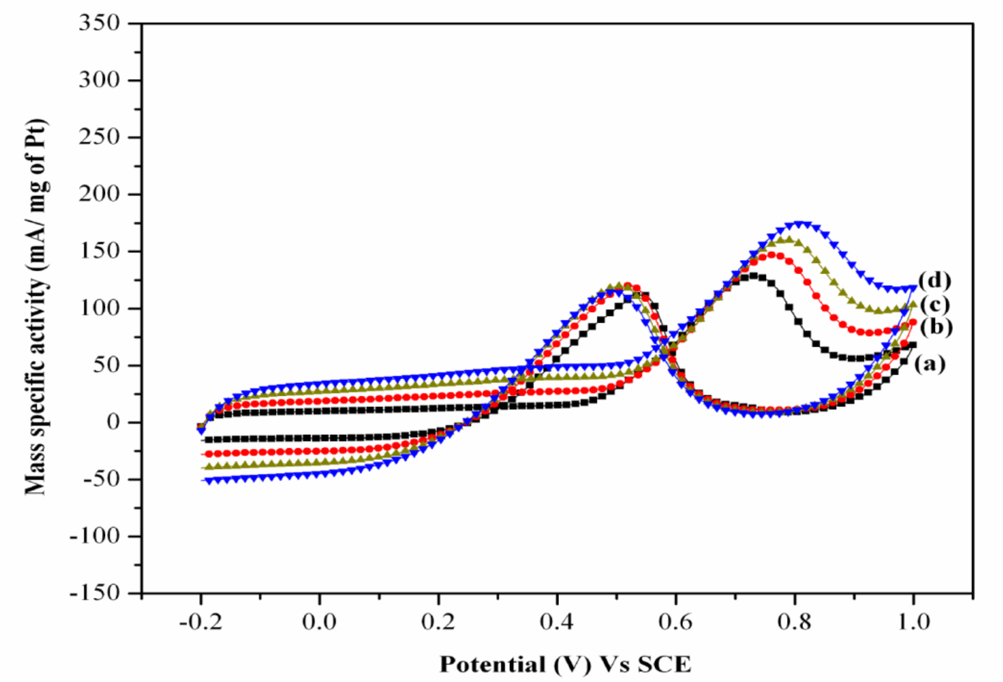

Figure E.5: Cyclic voltammograms of 20 wt.% Pt/AC (EG) at different scan rates ((a) 25 mV/s; (b) 50 mV/s; (c) 75 mV/s; (d) 100 mV/s) in 1 M H_2SO_4 and 1 M CH_3OH at room temperature.

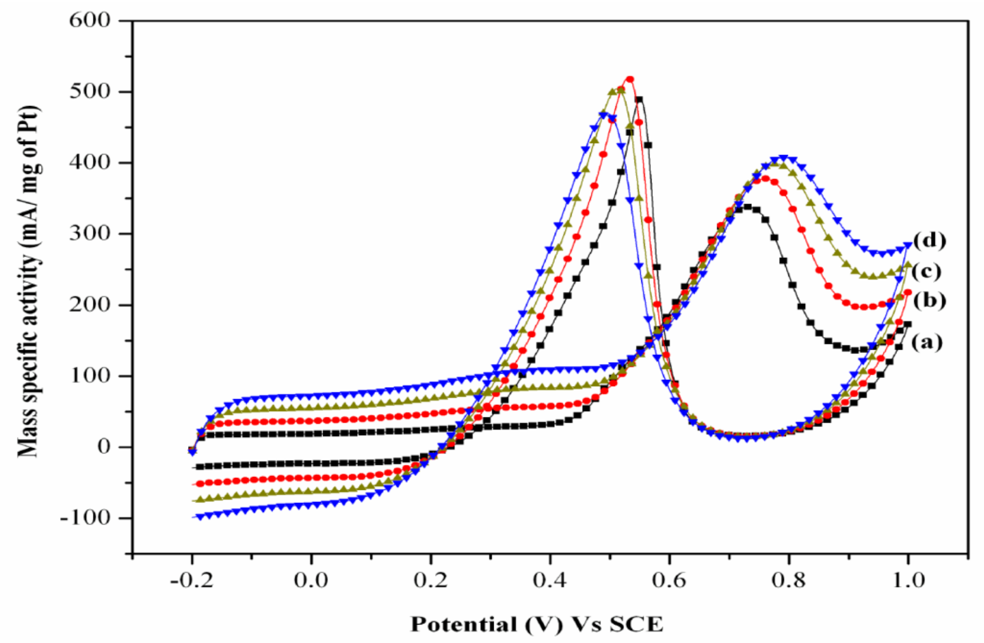

Figure E.6: Cyclic voltammograms of 10 wt.% Pt/CNPI-1 (SBH) at different scan rates ((a) 25 mV/s; (b) 50 mV/s; (c) 75 mV/s; (d) 100 mV/s) in 1 M H_2SO_4 and 1 M CH_3OH at room temperature.

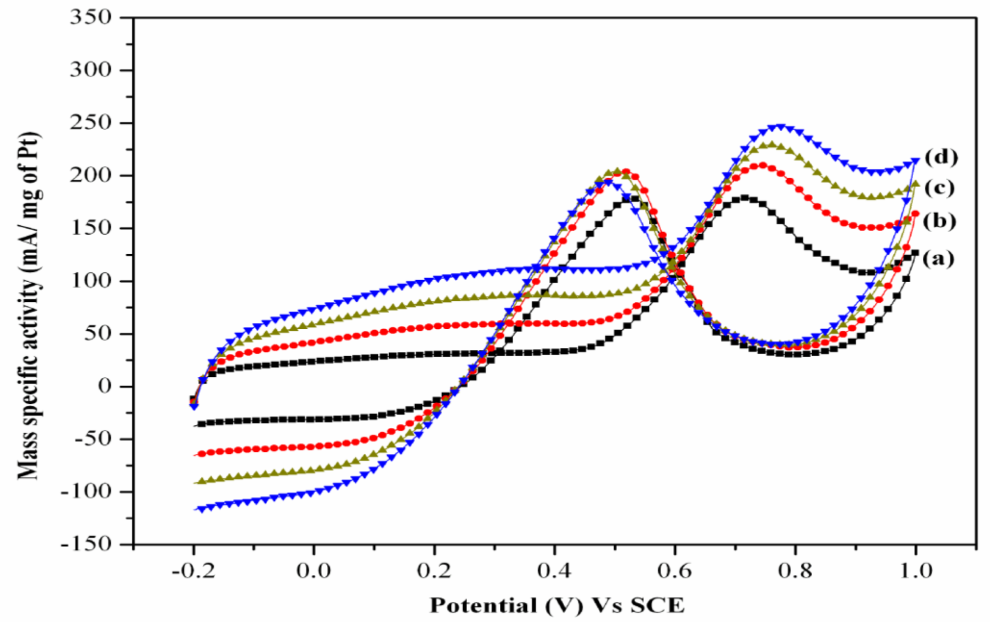

Figure E.7 : Cyclic voltammograms of 10 wt.% Pt/NCNPI-1 (SBH) at different scan rates ((a) 25 mV/s; (b) 50 mV/s; (c) 75 mV/s; (d) 100 mV/s) in 1 M H_2SO_4 and 1 M CH_3OH at room temperature.

E.2 DEPENDENCE OF THE PEAK CURRENTS ON THE SQUARE ROOT OF SCAN RATES

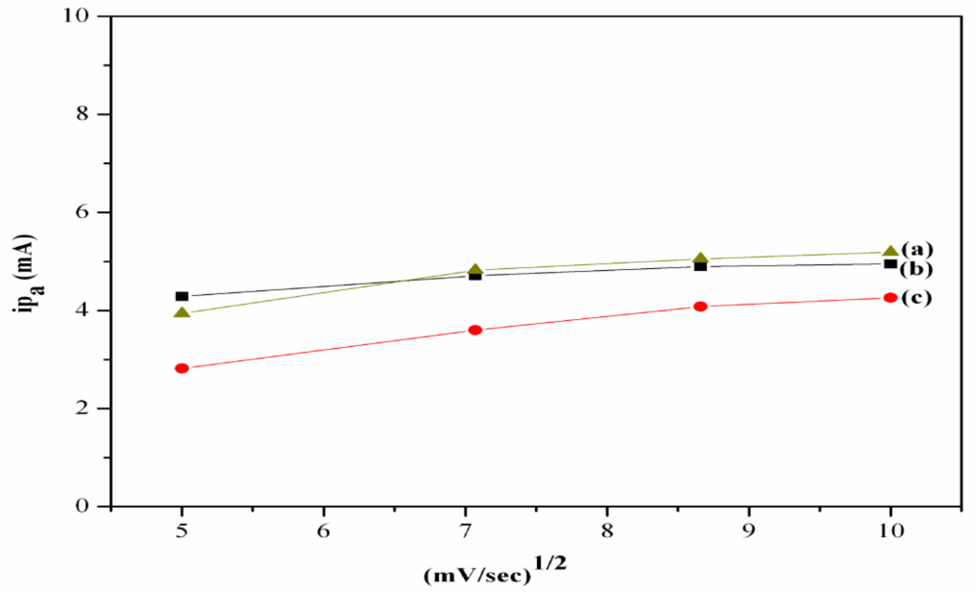

Figure E.8: Dependence of the peak currents on the square root of scan rates of (a) 20 wt.% Pt/AC (SBH); (b) 20 wt.% Pt/CNPI-1 (SBH); (c) 20 wt.% Pt/NCNPI-1 (SBH) in 1 M H_2SO_4 and 1 M CH_3OH at room temperature.

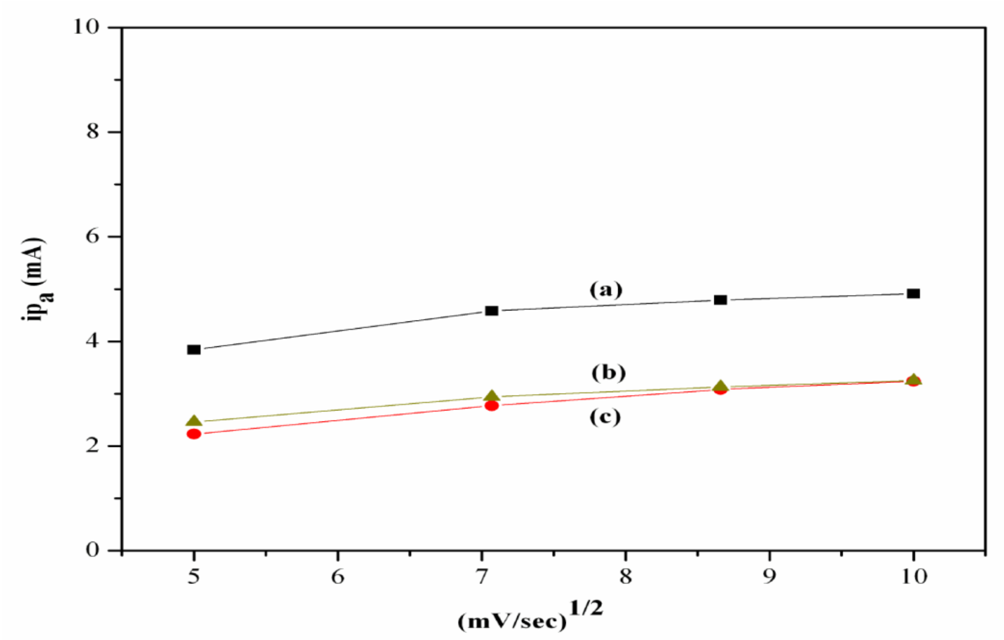

Figure E.9: Dependence of the peak currents on the square root of scan rates of (a) 20 wt.% Pt/CNPI-1 (EG); (b) 20 wt.% Pt/AC (EG); (c) 20 wt.% Pt/NCNPI-1 (EG) in 1 M H_2SO_4 and 1 M CH_3OH at room temperature.

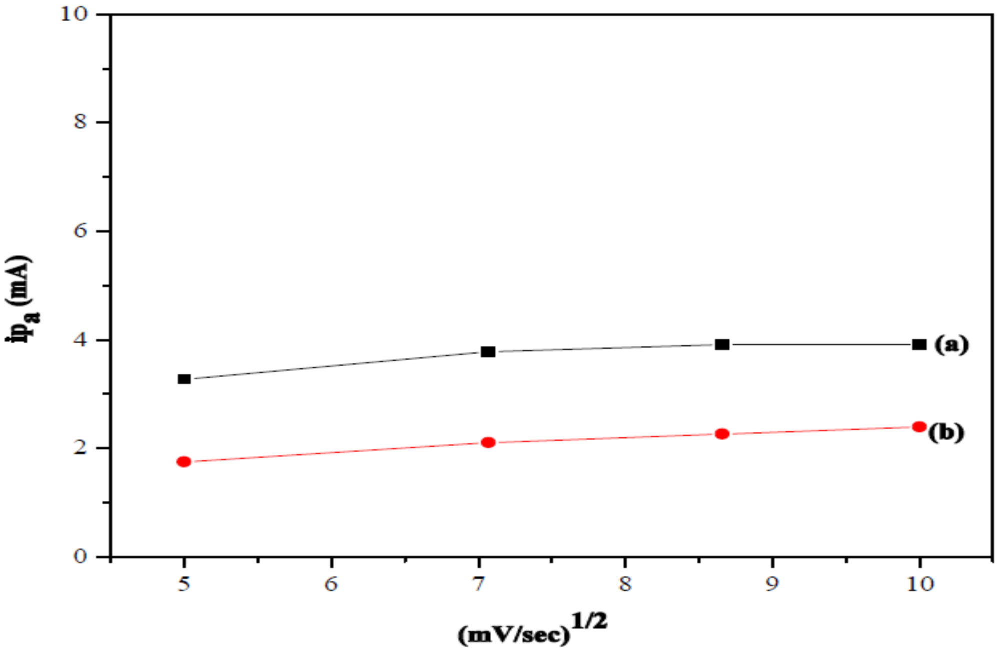

Figure E.10: Dependence of the peak currents on the square root of scan rates of (a) 10 wt.% Pt/CNPI-1 (SBH); (b) 10 wt.% Pt/NCNPI-1 (SBH) in 1 M H_2SO_4 and 1 M CH_3OH at room temperature.

APPENDIX F

CNPI-1 SUPPORTED Pt, Pd and Pd_3Pt ELECTRO-CATALYSTS FOR ORR

F.1 INTRODUCTION

The electrochemical reduction of molecular oxygen is important especially for devices such as metal-air batteries, fuel cells and air cathodes in many industrial electro-catalytic processes. Oxygen reduction reaction (ORR) has been studied over the years because of its fundamental complexity, sensitivity to the electrode surface and sluggish kinetics. The sluggish kinetics of ORR under the conditions employed in electrochemical devices is due to the low partial pressure of oxygen in air, slow flow rate of oxygen (i.e., less residence time for oxygen molecules on active sites) under ambient conditions. The main disadvantage in this electrode reaction is the value of exchange current density (j_0) in the region of 10^{-10} A/cm² in acidic medium and 10^{-8} A/cm² at 298 K in alkaline solution, which is lower than the j_0 value of anodic reaction in the electrochemical devices (Bockries and Reddy, 1970). Hence the oxygen reduction reaction usually contributes considerably to the overpotential and therefore results in a low efficiency in the functioning of electrochemical devices using air as oxidant. Understanding and exploitation of electro-catalysis for this reaction is needed more than any other reactions in electrochemical devices.

F.2 ELECTRO-CATALYSTS FOR OXYGEN REDUCTION REACTION

The essential criteria for better oxygen reduction electro-catalysts are: high electronic conductivity, chemical and structural stability under conditions namely; operating temperature, wide range of oxygen partial pressure and concentration of electrolyte, ability to decompose the intermediate species formed during the reduction process, chemical and thermodynamic compatibility to electrolyte and interconnector materials, tolerant to contaminants and low cost.

Both noble and non-noble metal based electrodes were investigated for oxygen reduction. In the case of noble metal electro-catalysts, platinum and palladium based materials appear to be the best, whereas in the case of non-noble metal electro-catalysts, transition metal chalcogenides and pyrolyzed macrocyclic compounds are most widely studied.

F.2.1 Pt Metal Electro-catalysts

The most promising electro-catalysts for oxygen reduction are based on Pt since they exhibit good activity and chemical stability under operating conditions. The ORR consists of an oxygen diffusion process, adsorption process, charge transfer process, desorption process and back diffusion process. The work function would be one of the key factors of the charge transfer process, because the work function is the minimum energy needed to remove an electron from the material surface. However, the work function of Pt with high catalytic activity for the ORR is higher than the other transition metals (Trasatti, 1971).

In general, oxygen reduction takes place at higher positive potentials. At such high potentials, most of the metals will dissolve and give rise to a similar situation to that prevailing at the cathode i.e., only noble metals and some of their alloys offer possibilities among metallic systems. The most familiar oxygen reduction catalysts are based on noble metals, especially platinum. To date, conventional carbon supported platinum is the efficient electro-catalyst for oxygen reduction. But the cost of the Pt/C electro-catalysts is the main hurdle for the commercialization of electrochemical devices. To reduce the amount of Pt loading at the cathode side, thereby reducing cost, various synthetic approaches are adopted to disperse Pt on suitable support. Among the various support materials, carbon is the most attractive one because of its unique features like good electronic conductivity, chemical stability, surface area, mechanical stability and low cost.

The observations made from the ORR measurements on the carbon supported Pt catalysts are :

(i) Sluggish kinetics of oxygen reduction reaction of Pt. It was observed that the formation of –OH species at + 0.8 V on the Pt surface hinder the oxygen reduction in such a way the kinetics is not facile. The –OH species also causes the less availability of molecular oxygen species and thereby reduce ORR activity.

(ii) Oxygen reduction is a structure sensitive reaction.

(iii) Hydrogen peroxide formation during oxygen reduction on Pt.

ORR Mechanism: In terms of electro-catalysis, oxygen reduction on Pt crystallites occurs by a parallel mechanism with direct four-electron reduction as an essential step. The main steps in the mechanism of oxygen reduction on Pt are shown below (Sidik *et al.,* 2002):

$$O_2 + 2Pt \rightarrow Pt_2O_2 \tag{1}$$

$$Pt_2O_2 + H^+ + e^- \rightarrow Pt2\text{-}O_2H \text{ (rate determining step)} \tag{2}$$

$$Pt_2\text{-}O_2H \rightarrow Pt\text{-}OH + Pt\text{-}O \tag{3}$$

$$Pt\text{-}OH + Pt\text{-}O + H^+ + e^- \rightarrow Pt\text{-}OH + Pt\text{-}OH \tag{4}$$

$$Pt\text{-}OH + Pt\text{-}OH + 2H^+ + 2e^- \rightarrow 2Pt + 2H_2O \tag{5}$$

F.2.2 Pd Electro-catalysts

Palladium has a similar valence shell electronic configuration and lattice constant of Pt. It was also reported that the oxygen reduction takes place in the same manner as that of Pt (Sepa *et al.,* 1981). But the less ORR activity than Pt and poor stability of Pd at high potentials prevents its commercialization. To improve the catalytic ORR activity of Pd, various bimetallic Pd alloys such as Pd-Co, Pd-Fe, Pd-Ni, Pd-Ta and Pd-Cr have been investigated. Pd/C, bimetallic Pd_3Pt/C catalysts were prepared by sol method using SBH and ethylene glycol as a reducing agents (Section 5.2.1).

F.3 CHARACTERIZATION

F.3.1 XRD

Fig. F.1 Shows XRD patterns of 10 wt.% Pd/AC prepared by different methods. 10 wt.% Pd supported on AC had been done for the optimization process. The broad diffraction peak observed on activated carbon supported Pd catalysts at around 25° was corresponding to the carbon. The diffraction peaks at about 40.1°, 46.7°, 68.1° and 82.1° were from the Pd (1 1 1), (2 0 0), (2 2 0) and (3 1 1) planes, respectively (JCPDS file No. 89-4897). The crystallite sizes of Pd, calculated from the Pd (1 1 1) diffraction peak by means of Scherrer equation, for 10 wt.% Pd/AC prepared by wet impregnation and colloidal deposition methods were 22.4 and 5.0 nm, respectively (Table F.1).

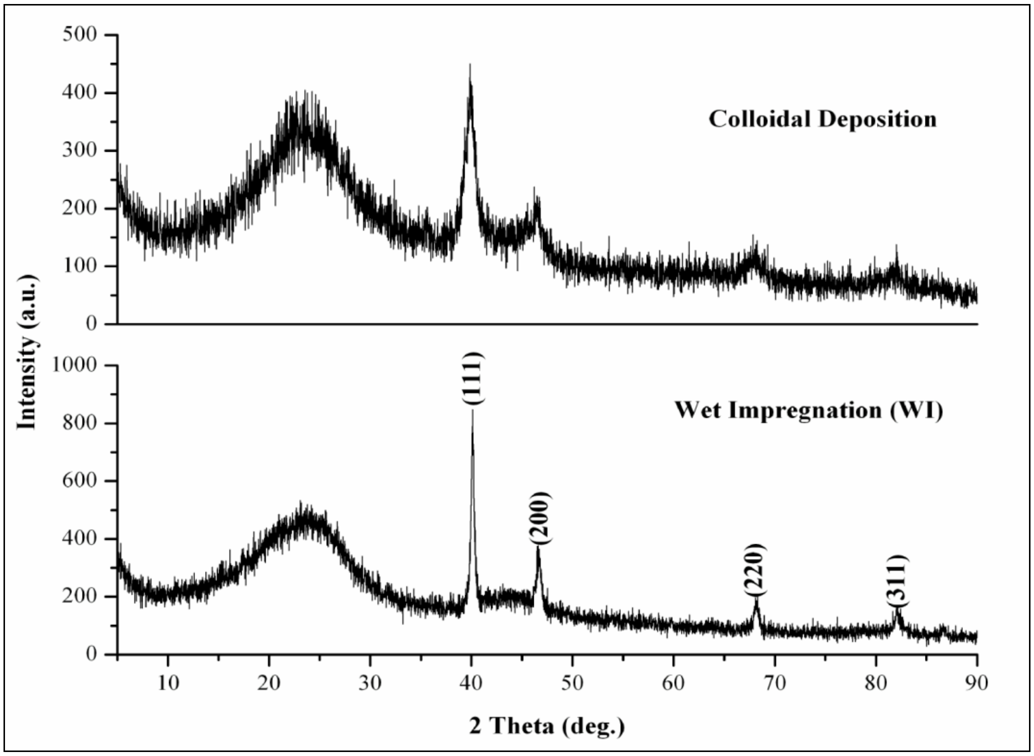

Figure F.1: XRD patterns of 10 wt.% Pd/AC prepared by colloidal deposition and WI method using SBH as a reducing agent.

Fig. F.2 shows XRD patterns of 20 wt.% Pd/C (Carbon: CNPI-1 and AC) prepared by colloidal deposition method using different reducing agents. The broad diffraction peak observed on carbon supported Pd catalysts at around 25° was corresponding to the carbon. The diffraction peaks at about 40.1°, 46.7°, 68.1° and 82.1° were from the Pd (1 1 1), (2 0 0), (2 2 0) and (3 1 1) planes, respectively (JCPDS file No. 87-0647). The crystallite sizes of Pd, calculated from the Pd (1 1 1) diffraction peak by means of Scherrer equation, for 20 wt.% Pd/AC (SBH), 20 wt.% Pd/AC (EG), 20 wt.% Pd/CNPI-1 (SBH) were 20 wt.% Pd/CNPI-1 (EG), prepared by sol method were 17.8, 17.0, 15.8 and 17.6 nm, respectively (Table F.2).

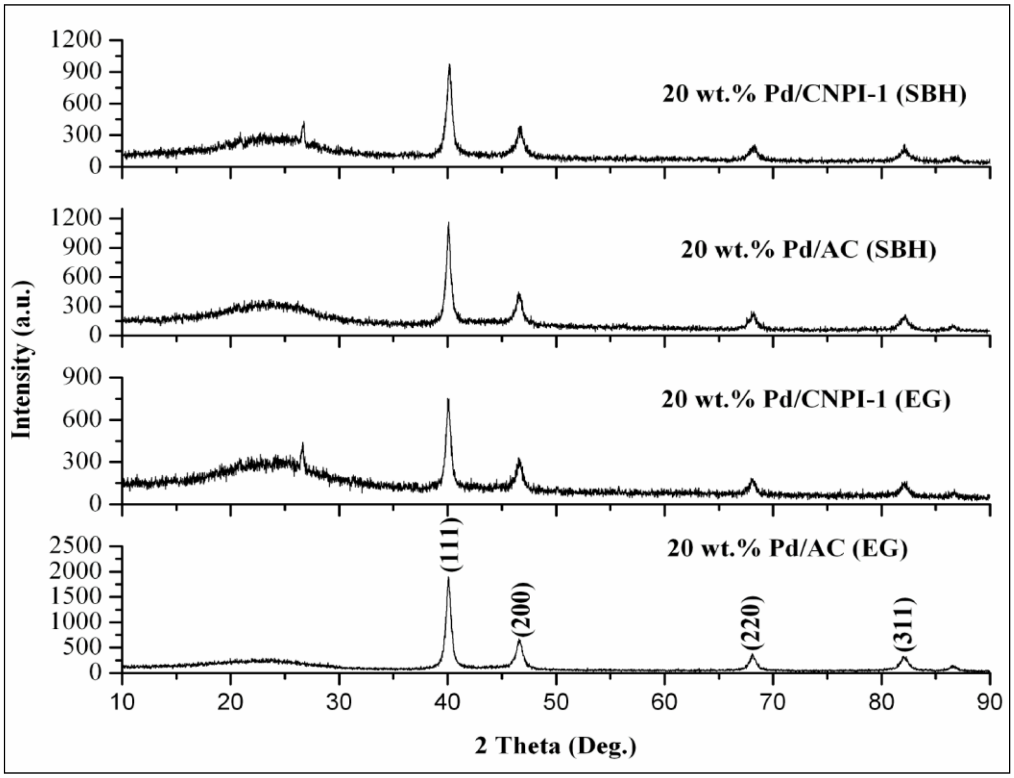

Figure F.2: XRD patterns of 20 wt.% Pd/ C (C: CNPI-1/AC) prepared by colloidal deposition method using different reducing agents (SBH and EG).

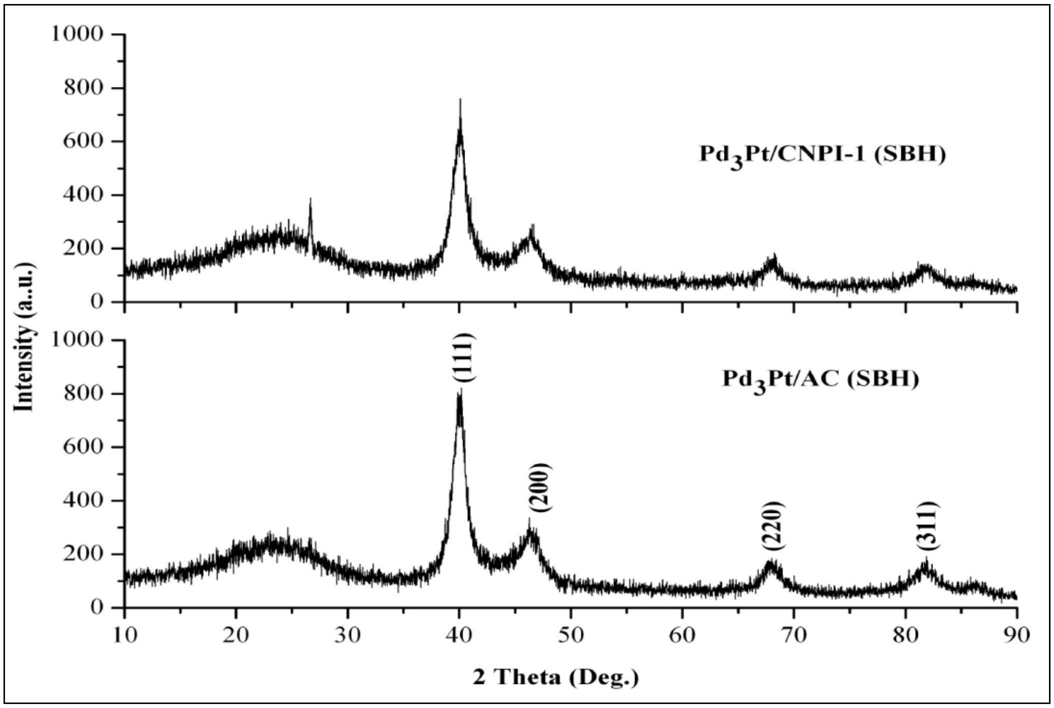

Figure F.3: XRD patterns of Pd_3Pt/C (C: CNPI-1/AC) prepared by colloidal deposition method using SBH as a reducing agent.

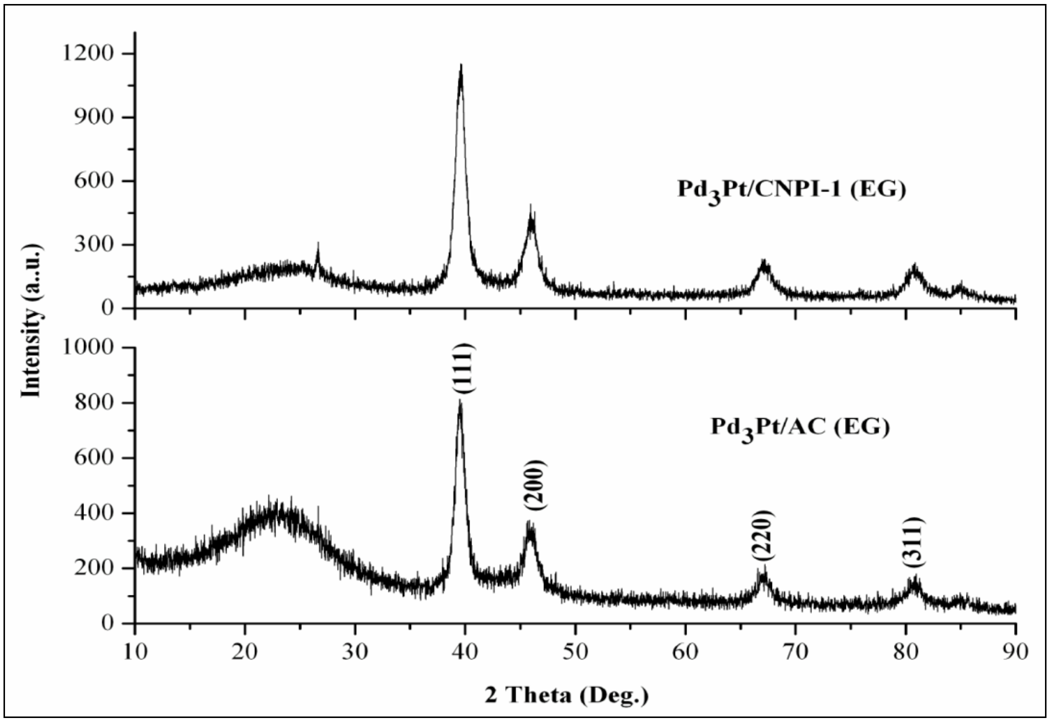

Figure F.4: XRD patterns of Pd_3Pt/C (C: CNPI-1/AC) prepared by colloidal deposition method using EG as a reducing agent.

Fig. F.3 and F.4 show XRD patterns of Pd_3Pt/C (Carbon: CNPI-1 and AC) prepared by colloidal deposition method using SBH and EG as reducing agents respectively. The total metal loading was set at 20 wt.%. The broad diffraction peak observed on Pd_3Pt/C catalysts at around 25° was corresponding to the carbon. The XRD patterns of the bimetallic catalysts displayed a slight negative shift relative to the bulk Pd at around $2\theta = 40.1°$, 46.7°, 68.1° and 82.1° which indicates that a number of Pd atoms were displaced by the larger Pt atoms leading to a lattice expansion due to the formation of Pd-Pt alloys (An *et al.*, 2011). The diffraction peaks at around 39.5°, 45.8°, 67.1° and 80.8° are corresponding to Pd_3Pt (111), (200), (220) and (311) planes respectively. All the diffraction peaks of Pd_3Pt were used to calculate the crystalline lattice parameters and the Pd_3Pt (111) peak was used for the calculation of crystallite size by means of Scherrer equation. The calculated crystallite size values of Pd_3Pt catalysts were tabulated (Table F.3).

Table F.1: Effect of preparation methods on the crystallite size of the AC supported Pd catalysts.

10 wt.% Pd/AC Preparation methods	Reducing Medium	Pd Lattice Constant (nm)	Pd Crystallite Size (nm)
Wet Impregnation	SBH	0.3885	22.4
Colloidal Deposition	SBH	0.3894	5.0

Table F.2: Effect of reducing agents and palladium loading on the crystallite size of the carbon supported Pd catalysts.

Pd Catalysts	Pd Lattice Constant (nm)	Pd Crystallite Size (nm)
20 wt.% Pd/CNPI-1 (SBH)	0.3889	15.8
20 wt.% Pd/AC (SBH)	0.389	17.8
20 wt.% Pd/CNPI-1 (EG)	0.3896	17.6
20 wt.% Pd/AC (EG)	0.3892	17.0

Table F.3: Effect of reducing agents and active metal loading on the crystallite size of the carbon supported Pd_3Pt catalysts.

Pd_3Pt Catalysts	Pd_3Pt Lattice Constant (nm)	Pd_3Pt Crystallite Size (nm)
Pd_3Pt /CNPI-1 (SBH)	0.3898	6.4
Pd_3Pt /AC (SBH)	0.3898	6.9
Pd3Pt /CNPI-1 (EG)	0.3942	8.7
Pd_3Pt /AC (EG)	0.3945	8.8

F.3.2 Electrochemical reduction of Oxygen

Electrochemical oxygen reduction measurements were performed at room temperature in a three electrode; one compartment cell containing 1 M H_2SO_4 as the electrolyte. After fabrication, the electrode was immersed in 1 M H_2SO_4 and purged with N_2 gas for 30 min to deaerate the solution. Then the cyclic voltammogram (scan rate: 50 mV/s) were recorded between -0.2 V to + 1.2 V Vs SCE. For the oxygen reduction experiments, the electrolyte was saturated with pure oxygen and the cyclic voltammogram (scan rate: 50 mV/s) were recorded between -0.2 V to + 1.2 V Vs SCE. Current densities were normalized to the geometric area of the glossy carbon substrate (0.07 cm^2). Electrochemical oxygen reduction results are shown in Fig. F.5.

It was evident that the oxygen reduction on all the catalysts was diffusion controlled when the potential was below + 0.4 V region and was under mixed diffusion-kinetic control in the potential region between + 0.4 V and + 1.2 V Vs SCE (Fig. F.5). For all the catalysts, single oxygen reduction peak was observed in the potential region of + 1.0 to + 0.4 V. The steep increase in peak current at + 0.4 V indicates the facile kinetics of ORR. Oxygen reduction activity was calculated by taking the difference in activity at + 0.4 V Vs SCE in N_2 and O_2 saturated 1 M H_2SO_4 and given in Table F.4. 20 wt.% Pt/CNPI-1 (SBH) showed higher ORR activity compared to other two catalysts. The higher activity of the Pt based monometallic catalyst can be attributed to the uniform and smaller particle size as well as to the higher dispersion of the Pt nanoparticles on the ordered microporous carbon support (Fig. 5.5a and Fig. 5.6a).

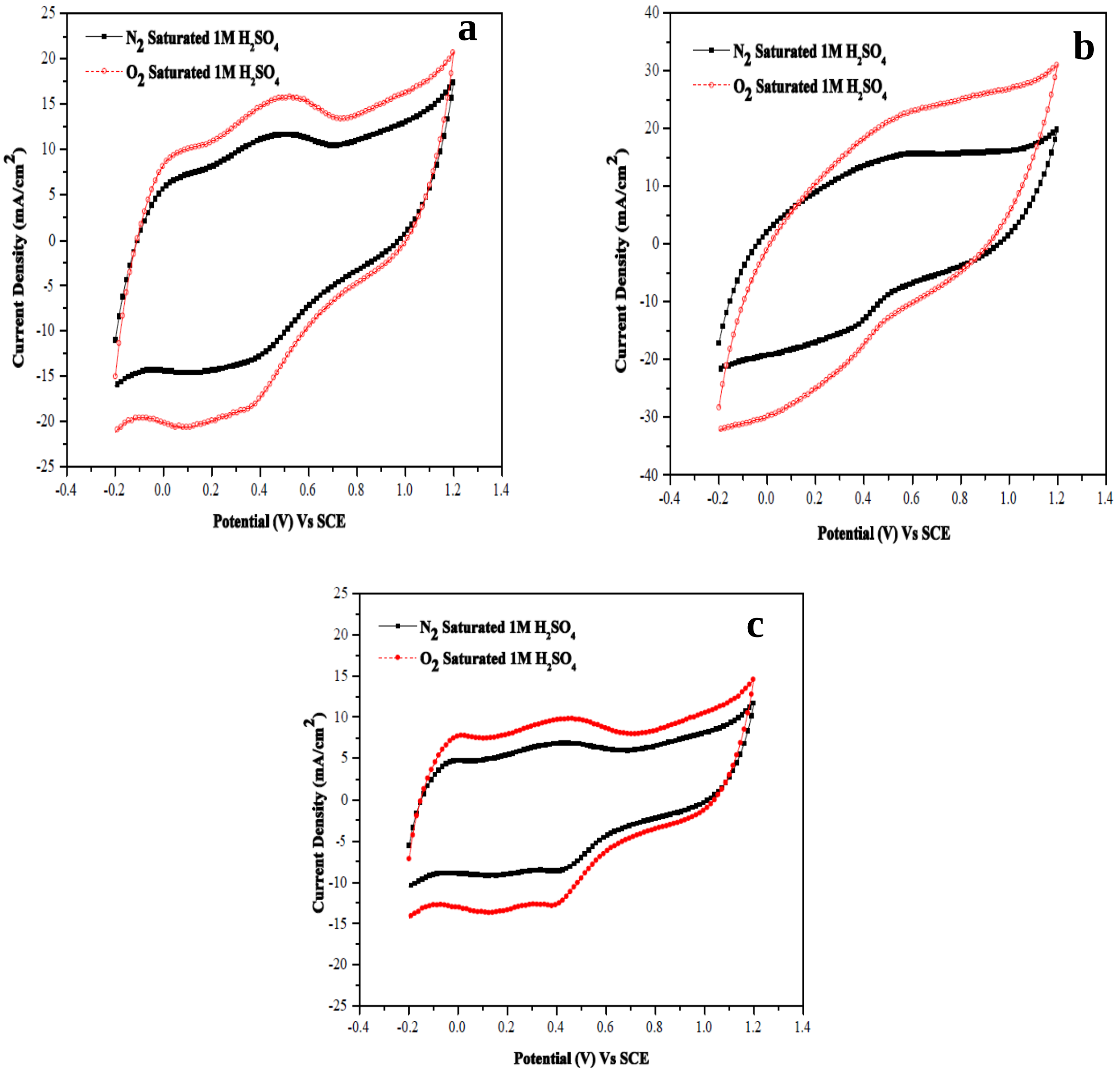

Figure F.5: Cyclic voltammograms of (a) 20 wt.% Pt/ CNPI-1 (SBH); (b) 20 wt.% Pd/ CNPI-1(SBH); (c) Pd_3Pt/ CNPI-1 (SBH) in N_2 and O_2 saturated 1 M H_2SO_4 solution at room temperature (scan rate: 50 mV/s).

Table F.4: ORR activity of the prepared monometallic and bimetallic catalysts.

Catalysts	ORR activity at + 0.4 V Vs SCE (mA/cm^2)
20 wt.% Pt/CNPI-1 (SBH)	4.6
20 wt.% Pd/CNPI-1 (SBH)	4.3
Pd_3Pt/CNPI-1 (SBH)	4.0

REFERENCES

1. **An, S., J. -H. Park, C. -H. Shin, J. Joo, E. Ramasamy, J. Hwang** and **J. Lee** (2011) Well-dispersed Pd_3Pt_1 alloy nanoparticles in large pore sized mesocellular carbon foam for improved methanol-tolerant oxygen reduction reaction. *Carbon*, **49**, 1108-1117.
2. **Bensebaa, F., N. Patrito, Y. L. Page, P. L'Ecuyer** and **D. Wang** (2004) Tunable platinum–ruthenium nanoparticle properties using microwave synthesis. *J. Mater. Chem*., **14**, 3378-3384.
3. **Bockries J. O'M.** and **A. K. N. Reddy** *Modern Electrochemistry: Vol. 2.* Plenum Press, New York, 1970.
4. **Bong, S., Y. -R. Kim, I. Kim, S. Woo, S. Uhm, J. Lee** and **H. Kim** (2010) Graphene supported electro-catalysts for methanol oxidation. *Electrochem. commun*., **12**, 129-131.
5. **Chambers, A., C. Park, R. Terry, K. Baker** and **N. M. Rodriguez** (1998) Hydrogen Storage in Graphite Nanofibers. *J. Phys. Chem. B*, **102**, 4253-4256.
6. **Chen, J., N. Xia, T. Zhou, S. Tan, F. Jiang** and **D. Yuan** (2009). Mesoporous Carbon Spheres: Synthesis, Characterization and Supercapacitance. *Int. J. Electrochem. Sci.*, **4**, 1063-1073.
7. **Chen, S., J. Zhu, X. Wu, Q. Han** and **X. Wang** (2010). Graphene Oxide-MnO_2 Nanocomposites for Supercapacitors. *Nano*, **4**, 2822-2830.
8. **Cullity, B. D.** *Elements of X-Ray Diffraction*. Addison-Wesley Publishing Company, Inc., 1978.
9. **Dicks, A. L.** (2006). The role of carbon in fuel cells. *J. Power Sources*, **156**, 128-141.
10. **Fan, Y. Y., B. Liao, M. Liu, Y. L. Wei, M. Q. Lu** and **H. M. Cheng** (1999) Hydrogen uptake in vapor-grown carbon nanofibers. *Carbon*, **37**, 1649-1652.
11. **Guo, J. W., T. S. Zhao, J. Prabhuram, R. Chen** and **C. W. Wong** (2006) Development of PtRu-CeO_2/C anode electro-catalyst for direct methanol fuel cells. *J. Power Sources*, **156**, 345-354.
12. **Hamnett, A.** (1997). Mechanism and electrocatalysis in the direct methanol fuel cell. *Catal. Today*, **38**, 445-457.

13. **Hirscher, M., M. Becher, M. Haluska, A. Quintel, V. Skakalova, Y. M. Choi, U. D.-Weglikowska, S. Roth, I. Stepanek, P. Bernier, A. Leonhardt** and **J. Fink** (2002) Hydrogen storage in carbon nanostructures. *J. Alloys and Compounds*, **330-332**, 654-658.
14. **Hufner, S.** and **G. K. Wertheim** (1975) Core-line asymmetries in the X-ray photoemission spectra of metals. *Phys. Rev. B*, **11**, 678-683.
15. **Jun, S., S. H. Joo, R. Ryoo, M. Kruk, M. Jaroniec, Z. Liu, T. Ohsuna** and **O. Terasaki** (2000) Synthesis of New, Nanoporous Carbon with Hexagonally Ordered Mesostructure. *J. Am. Chem. Soc*., **122**, 10712-10713.
16. **Kapteijn, F., J. A. Moulijn, S. Matzner** and **H. P. Boehm** (1999) The development of nitrogen functionality in model chars during gasification in CO_2 and O_2. *Carbon*, **37**, 1143-1150.
17. **Kim, K. H.** and **K. B. Kim** (2006) Synthesis of Mesoporous metal oxide/carbon nanotube composite electrode using Hard template method for Supercapacitors. ECS 210th meeting, Abstract0130.
18. **Kim, T. W., R. Ryoo, K. P. Gierszal, M. Jaroniec, L. A. Solovyov, Y. Sakamoto** and **O. Terasaki** (2005). Characterization of mesoporous carbons synthesized with SBA-16 silica template**.** *J. Mater. Chem*., **15**, 1560-1571.
19. **Kyotani, T., T. Nagai, S. Inoue** and **A. Tomita** (1997) Formation of New Type Of Porous Carbon by Carbonization in Zeolite Nanochannels. *Chem. Mater*., **9**, 609–615.
20. **Kyotani, T., N. Sonobe** and **A. Tomita** (1988) Formation of highly orientated graphite from polyacrylonitrile by using a two-dimensional space between montmorillonite lamellae. *Nature*, **331**, 331.
21. **Kyotani, T., L. Tsai** and **A. Tomita** (1995) Formation of Ultrafine Carbon Tubes by using an Anodic Aluminum Oxide Film as a template. *Chem. Mater*., **7**, 1427-1428.
22. **Kyotani, T., L. Tsai** and **A. Tomita** (1996). Preparation of Ultrafine Carbon Tubes in Nanochannels of an Anodic Aluminum Oxide Film. *Chem. Mater*., **8**, 2109-2113.
23. **Kuppan, B., B. Viswanathan** and **P. Selvam** (2011) Platinum Supported Ordered Nanoporous Carbon (NCCR-41) as promising Electro-catalyst for Methanol Fuel Cell Application. *World congress on Engineering and Technology*, Shanghai, October, 28-30.
24. **Lee, J., J. Kim** and **T. Hyeon** (2006) Recent Progress in the Synthesis of Porous Carbon Materials. *Adv. Mater*., **18**, 2073-2094.

25. **Lee, J., S. Yoon, T. Hyeon, S. M. Oh** and **K. B. Kim** (1999) Synthesis of a new mesoporous carbon and its application to electrochemical double-layer capacitors. *Chem. Commun*., 2177- 2178.
26. **Lee, J., S. Yoon, S. M. Oh, C. H. Shin** and **T. Hyeon** (2000) Development of a New Mesoporous Carbon Using an HMS Aluminosilicate Template. *Adv. Mater*., **12**, 359-362.
27. **Lei, Z., L. An, L. Dang, M. Zhao, J. Shi, S. Bai** and **Y. Cao** (2009) Highly dispersed platinum supported on nitrogen – containing ordered mesoporous carbon for methanol electrooxidation. *Microporous and Mesoporous Mater*., **119**, 30-38.
28. **Lei, Z., S. Bai, Y. Xiao, L. Dang, L. An, G. Zhang** and **Q. Xu** (2008) CMK-5 Mesoporous Carbon Synthesized via Chemical Vapor Deposition of Ferrocene as Catalyst support for Methanol Oxidation. *J. Phys. Chem. C*, **112**, 722-731.
29. **Li, X., G. Chen, J. Xie, L. Zhang, D. Xia** and **Z. Wu (2010)** An Electro-catalyst For Methanol Oxidation in DMFC-PtBi (XC-72) with Pt solid-solution structure. *J. Electrochem. Soc*., **157**, B580-B584.
30. **Li, L.** and **Y. Xing** (2007) Pt-Ru Nanoparticles Supported on Carbon Nanotubes as Methanol Fuel Cell Catalysts. *J. Phys. Chem. C*, **111**, 2803-2808.
31. **Liu, Z., X. Y. Ling, J. Y. Lee, X. Su** and **L. M. Gan** (2003) Nanosized Pt and PtRu colloids as precursors for direct methanol fuel cell catalysts. *J. Mater. Chem.*, **13**, 3049-3052.
32. **Liu, B., H. Shioyama, T. Akita** and **Q. Xu** (2008) Metal-Organic Framework as a Template for Porous Carbon Synthesis. *J. Am. Chem. Soc*., **130**, 5390-5391.
33. **Liu, H., C. Song, L. Zhang, J. Zhang, H. Wang,** and **D. P. Wilkinson** (2006). A review of anode catalysis in the direct methanol fuel cell. *J. Power Sources*, **155**, 95-110.
34. **Liu, Z., X. Y. Ling, X. Su** and **J. Y. Lee** (2004) Carbon – supported Pt and PtRu nanoparticles as catalysts for a direct methanol fuel cell. *J. Phys. Chem. B.,* **108**, 8234-8240.
35. **Lu, A. -H.** and **F. Schuth** (2006). Nanocasting: A Versatile Strategy for Creating Nanostructured Porous Materials. *Adv. Mater.*, **18**, 1793-1805.
36. **Lu, A. -H, D. Zhao** and **Y. Wan** *Nanocasting: A Versatile Strategy for Creating Nanostructured Porous Materials*, RSC Publishing (2010).

37. **Luo, J., P. N. Njoki, Y. Lin, D. Mott, L. Wang** and **C. -J. Zhong** (2006). Characterization of Carbon –Supported AuPt Nanoparticles for Electrocatalytic Methanol Oxidation Reaction. *Langmuir*, **22**, 2892-2898.
38. **Ma, Z., T. Kyotani, Z. Liu, O. Terasaki** and **A. Tomita** (2001). Very High Surface Area Microporous Carbon with a Three-Dimensional Nano-Array Structure: Synthesis and Its Molecular Structure. *Chem. Mater*., **13,** 4413-4415.
39. **Ma, Z., T. Kyotani** and **A. Tomita** (2000) Preparation of a high surface area microporous carbon having the structural regularity of Y Zeolite. *Chem. Commun.*, 2365–2366.
40. **Meng, Y., D. Gu, F. Zhang, Y. Shi, L. Cheng, D. Feng, Z. Wu, Z. Chen, Y. Wan, A. Stein** and **D. Zhao** (2006). A Family of Highly Ordered Mesoporous Polymer Resin and Carbon Structures from Organic-Organic Self- Assembly. *Chem. Mater*., **18**, 4447–4464.
41. **Parsons, R.** and **T. VanderNoot** (1988) The oxidation of small organic molecules A survey of recent fuel cell related research. *J. Electroanal. Chem.,* **257**, 9-45.
42. **Pozio, A., M. De Francesco, A. Cemmi, F. Cardellini** and **L. Giorgi** (2002) Comparison of high surface Pt/C catalysts by cyclic voltammetry. *J. Power Sources*, **105**, 13–19.
43. **Ramani, V.** (2006) *The Electrochem. Soc. Interface*, 41-44.
44. **Ralph, T. R., G. A. Hards, J. E. Keating, S. A. Campbell, D. P. Wilkinson, M. Davis, J. St-Pierre and M. C. Johnson** (1997) Low cost electrodes for proton exchange membrane fuel cells. *J. Electrochem. Soc.*, **144**, 3845–3857.
45. **Ryoo, R., S. H. Joo** and **S. Jun** (1999) Synthesis of Highly Ordered Carbon Molecular Sieves via Template-Mediated Structural Transformation. *J. Phys. Chem. B*, **103**, 7743-7746.
46. **Rzepka, M.** and **P. Lamp** (1998). Physisorption of Hydrogen on Microporous Carbon and Carbon Nanotubes. *J. Phys. Chem. B*, **102**, 10894-10898.
47. **Salgado, J. R. C., F. Alcaide, G. Álvarez, L.Calvillo, M. J. Lázaro** and **E. Pastor (2010).** Pt–Ru electro-catalysts supported on ordered mesoporous carbon for direct methanol fuel cell. *J. Power Sources*, **195**, 4022-4029.

48. **Sepa, D. B., M. V. Vojnovic** and **A. Damjanovic** (1981) Reaction intermediates as a controlling factor in the kinetics and mechanism of oxygen reduction at platinum electrodes. *Electrochim. Acta*, **26**, 781-793.
49. **Serp, P.** and **J. L. Figueiredo** *Carbon Materials for Catalysis*. A John Wiley & Sons, Inc., Publication, New York, 2009.
50. **Sidik, R. A.** and **A. B. Anderson (2002)** Density functional theory study of O_2 electroreduction when bounded to a Pt dual site. *J. Electroanal. Chem.*, **528**, 69-76.
51. **Sobkowski, J., K. Franaszczuk** and **K. Dobrowolska** (1992) Effect of anions and pH on the adsorption and oxidation of methanol on a platinum electrode. *J. Electroanal. Chem.*, **330**, 529-540.
52. **Solla-Gullón, J., F. J. Vidal-Iglesias, V. Montiel** and **A. Aldaz** (2004) Electrochemical characterization of platinum–ruthenium nanoparticles prepared by water-in-oil microemulsion. *Electrochim. Acta*, **49**, 5079-5088.
53. **Trasatti, S.** (1971) Work function, electro negativity, and electrochemical behavior of metals: II. Potentials of zero charge and electrochemical work functions. *J. Electroanal. Chem.*, **33**, 351-378.
54. **Viswanathan, B.** and **M. Aulice Scibioh** *Fuel Cell - Principles and Applications*. Universities Press (India) Private Limited, 2006.
55. **Wang, H., Q. Gao** and **J. Hu** (2009) High Hydrogen Storage Capacity of Porous Carbons Prepared by Using Activated Carbon. *J. Am. Chem. Soc.*, **131**, 7016-7022.
56. **Wang, X., B. Xu, X. Liu, J. Guo** and **H. Ichinose** (2006) Synthesis of Fe-included onion-like Fullerenes by chemical vapor deposition. *Diamond and Related Mater.*, **15**, 147-150.
57. **Wang, H. J., H. Yu, F. Peng** and **P. Lv** (2006) Methanol electro-catalytic oxidation on highly dispersed Pt/sulfomated - carbon nanotube catalysts. *Electrochem. Commun.*, **8**, 499-504.
58. **Wu, G.** and **B. Q. Xu** (2007) Carbon nanotube supported Pt electrodes for methanol oxidation: A comparison between multi- and single-walled carbon nanotubes. *J. Power Sources*, **174**, 148-158.

59. **Xia, D., G. Chen, Z. Wang, J. Zhang, S (Rob). Hui, D. Ghosh** and **H. Wang** (2006) Synthesis of Ordered Intermetallic $PtBi_2$ Nanoparticles for Methanol-Tolerant Catalyst in Oxygen Electroreduction. *Chem. Mater.*, **18**, 5746-5749.
60. **Xia, Y., Z. Yang** and **R. Mokaya** (2010) Templated nanoscale porous carbons. *Nanoscale*, **2**, 639-659.
61. **Xiong, L.** and **A. Manthiram** (2005) Catalytic activity of Pt–Ru alloys synthesized by a microemulsion method in direct methanol fuel cells. *Solid State Ionics*, **176**, 385-392.
62. **Xu, B., X. Yang, X. Wang, J. Guo** and **X. Liu** (2006) A novel catalyst support for DMFC: Onion-like fullerenes. *J. Power Sources*, **162**, 160-164.
63. **Xue, X., T. Lu, C. Liu** and **W. Xing** (2005) Simple and controllable synthesis of highly dispersed Pt-Ru/C catalysts by a two-step spray pyrolysis process. *Chem. Commun.*, 1601-1603.
64. **Yuan, D. S., J. Zeng, J. Chen** and **Y. Liu** (2009) Highly Ordered Mesoporous Carbon Synthesized via in situ Template for Supercapacitors. *Int. J. Electrochem. Sci.*, **4**, 562-570.
65. **Zeng, J., F. Su, J. Y. Lee, X. S. Zhao, J. Chen** and **X. Jiang** (2007) Method for preparing highly dispersed Pt catalysts on mesoporous carbon support. *J. Mater. Sci.*, **42**, 7191-7197.